IJOER
RESEARCH JOURNAL

International Journal

of

Engineering Research & Science
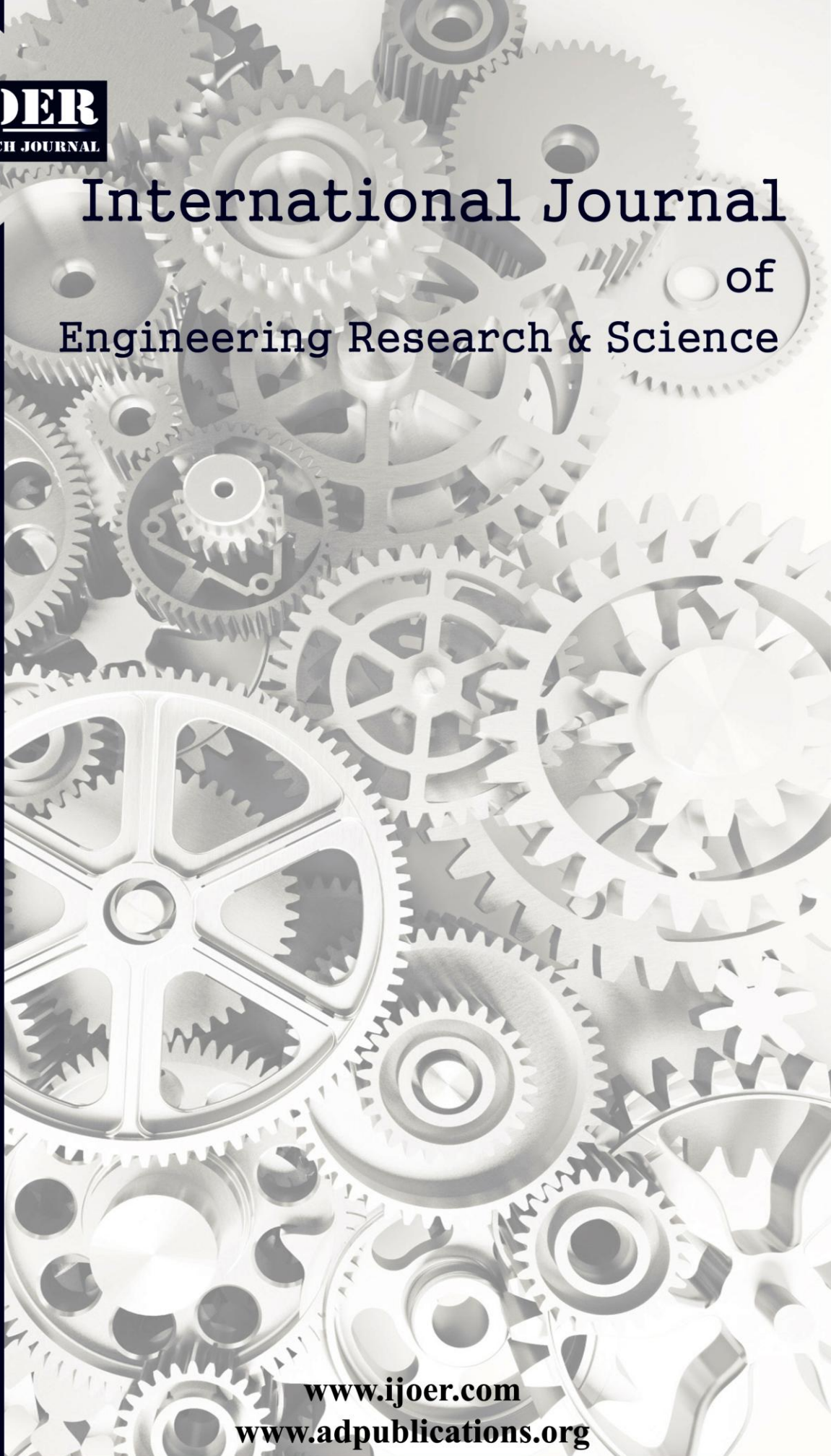
www.ijoer.com
www.adpublications.org

Preface

We would like to present, with great pleasure, the inaugural volume-3, Issue-11, November 2017, of a scholarly journal, *International Journal of Engineering Research & Science*. This journal is part of the AD Publications series *in the field of Engineering, Mathematics, Physics, Chemistry and science Research Development*, and is devoted to the gamut of Engineering and Science issues, from theoretical aspects to application-dependent studies and the validation of emerging technologies.

This journal was envisioned and founded to represent the growing needs of Engineering and Science as an emerging and increasingly vital field, now widely recognized as an integral part of scientific and technical investigations. Its mission is to become a voice of the Engineering and Science community, addressing researchers and practitioners in below areas

Chemical Engineering	
Biomolecular Engineering	Materials Engineering
Molecular Engineering	Process Engineering
Corrosion Engineering	
Civil Engineering	
Environmental Engineering	Geotechnical Engineering
Structural Engineering	Mining Engineering
Transport Engineering	Water resources Engineering
Electrical Engineering	
Power System Engineering	Optical Engineering
Mechanical Engineering	
Acoustical Engineering	Manufacturing Engineering
Optomechanical Engineering	Thermal Engineering
Power plant Engineering	Energy Engineering
Sports Engineering	Vehicle Engineering
Software Engineering	
Computer-aided Engineering	Cryptographic Engineering
Teletraffic Engineering	Web Engineering
System Engineering	
Mathematics	
Arithmetic	Algebra
Number theory	Field theory and polynomials
Analysis	Combinatorics
Geometry and topology	Topology
Probability and Statistics	Computational Science
Physical Science	Operational Research
Physics	
Nuclear and particle physics	Atomic, molecular, and optical physics
Condensed matter physics	Astrophysics
Applied Physics	Modern physics
Philosophy	Core theories

Chemistry	
Analytical chemistry	Biochemistry
Inorganic chemistry	Materials chemistry
Neurochemistry	Nuclear chemistry
Organic chemistry	Physical chemistry
Other Engineering Areas	
Aerospace Engineering	Agricultural Engineering
Applied Engineering	Biomedical Engineering
Biological Engineering	Building services Engineering
Energy Engineering	Railway Engineering
Industrial Engineering	Mechatronics Engineering
Management Engineering	Military Engineering
Petroleum Engineering	Nuclear Engineering
Textile Engineering	Nano Engineering
Algorithm and Computational Complexity	Artificial Intelligence
Electronics & Communication Engineering	Image Processing
Information Retrieval	Low Power VLSI Design
Neural Networks	Plastic Engineering

Each article in this issue provides an example of a concrete industrial application or a case study of the presented methodology to amplify the impact of the contribution. We are very thankful to everybody within that community who supported the idea of creating a new Research with IJOER. We are certain that this issue will be followed by many others, reporting new developments in the Engineering and Science field. This issue would not have been possible without the great support of the Reviewer, Editorial Board members and also with our Advisory Board Members, and we would like to express our sincere thanks to all of them. We would also like to express our gratitude to the editorial staff of AD Publications, who supported us at every stage of the project. It is our hope that this fine collection of articles will be a valuable resource for *IJOER* readers and will stimulate further research into the vibrant area of Engineering and Science Research.

Mukesh Arora

(Chief Editor)

Board Members

Dr. S.R.Boselin Prabhu

Ph.D, Wireless Sensor Networks, M.E. Network Engineering, Excellent Professional Achievement Award Winner from Society of Professional Engineers Biography Included in Marquis Who's Who in the World (Academic Year 2015 and 2016). Currently Serving as Assistant Professor in the department of ECE in SVS College of Engineering, Coimbatore.

Dr. Maheshwar Shrestha

Postdoctoral Research Fellow in DEPT. OF ELE ENGG & COMP SCI, SDSU, Brookings, SD Ph.D, M.Sc. in Electrical Engineering from SOUTH DAKOTA STATE UNIVERSITY, Brookings, SD.

Zairi Ismael Rizman

Senior Lecturer, Faculty of Electrical Engineering, Universiti Teknologi MARA (UiTM) (Terengganu) Malaysia Master (Science) in Microelectronics (2005), Universiti Kebangsaan Malaysia (UKM), Malaysia. Bachelor (Hons.) and Diploma in Electrical Engineering (Communication) (2002), UiTM Shah Alam, Malaysia

Dr. D. Amaranatha Reddy

Ph.D.(Postdocteral Fellow,Pusan National University, South Korea), M.Sc., B.Sc. : Physics.

Dr. Dibya Prakash Rai

Post Doctoral Fellow (PDF), M.Sc.,B.Sc., Working as Assistant Professor in Department of Physics in Pachhuncga University College, Mizoram, India.

Dr. Pankaj Kumar Pal

Ph.D R/S, ECE Deptt., IIT-Roorkee.

Dr. P. Thangam

BE(Computer Hardware & Software), ME(CSE), PhD in Information & Communication Engineering, currently serving as Associate Professor in the Department of Computer Science and Engineering of Coimbatore Institute of Engineering and Technology.

Dr. Pradeep K. Sharma

PhD., M.Phil, M.Sc, B.Sc, in Physics, MBA in System Management, Presently working as Provost and Associate Professor & Head of Department for Physics in University of Engineering & Management, Jaipur.

Dr. R. Devi Priya

Ph.D (CSE),Anna University Chennai in 2013, M.E, B.E (CSE) from Kongu Engineering College, currently working in the Department of Computer Science and Engineering in Kongu Engineering College, Tamil Nadu, India.

Dr. Sandeep

Post-doctoral fellow, Principal Investigator, Young Scientist Scheme Project (DST-SERB), Department of Physics, Mizoram University, Aizawl Mizoram, India- 796001.

Mr. Abilash

MTech in VLSI, BTech in Electronics & Telecommunication engineering through A.M.I.E.T.E from Central Electronics Engineering Research Institute (C.E.E.R.I) Pilani, Industrial Electronics from ATI-EPI Hyderabad, IEEE course in Mechatronics, CSHAM from Birla Institute Of Professional Studies.

Mr. Varun Shukla

M.Tech in ECE from RGPV (Awarded with silver Medal By President of India), Assistant Professor, Dept. of ECE, PSIT, Kanpur.

Mr. Shrikant Harle

Presently working as a Assistant Professor in Civil Engineering field of Prof. Ram Meghe College of Engineering and Management, Amravati. He was Senior Design Engineer (Larsen & Toubro Limited, India).

Table of Contents

MATLAB-Based Stochastic Modeling Distribution Analysis of Commercial Fishery Length-Frequency Samples Taken From the Black Sea (Bulgaria)

Ivelina Zlateva[1], Mariela Alexandrova[2], Nikola Nikolov[3], Violin Raykov[4]

[1,2,3]Department of Automation, Technical University of Varna, Bulgaria
[4]Institute of Oceanology - Varna, Bulgaria
Corresponding Authors Email: m_alexandrova@tu-varna.bg

Abstract— *Fish stock assessment procedure is initially based on the assumption that the frequencies in length/weight-frequency samples used for analysis of the stock status follow approximately the normal distribution. Many of the statistical procedures are based on specific distributional assumptions. The assumption of normality is very common in most classical statistical tests. In case that analysis of data implies techniques that make normality or some other distributional assumptions it is essential that this assumption is confirmed. If distributional assumption is proved, more powerful parametric techniques can be applied and if it is not justified an application of non-parametric or robust techniques may be required.*

The present article aims to present MATLAB-based algorithm for commercial fisheries length-frequency samples distribution analysis of samples of Sprat and Anchovy caught in the Bulgarian waters in the Black sea. The statistical analysis uses engineering approaches in statistical data processing and the method used for analysis of sample frequencies distribution is chi-square normality or goodness of fit test. For the provision of this analysis, specific program is developed in MATLAB programming environment to support and confirm the assumption that length-frequency samples follow the normal distribution.

Keywords— *MATLAB, fisheries, normal distribution, length-frequency samples, stock assessment, chi-square normality test.*

I. INTRODUCTION

Fish stock assessment procedure is initially based on the assumption that the frequencies in length-frequency samples used for analysis follow approximately the normal distribution [9]. The normal (Gaussian) distribution is a very common continuous probability distribution and it is important in statistics because it is often used in natural and social sciences to represent real-valued random variables whose distributions are not known [1,4,5]. The normal distribution is also useful due to its relation to the central limit theorem. Under certain conditions, in its most general form, the normal distribution determines that averages (mean values or expectation) of samples of observations of random variables, independently drawn from a population with unknown distribution, converge in distribution approximate to normal. The sample becomes normally distributed when the number of observations is sufficiently large. Any real values expected to indicate the sum of many independent processes (such as measurement errors) often have distributions that are relatively normal. Moreover, many results and methods (such as propagation of uncertainty and least squares parameter fitting) can be calculated analytically in explicit form when the relevant variables are normally distributed [5,7]. There are in use many non-parametric and robust statistical techniques, which are not based on strong distributional assumptions, however those based on specific distributional assumptions are considered in general most powerful and respectively preferred [6].

The present article deals with distribution analysis of commercial fisheries samples (length-frequency samples) of species taken from commercial catch caught in the Bulgarian part of the Black sea – i.e. sprat as a targeted catch and anchovy as by-catch and is aiming to confirm and justify the assumption for normality of length-frequencies samples distribution. The samples are analyzed by using engineering approaches in stochastic modeling and [2,3,6] the calculations are held in MATLAB programming environment by using specific program developed for the provision of this analysis.

II. METHODS

An experimental approach was adopted for collection of statistical data (total body length measurements of sprat and anchovy) to support the stochastic modeling process and distribution analysis. The samples are taken from commercial catches (stationary pound nets – with mesh size 7.5mm). The fish was caught on 1st of May 2017, near Varna, Bulgaria -

"Trakata" area. The catch composition was presented by two species– Sprat (*Sprattus Sprattus*) as a targeted catch and anchovy (*Engraulis Encrasicolus*) as a by-catch. The samples processed for further analysis are: $n=1000$ individuals of sprat and $n=230$ individuals of anchovy. The body length measurements of the samples have been recorded and processed to form the input massive for calculations done by a specified script developed in MATLAB programming environment. The null hypothesis is formed under the above-described conditions, stating that sample data follows the normal distribution. Respectively an alternative hypothesis is that the sample data do not follow the normal distribution.

The probability density function of the normal distribution is

$$f(x) = \frac{1}{s\sqrt{2\pi}} exp\left[-\frac{(x-M)^2}{2s^2}\right] \tag{1}$$

where: the expectation *M* (also median and mode) and the standard deviation sare distribution parameters, which characterize the center of the distribution and its scale and s^2 is the variance of *M:*

$$M = \int_{-\infty}^{\infty} xf(x)dx \tag{2}$$

$$s^2 = \int_{-\infty}^{\infty} (x - M)^2 f(x) \tag{3}$$

here: $-\infty < x > \infty, -\infty < M > \infty, s > 0$.

Significant and unbiased estimates of the expectation and variance when the sample is broken to *k*-intervals
(where: $k \approx 1 + 3.22\log_{10}(n)$ and *n* is the number of observations or observed frequencies) are:

$$\bar{x} = \frac{1}{n}\sum_{i=1}^{k} x_i^* n_i = \sum_{i=1}^{k} x_i^* P_i, \ P_i = \frac{n_i}{n} \tag{4}$$

$$s^2 = \frac{1}{n-1}\sum_{i=1}^{k} n_i (x_i^* - \bar{x})^2 = \frac{n}{n-1}\sum_{i=1}^{k} (x_i^* - \bar{x})^2 P_i \tag{5}$$

where: x_i^* is the mid-point of the, *i-th*" interval, and n_i are the observed frequencies in a given interval.

Important parameters in distribution analysis are the skewness (a parameter, characterizing the asymmetry) of the distribution and the excess. They both are used to identify the deviation of a certain distribution from the normal distribution. Their estimates for a finite number of values of a random variable are:

$$m_3 = \sum_{i=1}^{k} (x_i^* - \bar{x})^3 P_i \tag{6}$$

$$m_4 = \sum_{i=1}^{k} (x_i^* - \bar{x})^4 P_i \tag{7}$$

For symmetric distribution the skewness (asymmetry) is zero. Depending on the sign of the asymmetry it could be negative (the distribution is left-skewed and it has a long tail in the negative direction of the number line) and positive (right-skewed). In both cases the mean is also shifted, following the asymmetry sign.

The asymmetry relation to variance is an important indicator, which allows comparative analysis of two distributions, having a different scale. The estimate of this indicator is obtained with:

$$\sqrt{b_1} = \frac{m_3}{m_2^{3/2}} \tag{8}$$

The excess kurtos is m_4 is a measure of whether the data is heavy-tailed or light-tailed in relation to the normal distribution. That is, data set with high kurtosis tend to have heavy tails, or outliers. Data set with low kurtosis tend to have light tails, or lack of outliers. A uniform distribution would be an extreme case.

Its estimate is obtained with:

$$b_2 = \frac{m_4}{m_2^2} \tag{9}$$

For normal distribution the real precise value of proportion (9) is 3.

Normality tests are used to determine if a data set is well-modeled by a normal distribution and to compute how likely it is for a random variable underlying the data set to be normally distributed. More precisely, the tests are a form of model selection, and can be interpreted in several ways, depending on the aim of analysis and interpretations of probability and certain distribution parameters.

The experimental data is tested for normality using the chi-square normality test:

$$\chi^2 = \sum_{i=1}^{k} \frac{(n_i - n_{i\_t})^2}{n_{i\_t}}$$

(10)

where: n_{i_t} are the theoretical frequencies, n_i are the observed frequencies [3].

The chi-square normality test (or chi-square goodness of fit test) is used to test if a sample of data came from a population with a specific distribution [6,8]. The chi-square test is defined for the hypothesis H_0 – the data (the frequency distribution of certain eventsor variables) observed in a sample is consistent with a specific theoretical distribution and H_a – the data do not follow the specified distribution. For the provision of this analysis the events considered as hypothesis must be independent and have a total probability which equals 1. The null hypothesis is retained if the calculated value for χ^2 is less than a certain critical value $\chi^2{}_T$ ($v; p$) under significance level α, (where *v are the degrees of freedom and p is the probability*).

2.1   MATLAB based calculation procedure

The MATLAB script is developed in accordance with the following calculation procedure

Step	Matlab function	Description
1	*L=load('L.mat')*	Form the input data massive
2	*n = length(L)*	Define the size of input data massive loaded
3	*x₁=min(L)*	Calculate the min value
4	*x₂= max(L)*	Calculate the max value
5	*K= 1 +3,22*log₁₀(n)*	Calculate the interval numbers K. Round K to the nearest integer valuek
6	*delta=(x₂-x₁)/k*	Define the intervals length.
7	*hist(L, k);grid*	Build the histogram
8	*ni=hist(L,k)*	Calculate intervals frequencies, (vector row)
9	*Pe=nᵢ/n*	Calculate the frequencies by intervals, (vector row)
10	*x(1)=x₁+delta/2;* *for i=2:k* *x(i)=x(i-1)+delta;end*	Calculate interval midpoints, (vector row)
11	*M=x*Pe'*	Calculate the expectation value M
12	*s2=((x-M).^2)*Pe';* *S2=S2*n/(n-1)*	Calculate the variance
13	*s=sqrt(S2)*	Calculate the standard deviation
14	*a=1/(sqrt(2*pᵢ)*S);* *b=((x-M).^2)/(2*S2);* *f=a*delta*exp(-b)*	Calculate the theoretical distribution f by intervals
15	*ff=sum(f)*	Calculate the sum f
16	*ni_t=f*n*	Calculate the theoretical frequencies by intervals
17	n_{ic} and n_{i_tc}	Combine intervals (bins) with frequency count less than 5
18	*cap=((nᵢc-nᵢ_tc).^2)./nᵢ_t*	Calculated the weighed residuals
19	*χ²=sum(cap)*	Calculate χ^2 value
20	*Pef=[Pe'f']; plot(x,[Pef]), grid*	Build the histograms of the empirical and theoretical distributions
21	$f(x) = \dfrac{1}{s\sqrt{2\pi}} exp\left[-\dfrac{(x-M)^2}{2s^2}\right]$	Build the Normal distribution with the stochastic models delivered

The chi-square test is found sensitive to the selection of bins number (intervals) and for the approximation to be valid the expected (calculated, theoretical) frequency should be at least 5. It is not well applied to small samples and if some of the counts in sample frequencies are less than 5 it is recommended that they are combined.

2.2   MATLAB program script

```
clc
clear
load('spratLW.mat')
n=length(L);
```

```
x1=min(L)
x2=max(L)
K=1+(3.2*log10(n))
k=round(K)
delta=(x2-x1)/k
disp('Give precise value for deltal deltal=:')
deltal = input('deltal=')
hist(L,k);grid
Ni=hist(L,k)
ni=Ni;
Pe=ni/n
Pes=sum(Pe)
x(1)=x1+(deltal/2)
for i=2:k
    x(i)=x(i-1)+deltal;
end
x(i)
M=x*Pe'
S2=((x-M).^2)*Pe'
s2=S2*n/(n-1)
S=sqrt(S2)
a=1/(sqrt(2*pi)*S)
b=((x-M).^2)/(2*S2)
ft=a*(deltal*exp(-b))
ff=sum(ft)
ni_t=ft*n
disp('Combine intervals with values of ni_t less than 5')
disp('number of intervals with frequency < 5 r=:')
r = input('r=')
for i=1:k-r
ni_tc(i)=input('ni_tc=:')
end
disp('Combine intervals with values of ni less than 5')
ni=Ni
for i=1:k-r
nic(i)=input('nic=:')
end
cap=((nic-ni_tc).^2)./ni_tc;
chi2=sum(cap)
disp('Compare chi2 value with critical value of Chi2 distribution table:')
Chi2cr=input('enter Chi2cr Table value Chi2cr=:')
if chi2<Chi2cr
disp('sample frequencies follow the normal distribution')
else
disp('sample frequencies do not follow the normal distribution')
end
```

III. RESULTS

3.1 Chi-square test results length-frequency sample distribution analysis of sprat

The interim and final test results are presented in Table 1.

TABLE 1
NORMALITY TEST RESULTS FOR LENGTH-FREQUENCY SAMPLE OF SPRAT

| Interval numbers k=11, observations interval [x_{min}:x_{max}]=[6.30;11.00] (cm), dl=0.61 | | | | | | | |
| Expectation M=9.2676; Variance S^2=0.5945; Standard deviation S=0.7711; | | | | | | | |
Intervals (cm)	Intervals midpoint x	Observed frequencies n_i	Theoretical Frequencies n_{it}	Corrected Observed Frequencies n_{ic}	Corrected Theoretical Frequencies n_{i_ic}	Empirical Probability $P_e=n_i/N$	Theoretical Probability f
6.30-6.91	6.6050	2	0.8123			0.0020	0.0008
6.92-7.53	7.2150	13	9.1255	15	9.9378	0.0130	0.0091
7.54-8.15	7.8250	52	54.8276	52	54.8276	0.0520	0.0548
8.16-8.77	8.4350	160	176.1687	160	176.1687	0.1600	0.1762
8.78-9.39	9.0450	316	302.7235	316	302.7235	0.3160	0.3027
9.40-10.01	9.6550	273	278.1964	273	278.1964	0.2730	0.2782
10.02-10.63	10.2650	159	136.7240	159	136.7240	0.1590	0.1367
10.64-11.25	10.8750	19	35.9357	19	35.9357	0.0190	0.0359
11.26-11.87	11.4850	3	5.0512			0.0030	0.0051
11.88-12.49	12.0950	2	0.3797	6	5.4462	0.0020	0.0004
12.50-13.11	12.7050	1	0.0153			0.0010	0.0000
χ^2=16.55 <χ^2_T (5; 0.005)=16.75➔ the null hypothesis is retained and the sample data follows the normal distribution							

Expected (theoretical) frequencies in count less than 5 are combined to ensure validity of chi-square test results. They are marked in different color, presented in bold and denoted in Table1.

The histogram of the empirical probabilities P_e, theoretical probabilities f_t by bins (intervals) and the shape of the theoretical probability distribution are presented in Fig. 1.
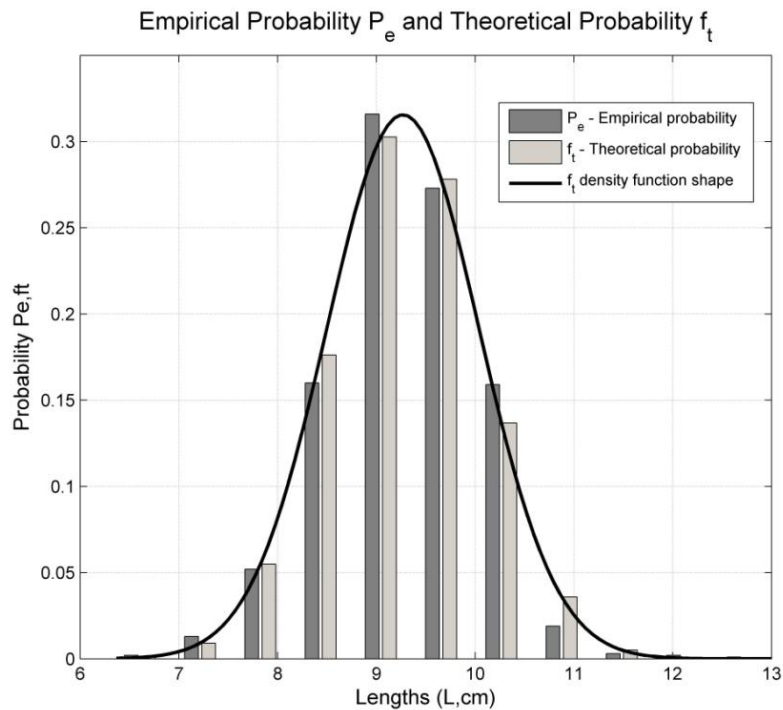
FIGURE 1. HISTOGRAM OF THE EMPIRICAL PROBABILITY P_e, THEORETICAL PROBABILITY f_t AND THE SHAPE OF THE THEORETICAL PROBABILITY DISTRIBUTION OF SPRAT LENGTH-FREQUENCY SAMPLE

3.2   Chi-square test result length-frequency sample distribution analysis of anchovy

The interim and final test results are presented in Table 2.

TABLE 2
NORMALITY TEST RESULTS FOR LENGTH-FREQUENCY SAMPLE OF ANCHOVY

Interval numbers k=9, observations interval [x_{min}:x_{max}]=[9.00;14.50] (cm), dl=0.61							
Expectation M=12.0686; Variance S^2=1.0343; Standard deviation S=1.0170;							
Intervals (cm)	*Intervals midpoint x*	*Observed frequencies n_i*	*Theoretical Frequencies n_{it}*	*Corrected Observed Frequencies n_{ic}*	*Corrected Theoretical Frequencies $n_{\_itc}$*	*Empirical Probability Pe=n_i/N*	*Theoretical Probability f*
9.00-9.61	9.3050	*1*	*1.3714*			0.0043	0.0060
9.62-10.23	9.9150	*10*	*5.8468*	11	7.2182	0.0435	0.0254
10.24-10.85	10.5250	17	17.3947	17	17.3947	0.0739	0.0756
10.86-11.47	11.1350	34	36.1134	34	36.1134	0.1478	0.1570
11.48-12.09	11.7450	44	52.3206	44	52.3206	0.1913	0.2275
12.10-12.71	12.3550	56	52.8966	56	52.8966	0.2435	0.2300
12.72-13.33	12.9650	40	37.3194	40	37.3194	0.1739	0.1623
13.34-13.95	13.5750	24	18.3735	24	18.3735	0.1043	0.0799
13.96-14.57	14.1850	4	6.3125	4	6.3125	0.0174	0.0274
χ^2=6.63<χ^2_T (5; 0.1)=9.236➔ the null hypothesis is retained and the sample data follows the normal distribution							

Expected (theoretical) frequencies in count less than 5 are combined to ensure validity of chi-square test results. They are marked in different color, presented in bold and denoted in Table 2.

The histogram of the empirical probabilities P_e, theoretical probabilities f_t by bins (intervals) and the shape of the theoretical probability distribution are presented in Fig. 2.
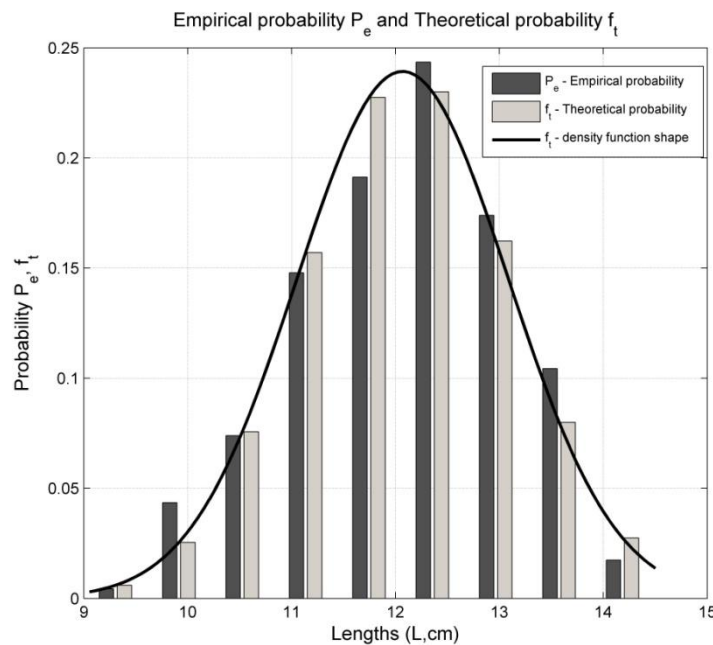
FIGURE 2. HISTOGRAM OF THE EMPIRICAL PROBABILITY P_e, THEORETICAL PROBABILITY f_t AND THE SHAPE OF THE THEORETICAL PROBABILITY DISTRIBUTION OF ANCHOVY LENGTH-FREQUENCY SAMPLE

IV.   CONCLUSIONS

The experimental data distribution (length-frequency commercial fisheries samples of sprat *n*=1000 and anchovy (by-catch) *n*=230 stocks) is tested for normality with chi-square goodness of fit test and results delivered confirm the null hypothesis, stating that data is following the normal distribution.

The procedure developed implies engineering approaches in analysis of statistical data and can be successfully used to confirm assumptions for normally distributed sample data, which one justified, might be successfully used further to facilitate unbiased parametric estimates.

The program developed to support the analysis might be successfully used for testing any sample data and respectively confirm or reject the assumptions for normal distribution of sample data.

ACKNOWLEDGEMENTS

REFERENCES

[1] Cover, T. M. and Thomas, J.A., 2006. Elements of Information Theory 2nd Ed. Hoboken, New Jersey: John Wiley& Sons, Inc., 792p.

[2] Genov, D., 2000. Modeling and Optimization of industrial processes Manual Lab, Varna: Technical university-Varna, 192p.

[3] Hahn, G. J. and Shapiro, S.S., 1967. Statistical Modeling in Engineering, New York, London, Sydney: John Wiley and Sons Inc., 376p.

[4] Lukacs, E., 1942. A Characterization of the Normal Distribution. The Annals of Mathematical Statistics. 13 (1): 91–93.

[5] Lyon, A., 2014. Why are Normal Distributions Normal?, The British Journal for the Philosophy of Science, 65 (3): 621-649.

[6] NIST/SEMATECH e-Handbook of Statistical Methods, 2003, last updated: 10/30/2013:
http://www.itl.nist.gov/div898/handbook/03.11.2017.

[7] Papoulis, A., 2002. Probability, Random Variables and Stochastic Processes (4th Edition). New York: McGraw-Hill Higher Education p.168.

[8] Snedecor G.W and Cochran W.G, 1989, Statistical Methods, 8th Edition, Iowa State University Press, 491p.

[9] Sparre P. and Venema S.C. 1998. Introduction to Tropical Fish Stock Assessment - Part 1: Manual. Rome: FAO Fish Tech. Pap., 306/1 (Rev.2), 407p.

Experimental Study of Hardness Measurement affected by a Cushion between Probe and PTF Pressure sensor

Hideki Toda[1], Natsumi Takata[2], Motoki Okumura[3]

Department of Electric and Electronic Engineering, University of Toyama, 3190 Gofuku, Toyama, 930-8555, Japan

Abstract—In this paper, experimental study of hardness measurement process affected by a cushion between the probe and PTF (polymer thick film) pressure sensor was discussed. Hardness sensing for soft material has been one of the important problems in many fields such as foods industry and material science. One difficulty is how to measure the weak contacting force (0.1 to few N)stable with the small target deformation by low-cost force sensor such as PTF, and we found the result of the measurement stability depending on a cushion between the probe and PTF sensor. The result shows that (1) the output force value depends on the kind of cushion material (plastic, urethane, rubber, styrene elastomer, etc.), (2) the force value was affected by the sensor probe angle to the target material. This result would be useful to develop and study the hardness sensing process intending to reduce the target deformation.

Keywords—Hardness measurement, soft material, cushion, PTF sensor.

I. INTRODUCTION

In this paper, hardness measurement process affected by a cushion between the probe and PTF (polymer thick film) type pressure sensor was discussed. Hardness sensing especially for soft material is one of important problem in many fields such as foods industry and material science, including robotics [1-11].For application, the hardness sensing used many fields such as breast cancer diagnosis [6, 12], tension-type headache from the musculoskeletal complaints [13, 14], trapezius muscle hardness changes from the reason of visual display terminal height [15], muscle hardness measurements using ultrasound [16, 17], hardness sensing using optical (IR frequency) techniques [18].As the force sensor, gauge sensor has been used for the hardness measurement. Since gauge sensor measures a distortion of metal, the accuracy of weak force range (0.1 to few N) inevitably drops, and it is considered difficult to measure the hardness of soft material [3,19-28]. PTF sensor, on the other hand, is designed for weak force range (about 0.1 to 20 N), but the high reliability could not be realized by the instability of the contact area change of the two membranes inside the sensor (Fig. 1a).For example, if the shape of the probe contact terminal to the PTF sensor surface (A) is square, the sensor would be pushed by the linear edge (B) of the probe contact terminal (Fig. 1b), and the probe pushing contact area of the membrane is difficult to change linearly by the pushing force. Since the force is measured proportionally the contact area of the two membranes, the shape and contact area change stability of the probe contact terminal is important factor.
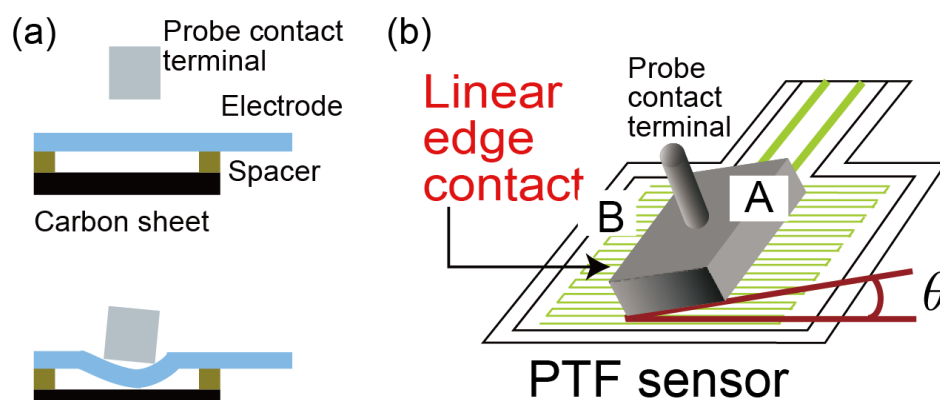
FIGURE 1. EFFECT OF THE SHAPE OF THE PROBE CONTACT TERMINAL CONTACTING WITH PTF SENSOR SURFACE

As shown in Fig.2a, hardness meter is developed by frame, actuator, pushing base, pressure sensor, and "probe body." The probe body contact to the pressure sensor surface and target via the probe part simultaneously. To measure the target object hardness, the actuator force is conveyed to the target via the probe body, and contact situations of the probe body (angle, position, contact place of the target and sensor surface etc.) affect the accuracy and stability of the hardness measurement (Fig.2b). Also, the contact situations cannot control.
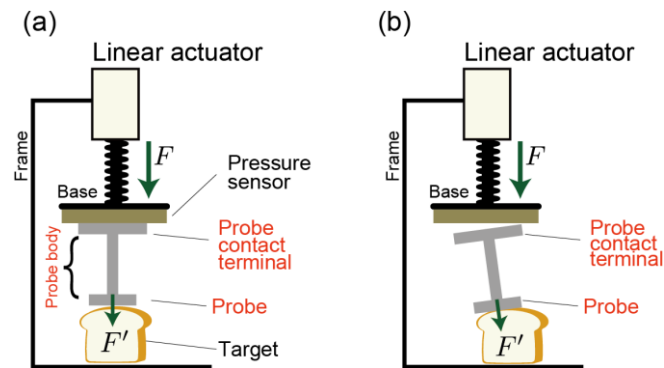
FIGURE 2. EFFECT OF SHAPE OF THE PROBE CONTACT TERMINAL OF THE PROBE.
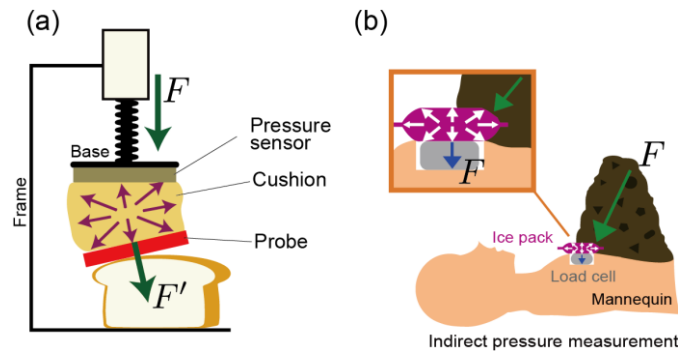
FIGURE 3. (a) ROLE OF THE CUSHION BETWEEN PTF PRESSURE SENSOR AND TARGET MATERIAL. (b) INDIRECT PRESSURE MEASUREMENT OF HUMAN BODY (MANNEQUIN) WHEN SEDIMENT DISASTER BY USING AN ICE PACKS

By adopting a rubber type cushion as the probe body (Fig.3a), it is realized to absorb unevenness of the contact situation, and the target pushing force is correctly transferred to the PTF sensor surface at least. In this paper, the effect of the existence of the cushion as the probe body is examined whiles the hardness measurement.

1.1   Probe body of cushion

As shown in Fig.2a, hardness measurement is realized by a hard material's probe body such as metal, and it is important to control and measure the displacement (indent) of the probe by the pushing force [29-31]. It can be realized by the material hardness of the probe body. On the contrary, by using the cushion as the probe body, the accuracy of the control and measurement of the displacement would be reduced. In our approach, by using a cushion that softer than a metal and harder than the target object, it is designed to perform the deformation (indent) of the target by the force while the probe body is deformed to transmit the force to the sensor surface correctly at the same time [32,33]. This approach is based on the study of indirect pressure measurement of a human body (mannequin) when sediment disaster (Fig.3b) [34].To measure a pressured force applied to the human body by the sediment, they used a load cell buried in the mannequin. But the measurement force of the load cell is unstable, and it is impossible to measure the correct pressured force with most measurement since the applied force by the sediment is not correctly gained to the load cell's sensor part. Their solution is to use an ice pack as the probe body, and the mechanism is that the force applied to one side appears as a reaction force on each side of the ice pack.

The characteristics of the ice pack required here were as follows: (1) be able to deform but return the shape (not broken), (2) spring constant k ($\Delta f = k\Delta x$, Δf is force change, Δx is displacement change) is larger than the target and lower than the metal type probe body. Necessary other characteristics as material were discussed in the result section.

II.   METHOD

Fig.4 shows the developed measurement system. It constructed from a linear actuator (RB-Fir-14, DC 12 V, 100 mm stroke, 12.0mm/sec, Actuonix Corp.), polymer thick film type pressure sensor (FSR402, 0.2 to 100N, Interlink Electronics Inc.) and small size rubber cushion (2 mm diameter, thickness 2.5 mm), and 10 kΩ slider potentiometer, 2 mm thickness acrylic plate (3×3cm). The cushion was positioned on the PTF sensor (Fig.4), and the kind of the cushion (plastic, rubber, gel, sponge, air cushion, ice pack) was changed in the experiment. As mentioned above, the role of the cushion is assumed to convey the correct force between the target material surface and the PTF sensor surface. The displacement of the linear actuator's

pushing distance was measured by a potentiometer inside the linear actuator (10 kΩ). The position accuracy of the potentiometer was about 0.55μm.

The controller was designed as a simple potentiometer's proportional feedback system since the linear actuator's ball screw mechanisms does not realize quick responses, and the fastest convergence time or the controllability is not required in this paper. The force sensor output was measured 12 bit AD board (Arduino Duo, Arduino Corp.) inside PC via operational amplifier OP-07. The force and the potentiometer's output sampling rate were 10 msec.
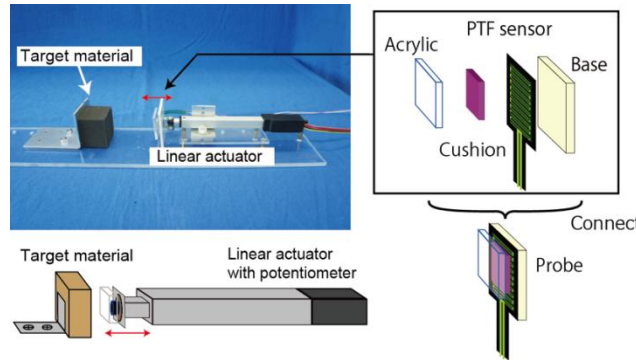
FIGURE 4. EXPERIMENT SETUP OF DEPENDENCIES OF CUSHION MATERIALS.

III.   EXPERIMENT

3.1   Experiment 1: Dependencies of cushion material

In the experiment 1, the dependencies of the kind of the cushion material was examined. Table 1 shows tenmaterial's picture and size list used as the cushion, and Table 2 means the material, product name and rough estimate of Young's modulus. As target material, urethane foam sponge (30×30×50 mm, Young's modulus σabout 20 kPa, No-#1, Yahata-neji Corp.) was used, and the key point of the target material was that the $\sigma$was lower (about one tenth)than the cushion material σ.

TABLE 1
SPECIFICATION OF CUSHION MATERIALS

Name	Beads1	Beads2	Rubber1	Rubber2	Sponge	Air Cushion	IcePack	Plastic plate	Gel1	Gel2
Picture										
Shape	●	●	◓	◓	⬭	Soft	Soft	☐	☐	⬭
Diameter (size)[mm]	4.1	7.9	11.2	9.5	20	10	32×31	9×9	9×9	30
Thickness [mm]	4.1	7.9	5.1	3.8	2.0	3.0	9.0	3.0	3.0	3.0

TABLE 2
MATERIAL NAMES AND YOUNG'S MODULUS OF THE CUSHION MATERIALS

Name	Material	Product name, Corporation	Young's modulus [kPa]
Beads1	Plastic (PP)		~30000
Beads2	Plastic (PP)		~30000
Rubber1	Poly urethane	PS-10R, Exseal Corp.	~1000
Rubber2	Poly urethane	PS-8R, Exseal Corp.	~1000
Sponge	Urethane rubber	CN-102, Waki company	~100
Plastic Plate	Plastic (PVC)		~50000
Ice Pack	Polymeric water-absorbing polymer	HC-100PL, Catch-cool, Try Corp.	
Air Cushion	Air and thin vinyl		
Gel1	Styrene elastomer	Super gel shock absorbing sheet, ACTIKA Corp.	~200
Gel2	Urethane elastomer	GEL7, Seiwa-pro Corp.	~200

The experiment process was divided into three phases.(1) Contact phase: The sensor probe was approached to the target surface by using the linear actuator with a low speed (about 1mm/sec) and it stops the linear actuator when the force sensor changes over 6 S.D. from the 0 N. In the system, the base noise of the force sensor is 0.0005 N (6 S.D. = about 0.003 N). (2) Pushing 3 mm constant distance: The force sensor was pushed 3 mm constant distance to the target material. The linear actuator's ball screw mechanism realizes the constant distance control by not difficult control algorithm. The bang-bang control for controlling the force sensor distance was used.(3) Waiting until the force curve is attenuated: After the pushing process, the position of the sensor probe was fixed with 7 sec. The sensor probe was pushed 3 mm with the longitudinal direction of the target foam sponge (Fig.5a), and it was repeated five times. By changing the kind of cushion (Beads1 to Plastic plate), the measurement force and the stability were confirmed.
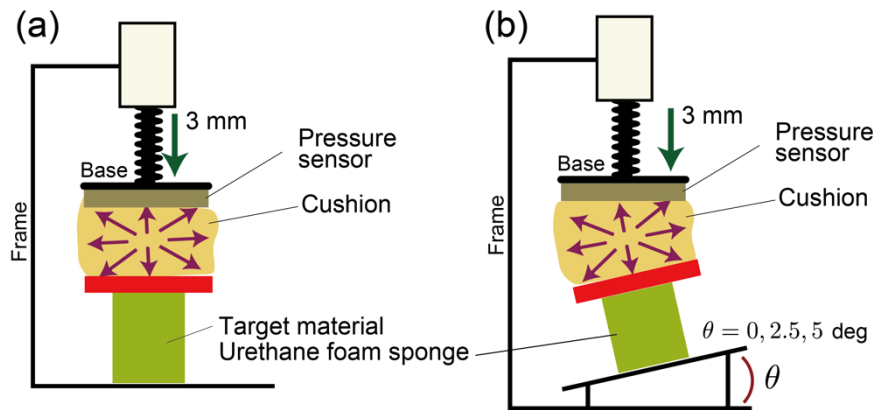
FIGURE 5. EXPERIMENT SETUP CONDITIONS OF (a) EXPERIMENT 1AND (b) EXPERIMENT 2.

3.2 Experiment 2: Dependencies of the sensor probe angle

In experiment 2, the dependencies of the sensor probe angle were examined using (a) Plastic plate and (b) Gel2 in Table 1 as the cushion. The experiment process was same with experiment 1.

IV. RESULT

The result of experiment 1 was shown in Table 3 and Fig.6. The force F represents the average of the PTF sensor output after 7 sec attenuation when 3 mm pushing process, and S.D. of F means the standard deviation of the F (N=5). Since the F was not taken a constant value, the S.D. of F was normalized by F using formula $\frac{S.D.of\ F}{F} = s$ and the result was summarized in Table 3 and Fig. 6. When the value takes a low value, it means the measurement was a stable one.

The result was summarized below: (1) When the cushion was hard material (Beads1, Beads2), s takes a high value (>0.3) though the shape of the cushion is a sphere (Table3 and Fig. 6).It means that to reduce the effect of angle dependencies of the sensor probe, the point contact (because it is a sphere) has not better effects to the sensor output of the PTF. (2)Round shape polyurethane rubber (Rubber1, Rubber2) result takes almost same or relatively small value of s. It means that in the range of 1000 kPa material, the shape of the cushion was not important. (3) To comparing the previous study of the indirect pressure measurement of a human body (mannequin) [34] (Fig.3b), small sized Ice pack (Fig. 6B) was used, and the result was good comparing with Sponge (100 kPa) or Plastic plate (50000 kPa, Fig. 6A).(4) Soft materials (Air Cushion, Gel1, Gel2) got good performance (around 0.13)of s. It means that about 200 kPa range of Young's modulus was necessary to measure the hardness of the urethane foam sponge (about 20 kPa).

TABLE 3
RESULT OF EXPERIMENT 1

	Beads1	Beads2	Rubber1	Rubber2	Sponge	Plastic plate	IcePack	Air Cushion	Gel1	Gel2
Picture										
F[N]	1.32	1.3	1.4	2.05	2.31	2.03	2.79	2.7	2.78	3.1
S.D. of F [N]	0.45	0.43	0.46	0.48	0.44	0.37	0.49	0.37	0.38	0.39
Normalize S.D. by F	0.34	0.32	0.33	0.23	0.19	0.18	0.17	0.14	0.14	0.13
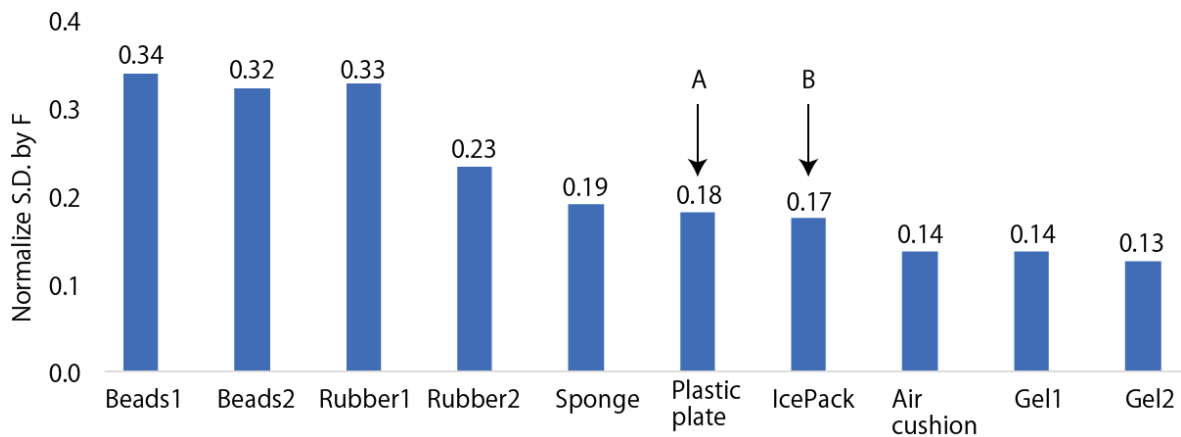
FIGURE 6. NORMALIZED STANDARD DEVIATION BY F OF THE RESULT OF EXPERIMENT 1

The result of experiment 2 was shown in Fig.7. Fig. 7(a) was the case of the Plastic plate as the cushion. The output force value F was measured in the case of 3 mm pushing while 10 sec. The reason of using the Plastic plate was that even if Young's modulus takes a high value, the s was measured as a small value. This characteristic mainly depended on the size of the plate, and the 9×9 mm size plate led maximum performance in our experimental setup (it related to the size of the PTF sensor). However, in the case of the Plastic plate cushion, the F was decreased by the change of the pushing angle (the condition was Fig.5b), and the force convergence curve was not stable. On the other hand, Fig. 7(b) shows the case of Gel1, and it was converged one value (3.18±0.08 N, N=5) in each angle settings.
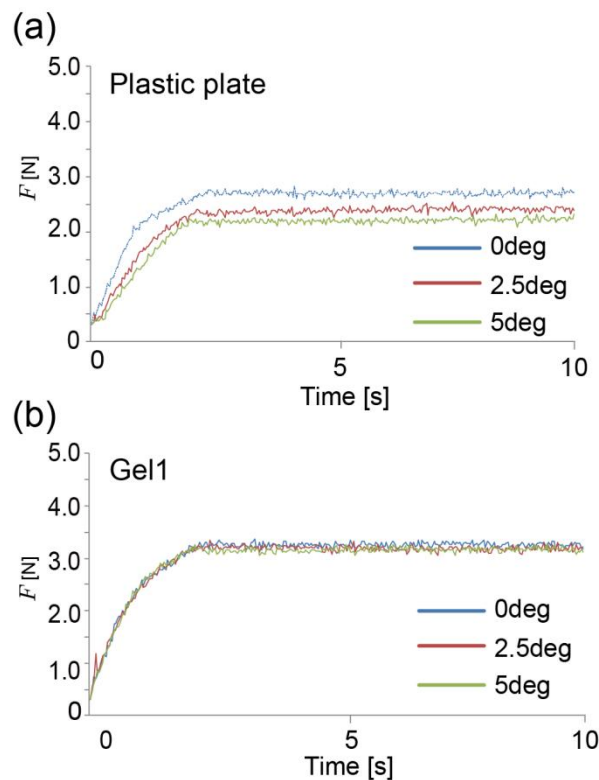
FIGURE 7. RESULT OF EXPERIMENT 2. THE CASE OF PLASTIC PLATE AND GEL1.

V. CONCLUSION

In this study, experimental study of hardness measurement process affected by a cushion between the probe contact terminal and PTF pressure sensor was discussed. The result of experiment 1 shows that the material kind of the cushion is important for the stable measurement of the force. Shock-absorbing gel (Gel1, Gel2) was effectively work for transmitting the pushing force to the PTF sensor surface. The result of experiment 2 shows that the pushing angle of the sensor probe was affected to the force measurement and the divergence of the force could be suppressed by using shock absorbing gel (Gel1, Gel2). This result would be useful for developing a low-cost hardness measurement system for soft material.

REFERENCES

[1] M. Taguchi, G. Nakajima, S. Maeda, T. Yoshino, "Toward to ensure fruit and vegetables of safety and security - the use of fruits and vegetables of the traceability system", ISFJ Japan policy Student Conference, 2010.

[2] K. Sakamoto, Y. Muratani, S. Omata, "Fundamental research on the development of surgical support device", SICE Tohoku branch, No. 198 Workshop, 198-9, pp.1-4, 2001.

[3] M. Tanaka, T. Adachi, Y. Tanahasi, S. Chonan, "Development of An active Palpation Sensor for Detecting Prostatic Cancer and Hypertrophy", Japan Society of Mechanical Engineers, Annual Conference Papers (I), 2002.

[4] A. Shigetaka, H. Takashi, H. Eiichiro, M. Kazuhiko, K. Shinken, "Non-invasive Measurement of Intracranial Pressure via the Anterior Fontanelle: New Method for Fixation of the Measuring Apparatus", Neurologia medico-chirurgica, Vol. 26(4), pp. 291-295, 1986-04-15.

[5] E. Honda, T. Hayashi, T. Masasima, S. Anegawa, T. Kikukawa,"A New Instrument for Non-invasive Measurement of Intracranial Pressure via the Anterior Fontanelle.", Neurol. Med. Chir., Vol. 22, pp.640-648, 1982.

[6] I. Kato, K. Koganezawa, A. Takanishi, "Automatic Palpation System for Breast Cancer: WAPRO-4", Journal of the Robotics Society of Japan, Vol. 5(2), pp.102-108, 1987.

[7] H.G. Muller, "An lntroduction to Food Rheology", pp. 1-16, 1973.

[8] American Association of Cereal Chemists: Cereal laboratory methods, Staleness of bread compression test with baker compressimeter, AACC Method, Vol. 74-10, 1961.

[9] D.W.E Axford , K. H. Colwell , S.J. Conford , G.A.H. Elton , "Effect of loaf specific volume on the rate and extent of staling in bread", Journal of Science of Food and Agriculture, Vol. 19, pp. 95-101, 1968.

[10] Neuroinfo Japan HP, "Neurosurgical disease information", available from <http://square.umin.ac.jp/neuroinf/medical/601.html>, (accessed 2017-10-31).

[11] Japan hydrocephalus Association, "hydrocephalus Guidebook 2002", available from <http: // www.suitoushou.net/guide.html>, (accessed 2017-10-31).

[12] M. Tanaka, M. Tamura, T. Okuyama, "Study on a roller scanning type palpation sensor", International Journal of Applied Electromagnetics and Mechanics, DOI: 10.3233/JAE-141899, Vol. 45, No. 1-4, pp. 723-729, 2014.

[13] K. Maeda, "Occupational Cervicobrachial disorder and its causative factors", J. Human Ergol., Vol. 6 (2), pp. 192-202, 1977.

[14] F. Sakai, S. Ebihara, M. Akiyama, H. Horikawa, "Pericranial muscle hardness in tension-type hcadache; A non-invasive measurement method and its clinical application", Brain, Vol. 118, pp. 523-531, 1995.

[15] M. Horikawa, "Effect of visual terminal height on the trapezius muscle hardness: quantitative evaluation by a newly developed muscle hardness meter", Applied Ergonomics, Vol. 32, pp. 473-478, 2001.

[16] J. L. Gennisson, C. Cornu, S. Catheline, M. Fink, P. Portero, "Human muscle hardness assessment during incremental isometric contraction using transient elastography", Journal of Biomechanics, Vol. 38 (7), pp. 1543-1550, 2005.

[17] O. Yanagisawa, M. Niitsu, T. Kurihara, T. Fukubayashi, "Evaluation of human muscle hardness after dynamic exercise with ultrasound real-time tissue elastography: A feasibility study", Clinical Radiology, Vol. 66, No.9, pp. 815-819, 2011.

[18] U. Bindig, I. Gersonde, M. Meinke, Y. Becker, G. Muller, "Fibre‐optic IR‐spectroscopy for biomedical diagnostics", Spectroscopy, Vol. 17, No. 2,3, pp. 323-344, 2003.

[19] N. Tomotake, H. Watanabe, J. Matuoka, Y. Jinou, R. Koga, "A study of static stretching time and its effect of using the muscle hardness tester", Japanese Journal of Sports Injuries, Vol. 17, pp.37-39, 2012.

[20] T. Koeda,"Hardness measurement of vivo by muscle hardness meter - reproducibility and validity and usefulness -", Nagoya Gakuin University Studies, humanities and natural sciences (Japanese), Vol. 46, No. 2, 2010.

[21] S. Suzuki et al., "Individual Muscle Stretching", ISBN978-4-89590-475-9, pp.36-39, 2006.

[22] O. Ooshiro, et al., "Analysis of local elastic modulus in MR Elastography of using the instantaneous frequency method", MEDICAL IMAGING TECNOLOGY, Vol.18, No.2, 2000.

[23] M. Nagao, T. Endo, O. Yokota, "Correlation between Questionnaire Survey and Muscle Hardness in Shoulder Stiffness", SICE Tohoku Branch No. 268 Workshop, 268-6, 2011.

[24] D. Ishikawa, T. Uchiyama, "Development of portable digital muscle hardness meter using indentation method", Bio mechanism Journal, Vol. 30 (4), pp. 234-237, 2006-11-01.

[25] Kind of hardness sensor, Elastron HP, available from <http:// www.elastron.co.jp / about.html>, (accessed on 2017-10-31).

[26] T.M. Junisbekov, "Stress Relaxation in Viscoelastic Materials", ISBN 1-57808-258-7, 2003.

[27] S. Moromugi, S. Kumano, M. Ueda, T. Ishimatsu, M. Q. Feng, T. A. Tanaka, "Sensor to measure hardness of human tissue", Sensors, 2006, 5th IEEE Conference on 2006, DOI: 10.1109/ICSENS.2007.355487, pp. 388 - 391, 2006.

[28] T. Koeda,"Hardness measurement of vivo by muscle hardness meter - reproducibility and validity and usefulness -", Nagoya Gakuin University Studies, humanities and natural sciences (Japanese), Vol. 46, No. 2, 2010.

[29] Y. Maeda, K. Terao, T. Suzuki, F. Shimokawa, H. Takao, "A tactile sensor with the reference plane for detection abilities of frictional force and human body hardness aimed to medical applications", Micro Electro Mechanical Systems (MEMS), 2015 28th IEEE International Conference on 2015, pp. 253-256, DOI: 10.1109/MEMSYS.2015.7050936, 2015.

[30] Z. Shenshen, D. Parks, L. Chang, "Design and Modeling of a Wide Dynamic-Range Hardness Sensor for Biological Tissue Assessment", Sensors Journal, IEEE, Vol.13, Issue 12, DOI:10.1109/JSEN.2013.2271736, pp. 4613-4620, 2013.

[31] L. Zizhen, K. Yeung, "On Preconditioning and Stress Relaxation Behaviour of Fresh Swine Skin in Different Fibre Direction", International Conference on Biomedical and Pharmaceutical Engineering 2006, ICBPE 2006, pp.221-226, 2006.

[32] O. Motoki, T. Hideki, "Development of softness measurement technique using a flexible probe and a constant distance pushing for infant hydrocephalus inspection", The Robotics and Mechatronics Conference 2015, ROBOMECH2015 in Kyoto, ID: 19921203, 2015.

[33] O. Motoki, T. Hideki, "Proposal of Low Deformation Hardness Sensing Method by Constant-Displacement Pushing without Force Control", International Conference of u-Healthcare 2015, Kinki University Japan, Nov.30-Dec.2, P1-19, 2015.

[34] T. Satoru, T. Jin, O. Akihiro, "Full scale model experiment on working pressure at burial sediment", (japanese), Society of Biomechanisms Japan, SOBIM 2016, Toyama, pp. 213-216, 2016.

A novel study on the degradation of styphnic acid from water by cold plasma technology

Nguyen Cao Tuan[1], Nguyen Van Hoang[2], Dang Kim Chi[3]

[1,2]Institute of New Technology
[3]Hanoi University of Science and Technology

Abstract— *Cold plasma technology exhibits many advantages in practical application. Due to these reasons the use of cold plasma technology for environmental treatment is receiving great attention. Here a novel study on the degradation of styphnic acid from water by cold plasma technology has been presented in detail, such as establishment of cold plasma reactor structure, determination of efficiency in degradation of styphnic acid by cold plasma radiation under different experimental conditions. The obtained results have shown that cold plasma might be used for degrade styphnic acid with high efficiency.*

Keywords— *cold plasma, degradation, acid styphnic.*

I. INTRODUCTION

Styphnic acid (TNR) or 2,4,6 trintro-1,3 benzenediol with formula $C_6H_3N_3O_8$ is used in manufacturing dyes, pigments, inks, medicines, explosives (led styphnate) [1]. Styphnic acid is one of aromatic nitro compounds, with synonyms: 2,4,6-trinitroresorcine, 2,4,6- trinitroresorcinol ranging from slight to strong oxidizing agents. It may explode in the presence of a base such as NaOH or KOH even in the presence of water or organic solvents. So that this compound is always kept away from heat, sparks and avoided from mechanical shock [2]. Styphnic acid can cause eye, skin and being harmful if inhaled, swallowed or absorbed through the skin. It is also toxic for blood, kidney and nervous system, causing cancer and aquatic life *[3]*. Like aromatic nitro compounds, the styphnic acid contaminated water may be treated by many methods such as physical, chemical [4].

In recent years, plasma plays an important role in variety of industrial applications. including material processing, environmental treatment and many more. There are increasing interests in the plasma discharges in liquids because of its potential applications for various fields like biological, environmental, and medical technologies. In this paper a novel study on the degradation of TNR from water using cold (non thermal) plasma technology was presented. The chief aim of study is to degrade TNR from plant wastewater resulting from the manufacture of lead styphnate to avoid explosive hazard. Plasma is an ionized gas that is the fourth state of matter after solid, liquid and gas. Plasma technology has been studied and applied for wastewater treatment in recent years, involving many advantages compared with chlorination, ozonation and UV. Principle of plasma is based on the formation of free radicals and strongly oxidative species under electric discharge with high voltage through a dielectric barrier in air at atmosphere pressure as following [5-8]:

- Reactions producing ozone

$$O_2 + h\nu \rightarrow O + O$$

$$O_2 + O \rightarrow O_3$$
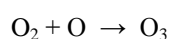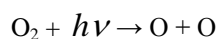
- Reactions producing free species

$$O_3 + OH^- \rightarrow O_3^{\bullet -} + {}^{\bullet}OH$$

$$O_3^{\bullet -} \rightarrow O^{\bullet -} + O_2$$

$$O^{\bullet -} + H_2O \rightarrow {}^{\bullet}OH + OH^-$$
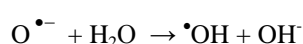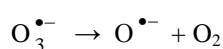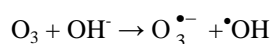
The main oxidative species is hydroxyl free radical with the high reduction potential 2.80 V might degrade recalcitrant organic compounds like TNR from water as follows:

$$C_6H_3N_3O_8 \xrightarrow{oxidative species ({}^{\bullet}OH)} Products$$
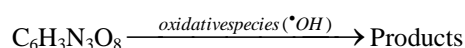
II.   EXPERIMENTAL PART

2.1   Chemicals:

Styphnic acid with analytical purity grade purchased from China.

Other chemicals such as methanol (Merck, Germany), and NaOH, H_2SO_4, H_2O_2 with analytical purity grade purchased from China too.

2.2   Apparatus

-    HPLC Model HP 1100, using *diode-array detector*. (DAD), Agilent (USA),

-    Spectrophotometer UV- Vis Agilent 8453 (USA),

-    DR/890 Colorimeter, HACH, for COD analysis.

The schematic structure of plasma reactor shown in the Fig 1.
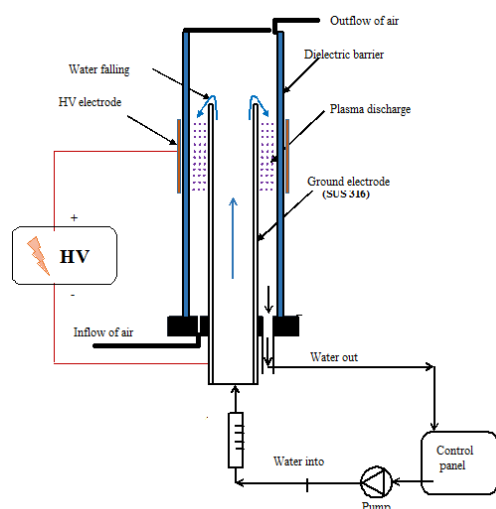
FIG.1. SCHEMATIC STRUCTURE OF PLASMA REACTOR

2.3   Experimental procedure

The experimental procedure is focused on studying the following items:

2.3.1   Formation of cold plasma

The appearance of cold plasma will carried out under conditions like electric current varying from 3.5 to 22 mA and electrode potential increasing from 7 to 21 kV (HV). Plasma intensity appeared is recognized by the naked eyes and through TNR degradation efficiency.

2.3.2   Degradation of TNR from water in varying electric power

To increase the degradation of process, the plasma is in direct contact with the thin film of water falling via a grounded electrode. The TNR contaminated water sample is always circulated through reactor during the reaction proceeding, with the rate of 415 mL/minute and the air rate blowing with 3 liter/min. The degradation of TNR is carried out under the conditions such as: volume of sample is 500 mL containing a certain concentration of TNR, pH of samples from 3.2 to 11 at different electric power. After an interval of reaction time, a certain volume of sample is taken out to measuring the TNR concentration left, by HPLC method as suggested in [9].The removal of efficiency of styphnic acid is calculated using the expression:

$$H = \frac{(C_0 - C_t)}{C_0} \times 100, \text{ (\%)}$$

Here H is removal efficiency of TNR. C_0 and C_t are concentrations of styphnic acid at the initial and t reaction time, mg/L.

The average rate of TNR degradation is also calculated by the expression:

$$r = \frac{(C_{t_1} - C_{t_2})}{\Delta t}$$

Here r denoted the average reaction rate (mg/l.min), Δt is the time interval from t_1 to t_2, min.

2.3.3   Study on increasing degradation efficiency

The experimental method was implemented like 2.3.2 but using H_2O_2 in addition

2.3.4   Study on other factors influencing degradation efficiency of TNR

- Influence of initial concentration of TNR, the experiments are carried out like in 2.3.2 but varying initial concentration of TNR.

- Influence of pH, the experiments were implemented like in 2.3.2, but the pH varying from 3.2 to 11.

III.   RESULTS AND DISCUSSION

3.1   The appearance of plasma

The images of plasma discharges in reactor are presented in Fig.2

U= 7 kV I = 3.5 mA	U= 14kV I=5.5 mA	U=16kV I= 10 mA	U=19 kV I = 16 mA	U= 21kV I = 22 mA
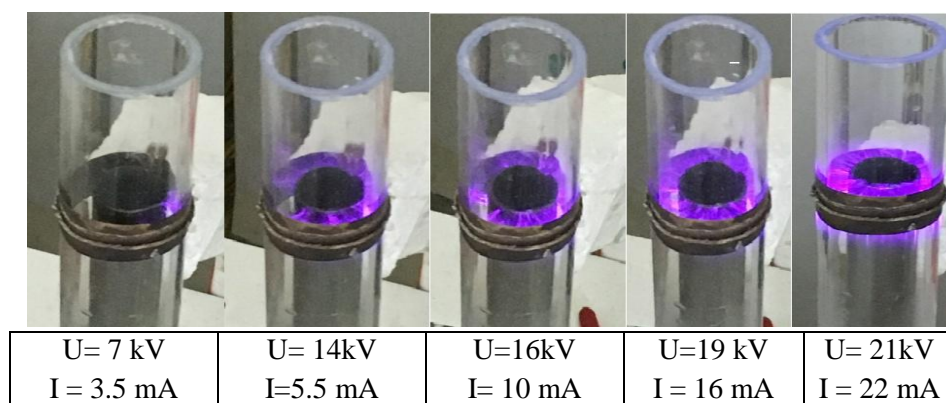
FIG.2. THE APPEARANCE OF PLASMA IN VARYING CONDITIONS OF U AND I

Under condition such as U = 21kV, I =22 mA, intensity of plasma radiation is observed to be the highest.

3.2   The degradation of TNR in varying plasma discharge

The results of TNR degradation about efficiency and reaction rate, under the varying plasma discharge such as U and I were presented in Table 1 and in Fig.3.

TABLE 1
INFLUENCE OF PLASMA DISCHARGE ON TNR DEGRADATION

Reaction time, min	TNR degradation								
	I=10mA, U=16kV			I=16mA, U=19kV			I=22mA, U=21kV		
	C_t, mg/L	H, %	r, mg/l.min	C_t, mg/L	H, %	r, mg/l.min	C_t, mg/L	H, %	r, mg/l.min
0	115.60			115.60			115.60		
30	94.75	18.04	0.70	75.28	34.88	1.34	15.25	86.80	3.34
60	79.21	31.48	0.52	45.13	60.96	1.01	1.34	98.84	0.46
90	66.97	42.07	0.41	20.26	82.47	0.83	0.77	99.33	0.02
120	54.48	52.87	0.42	7.72	93.32	0.42	0.00	100.00	0.03
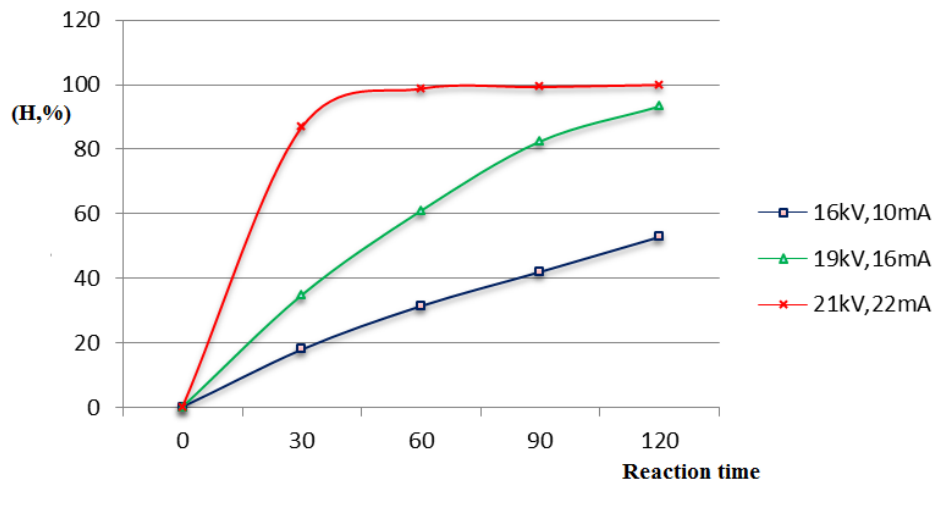
FIG.3. TNR DEGRADATION EFFICIENCIES VERSUS TIME

The obtained data have shown that the TNR degradation depends on the plasma discharge. Under the conditions such as U =21 kV, I = 22 mA, plasma discharge reaches the highest state.

3.3   Influence of pH on the TNR degradation

The results of influence of pH on the TNR degradation was presented in Table 2.

TABLE 2
INFLUENCE OF PH ON TNR DEGRADATION

Reaction time, min	TNR degradation								
	pH = 3.2			pH = 7.0			pH = 11.0		
	C_t, mg/l	H, %	r, mg/l.min	C_t, mg/l	H, %	r, mg/l.min	C_t, mg/l	H, %	r, mg/l.min
0	115,60			115.6			115.6		
30	75.28	34.88	1.34	77.08	33.32	1.28	74.36	35.67	1.37
60	45.13	60.96	1.01	46.62	59.67	1.02	43.59	62.29	1.03
90	20.26	82.47	0.83	20.14	82.58	0.88	16.87	85.41	0.89
120	7.72	93.32	0.42	7.07	93.88	0.44	2.2	98.10	0.49

The obtained experimental data has shown that at the pH =11, the TNR degradation efficiencies and reaction rate are higher at pH= 11.Due to that at this pH, the ozone resulting in plasma discharge is easily converted in hydroxyl radical. This radical is more reactive in alkaline medium the in acid or neutral one that has suggested in [10].

3.4   Influence of TNR initial concentration on degradation

The TNR degradation efficiency under cold plasma condition depends on the initial concentration of TNR, presented in Table 3 and in Fig.4.

TABLE 3
INFLUENCE OF INITIAL CONCENTRATION ON TNR DEGRADATION

reaction time min	TNR degradation								
	C_{TNR} =61.72 mg/L			C_{TNR} =115.6 mg/L			C_{TNR} =175.03mg/L		
	C_{TNR} mg/L	H, %	r, mg/l.min	C_{TNR} mgL	H, %	r, mg/l.min	C_{TNR} mg/L	H, %	r, mg/l.min
0	61.72			115.60			175.03		
30	27.15	56.01	1.15	75.28	34.88	1.34	132.25	14.16	1.43
60	9.72	84.25	0.58	45.13	60.96	1.01	99.19	31.90	1.10
90	1.36	97.80	0.28	20.26	82.47	0.83	72.23	53.02	0.90
120	0.00	100.00	0.05	7.72	93.32	0.42	53.15	69.63	0.64
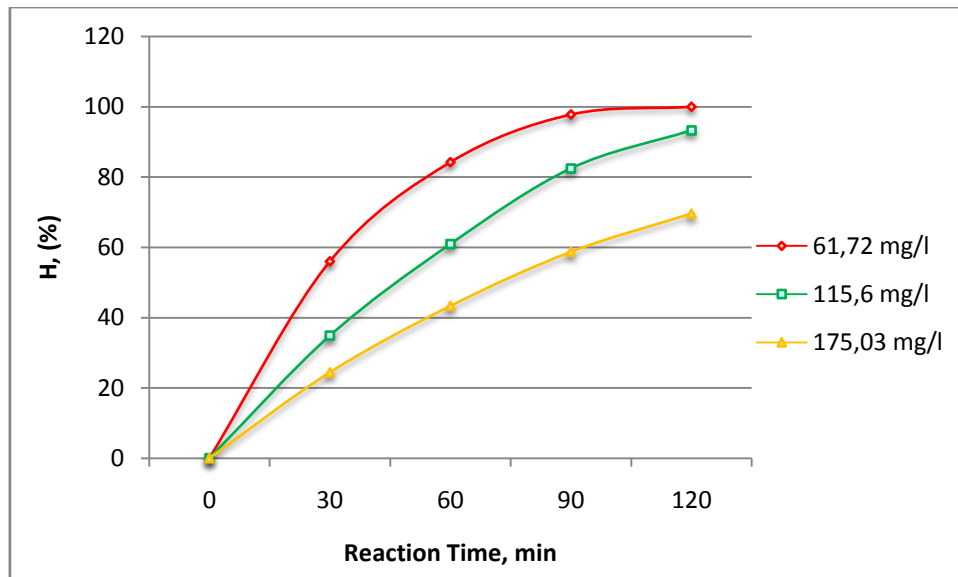
FIG. 4. TNR DEGRADATION EFFICIENCIES AT DIFFERENT CONCENTRATIONS

The obtained experimental data have shown that at the same plasma discharge and at the initial concentration of TNR of 61,72 mg/L, after 120 min, the TNR degradation efficiency reach 100 %, at the same time the TNR degradation efficiencies are 93.32 and 69.63 % for the TNR initial concentrations of 11.60 and 175.03 mg/L respectively. This is really true due to the plasma discharge limited.

3.5   Increase of TNR degradation efficiency by plasma discharge combined with H_2O_2.

The addition H_2O_2 into plasma reaction might enhance TNR degradation, presented in Fig. 5.
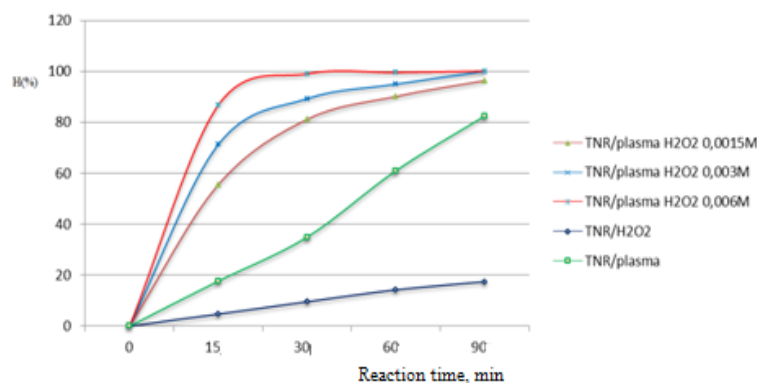
FIG. 5. TNR DEGRADATION EFFICIENCY BY PLASMA COMBINED WITH H_2O_2

The obtained experimental data have shown the presence of H_2O_2 increases the TNR degradation efficiency. The high efficiency might explain by the activation of H_2O_2 by plasma (UV) in plasma reactor to produce hydroxyl radical as follows:

$H_2O_2 + hv \rightarrow HO^{\bullet} + {}^{\bullet}OH$
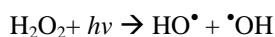
The increase of hydroxyl radical leads toincrease the TNR degradation efficiency.

3.6   Proposed TNR degradation rate expression by cold plasma

The degradation of TNR in water sample under the plasma discharge is due to the formation of oxidative species, mainly hydroxyl free radical (OH•). Under the same condition of plasma discharge, the total oxidative species are constant amount, the TNR degradation rate expression is normally is following:

$$r = - k[OH][TNR] = - k_{app}[TNR]$$

Here denoted $k[OH] = k_{app} = $ constant.

In this case the degradation rate of TNR should be proportional to TNR concentrations. The plot in Fig. 6 (a) has shown there is no proportional to TNR concentration. In the other hand there is a good proportional relationship between 1/rate and 1/TNR concentration Fig.6 (b).
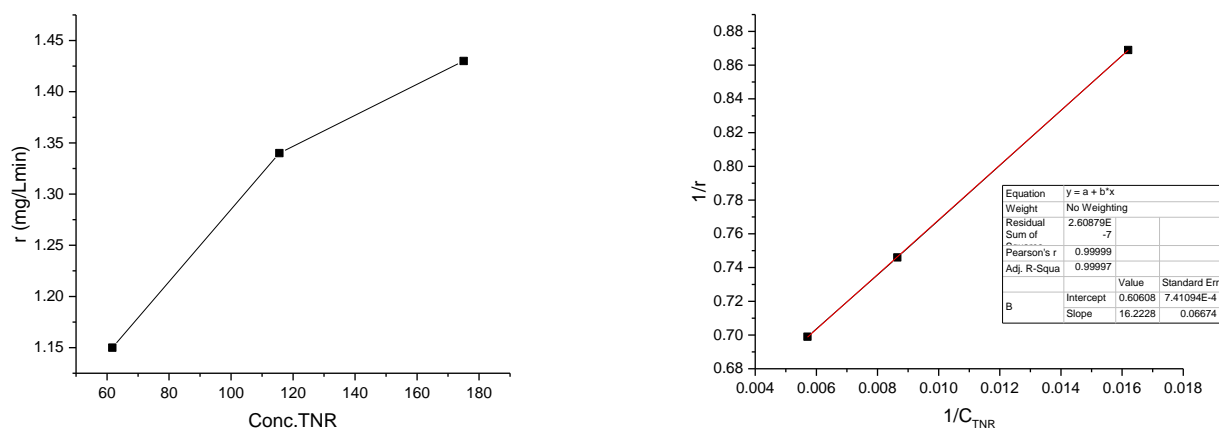
FIG. 6. THE PLOTS OF THE REACTION RATE AND TNR CONCENTRATION

But from data in the Table 3 the rate expression of TNR degradation fits to the formula as follows:

$$- r = \frac{k_1[TNR]}{1 + k_2[TNR]}$$

Here k_1 and k_2 are constants, [TNR] is TNT initial concentration. This proposed expression is in accordant with the work [11]. The k_1 and k_2 will be determined in the further article.

IV.   CONCLUSIONS

In this paper a novel study of cold plasma technology was presented. The use of cold plasma discharge for degradation of TNR from water was studied in detail. The main factors such as the reaction time, pH, TNR initial concentration, H_2O_2 and electric power influencing on the plasma resulting in and on TNR degradation efficiency were determined. By cold plasma, the TNR degradation efficiency might reach 100% for 120 min, when the initial TNR concentration is 61.72 mg/L.

REFERENCES

[1] *Armarego, W.L.F.; Chai, C.L.L. (2003).* Purification of Laboratory Chemicals. *Butterworth-Heinemann. p. 353.* ISBN 9780750675710. Retrieved 2015-05-20.

[2] Arthur Finch John Payne 1990, Thermochemistry of nitroresorcinols, 2,4,6- trinitroresorcinol(styphnic acid). Thermochimica Acta Volume 170, 12Pages 209-212

[3] Brown, G.I. (1998) The Big Bang: a History of Explosives Sutton Publishing ISBN 0-7509-1878-0 pp.151–163].

[4] Peroxygen Talk. "Choosing the Right Activator", Jan2006. (www.klozur.com).

[5] A.A. Joshi, B.R. Locke, P. Arce, W.C. Finney , "Formation of hydroxyl radicals, hydrogen peroxide and aqueous electrons by pulsed streamer corona discharge in aqueous solution", Journal of Hazardous Materials, vol. 41, pp. 3-30, 1995.

[6] M. Dors, J. Mizeraczyk, Y.S. Mok, Phenol Oxidation in Aqueous solution by Gas Phase Corona Discharge, Journal of AdvancedOxidation Technologies, 9, 139-143, 2006.

[7] M. Dors, E. Metel, J. Mizeraczyk, Phenol Degradation in Water by Pulsed Streamer Corona Discharge and Fenton Reaction, Int. J. Plasma Environ. Sci. Technol., 1, 76-81, 2007.

[8] Sunka P, Babicky V, Clupek M, Lukes P, Simek M, Schmidt J and Cernak M 1999 Generation of chemically active species by electrical discharges in water Plasma Sources Sci. Technol. 8 258–65.

[9] Ronald L. Yates and Donal C, Havery, Cosmet. Sci., 50, 315-325 (September/October 1999) Determination of phenol, resorcinol, salicylic acid and -hydroxy acids in cosmetic roducts and salon preparations .

[10] Yong Hee Kim, Young June Hong, Ku Youn Baik, Measurement of Reactive Hydroxyl Radical Species Inside the Biosolutions During Non-thermal Atmospheric Pressure Plasma Jet Bombardment onto the Solution. Plasma Chemistry and Plasma Processing, May 2014, Volume 34, Issue 3, pp 457–472.

[11] Do Young KimMeng-Wen Chang, Tai-Shang Chen, and Jia-Ming Chern, 2008. Initial Degradation Rate of p-Nitrophenol in Aqueous Solution by Fenton Reaction, Ind. Eng. Chem. Res.,47,8533–8541.

Preparation of Oligo (Hexene-1-So-Indenes) and Investigation of Its Products as Additives to Oils

A.M.Hasanova[1], F.Y.Aliyev[2], S.B. Mammadli[3], D.R.Nurullayeva[4], B.A. Mammadov[5]

[1,2]Ganja Department of Azerbaijan National Academy of Sciences, Azerbaijan
[3,4,5]Institute of Polymer Materials of Azerbaijan National Academy of Sciences, Azerbaijan

Abstract— *It has been carried out the copolymerization reactions of hexene-1 and indene with participation of $BF_3 \cdot O(C_2H_5)_2$ as the catalyst, the yield, the composition, the structure, the copolymerization constant and the average molecular weight values depending on cooligomerization condition have been determined. It has been shown that a location of links in the prepared cooligomers has a statistic character, but the blocks organized by molecules of hexene-1 may be included. Thermal stability of the synthesized cooligomers of hexene-1-indene has been investigated both individually and in fatty solution and it has been elucidated that an increase of a quantity of indene links in cooligomer composition leads to increase of thermal stability and an increase of the molecular weight decreases a thermal stability. An inclusion of the synthesized cooligomers in composition of M-6 oil as synthetic component increases a viscosity index value and gives it anticorrosion property.*

Keywords— *hexene-1, indene, viscosity-temperature additives.*

I.   INTRODUCTION

Using the oligomer and cooligomer as synthetic component in the composition of the oils one can prepare the oils with high viscosity index [1-3]. Most of the oils intended for surface technique are prepared by this method, so they are mixed with 1-alkene oligomers and cooligomers at various ratios.

The numerous investigations have been carried out in the direction of use of cooligo- and copolymers of 1-alkenes with a number of vinyl monomers and dicyclopentadiene as additives to petroleum oils [4-8]. At the same time a use of hexene-1 as a basic monomer and also its copolymers with indene as viscous additives for oils is also of interest. It was known that an introduction of the aromatic fragments in polymer chain increases their stability to actions, and an introduction of dicyclopentadiene fragments leads to that the prepared macromolecular compounds show anticorrosion and depressor properties in the composition of lubricating oils. The indene molecule combines both aromatic and carbocyclic fragment, therefore it is subjected to cooligomerization with hexene-1.

II.   EXPERIMENTAL

For cooligomerization it was used freshly distilled hexene-1 and indene, as the catalyst – $BF_3 \cdot O(C_2H_5)_2$. The process is carried out methodologically as follows. After addition of the calculated quantity of monomer mixture of hexene-1-indene and hexane or heptane as a solvent to a flask equipped with mixer, thermometer and drop funnel the mixer is activated and the reaction temperature in the flask is created by cooling bath. The catalyst $BF_3 \cdot OEt_2$ is introduced into the system as a solution through the drop funnel. The catalyst feed rate is adjusted so that the temperature in the flask should not be higher 415K. After the temperature rise, the reaction mass is additionally stirred for 1 h to complete the reaction, so that the reaction should be completed. Then the catalyst complex is decomposed by 2-3% alkaline solution, washed with water-isopropyl alcohol (not to form emulsion) to neutral medium, filtered, the solvent and easy part is distilled, a yield of the prepared oligomer compound, kinematic viscosity and molecular weight value is determined.

The composition and structure of the synthesized compounds have been investigated by methods of IR- and NMR-spectroscopy, elemental analysis (determination of composition on carbon) and fractional composition. The IR-spectra have been taken on Varian 640 IR FTIR spectrometer, Specord M 80 (Carl Zeiss Jena) and Spectroscopy FTIR Nicolet is 10 devices. The NMR-spectra have been taken on the device 300 MHz "Bruker" using CCl_4. For investigation of some points it has been used the device 90 MHz "Perkinq Elmer".

The thermal analysis of hexene-1-indene cooligomers has been carried out in nitrogen atmosphere in derivatography of OD-102T type (Paulic-Paulic-Erdey system) at temperature of 293÷773K, at dynamic regime by quickly heating for 5K/min. The aluminum oxide was used as a standard and a quantity of the sample was 0.100g, the temperature rise rate was 5 K/min. For

each sample DTA, TQA, and DTQ curves were obtained, the thermal or thermal-oxidative destruction of the sample was mainly estimated on the temperature corresponding to the mass loss of 5, 10 and 50% of the TGA and DTA curves.

III.   RESULTS AND DISCUSSION

The study of influence of temperature showed that (cooligomerization is carried out in the condition when hexene-1-indene ratio – 0.9:0.1 (mol.p.), a quantity of the catalyst – 0.5%) with its decrease from 313K to 228 K a yield of cooligomer is changed in the range of 95.4÷98.8%, i.e. as the ions are stable at low temperature, a decrease of temperature leads to increase of both yield and molecular weight of the prepared oligomer product, which is the characteristic peculiarity of the ionic polymerization.

In increase of a quantity of the indene from 0.05 mol.p to 0.10 mol.p (temperature 273 K and quantity of the catalyst 0.5%) in the monomer mixture the average molecular weight of the prepared cooligomer is increased from 830 to 1130. Further increase of a quantity of indene (0.20 mol.p.) leads to the decrease of the molecular weight to 950. As the indene is the monomer of the aromatic nature its small quantity facilitates the oligomerization showing positive influence on catalyst activity. In further increase of its quantity along with cooligomerization it can be taken place a dimerization and also alkylation of indene, which leads to the decrease of the average molecular weight of cooligomer (Table 1).

The results of cooligomerization are presented in Table 1.

TABLE 1
CONDITION OF COOLIGOMERIZATION OF HEXENE-1(M_1) WITH INDENE (M_2), YIELD AND SOME INDICES OF COOLIGOMERS

Condition of cooliogomerization			Yield, %	Characteristics of cooligomers	
Temperature, K	M_1:M_2. mol.p.	Quantity of the catalyst, %		Viscosity at 373K, mm^2/s	Average molecular weight
278	0.80:0.20	0.50	88.3	72.5	950
283	0.80:0.20	0.50	82.6	65.1	890
293	0.80:0.20	0.50	65.4	53.5	810
278	0.90:0.10	0.50	98.3	87.3	1180
283	0.90:0.10	0.50	96.8	55.2	1090
283	0.90:0.10	0.35	77.0	82.2	1000
283	0.90:0.10	0.50	97.3	85.6	880
313	0.90:0.10	0.50	95.4	56.5	820
278	0.90:0.10	0.17	58.2	63.7	890
278	0.95:0.05	0.50	84.1	62.6	870
313	0.95:0.05	0.17	52.0	55.7	830
313	0.95:0.05	0.50	75.3	51.8	790

For elucidation of distribution of the monomer links in oligomer chain the copolymerization constants of the investigated pairs of monomer have been determined by Fayneman-Ross method and the following values have been obtained:

for hexene-1 r_1=1.35±0,05

for indene r_2=0.23±0,01

The constant values r_1 and r_2 show that the end carbocations of both alkene and indene are more inclined to connect the molecules of hexene-1, i.e. during cooligomerization it is high a probability of the formation of macromolecules of real cooligomers enriched with hexene-1 links**.** Indeed, the prepared oligomers are enriched with hexene-1 links and there is a possibility of formation of hexene-1 homopolymer. However, it should be noted that the formation of homooligomer of hexene-1 in this system doesn't show a negative influence on results of the process, as it well dissolves in the petroleum oils. But the indene molecule is inclined to connection to the active center formed from hexene-1, i.e. a probability of being of

long-chain blocks, which can be created from indene homooligomer and residue of indene in cooligomer chain in the system is very small.

The composition and structures of the synthesized compounds have been studied by methods of the IR- and NMR-spectroscopy. The absorption bands in the IR-spectrum at 1576, 1588 and 1608 cm^{-1} characterize the aromatic C=C bonds (fig1). The absorption band at 728 cm^{-1} corresponds to 1,2-substituted benzene ring (indene link).

In the NMR-spectrum there are signals characterizing indene links – 2,06; 2,17 and 7,11 mln^{-1} signals correspond to chemical substituent.

During cooligomerization of hexene-1 with indene the following reactions can be taken place:

1) homooligomerization of hexene-1:

$$nCH_2{=}CH \longrightarrow \left[-CH_2-CH- \right]_n$$
$$\quad\quad\quad |\quad\quad\quad\quad\quad\quad |$$
$$\quad\quad C_4H_9\quad\quad\quad\quad\quad C_4H_9$$

2) cooligomerization of hexene-1 with indene

$$nCH_2{=}CH \;+\; m\;\text{(indene)} \xrightarrow{\text{catalyst}} \left(CH_2-CH \right)_n \left(\text{indene} \right)_m$$
$$\quad\quad |$$
$$\quad C_4H_9\quad\quad\quad\quad\quad\quad\quad\quad\quad\quad C_4H_9$$
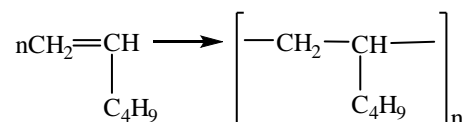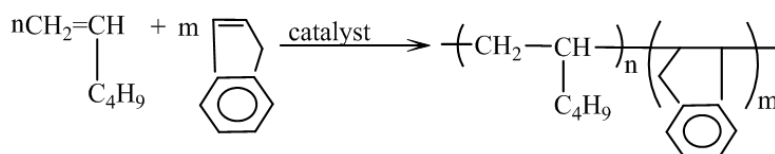
A location of links in the composition of macromolecules of the prepared cooligomer has mainly a statistic (accidental) character. However, as it is noted, an inclusion of the blocks prepared from hexene-1 molecules in composition of cooligomer macromolecules is possible, and a probability of inclusion of indene fragments in macromolecular chain as blocks is very little and it can be only realized when a ratio of indene:hexene is very high in the monomer mixture.
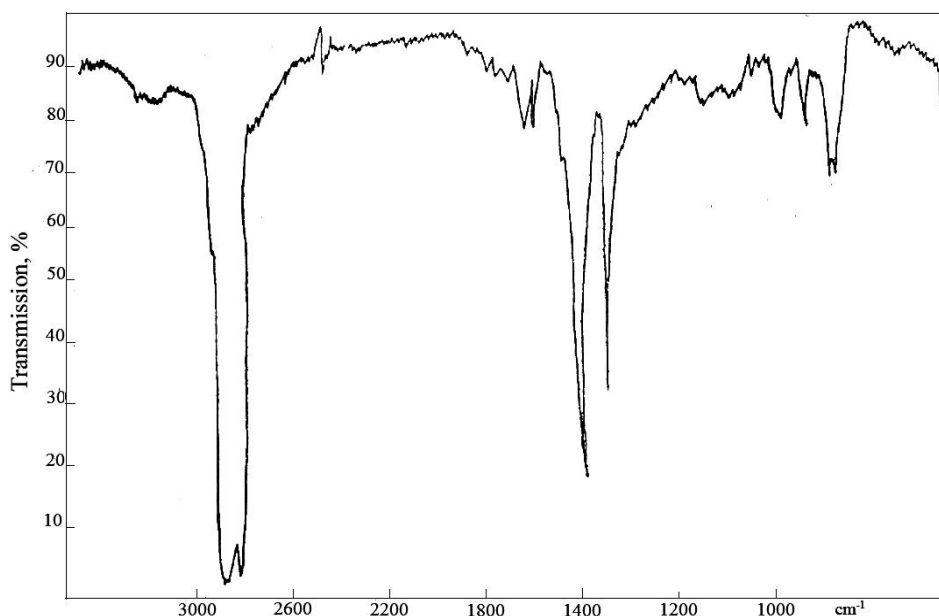
FIGURE 1 – IR-SPECTRUM OF COOLIGOMER OF HEXENE-1 WITH INDENE

The indene molecule combines the aromatic and cyclic fragments and its inclusion in macromolecular chain of hexene-1 increases the thermal stability of the prepared cooligomer. On the other hand, at cooligomerzation there are formed the interactions between aliphatic and aromatic carbons, which are stronger than interactions between aliphatic carbons and the investigation of such cooligomers as additive or component to the oils is of interest.

As the synthesized cooligomers have low molecular weight, they can present the more interesting information about stability to thermal effects individually than their destruction in the oils. Therefore, the thermal stability of the synthesized hexene-1-

indene cooligomers has been investigated by a derivatographic method and the obtained results are presented in Table 2. As is seen from Table, an increase of a quantity of the indene links in the composition of cooligomer leads to the increase of thermal stability, and an increase of the molecular weight (or viscosity) decreases thermal stability.

TABLE 2
RESULTS OF THERMOGRAVIMETRIC ANALYSIS OF HEXENE-1-INDENE BINARY COOLIGOMERS

Indices of cooligomer		Temeprature corresponding to mass loss		
Quantity of indene in cooligomer, mol.p.%	Molecular weight	$T_{5\%}$	$T_{10\%}$	$T_{50\%}$
0	700	463	493	573
0.05	660	480	503	590
0.10	600	493	513	603
0.20	540	490	518	613
0.30	500	495	543	620
0.10	700	483	513	593
0.10	810	475	505	580
0.10	1000	470	500	570

For ex., as a result of increase of a quantity of the indene links in the composition of cooligomer from 0 (oligohexene) to 0.30 mol.p the temperature corresponding to $T_{10\%}$ of mass loss of the sample rises from 493 K to 543 K. When the molecular weight value of cooligomer is increased from 610 to 1000 in the same composition (0.10 mol.p. of indene links), this temperature is decreased from 513 K to 500 K. A positive influence of increase a quantity of the indene links in the composition of cooligomer can be explained by aromatic nature of indene and creation of more stable $C_{aliph.}$- $C_{carboc.}$ bonds in the composition of cooligomer, i.e, the cooligomerization leads to the modification of macromolecule.

An increase of the average molecular weight of cooligomer has been connected with increase of length of macromolecules, as a result not subjecting macromolecules to destruction their intensity of motion is decreased depending on temperature. As a result of destruction the macromolecule is divided into more small-measured analogs and its motion is facilitated. Therefore, the oligomers with low molecular weight are more stable to destructive effects.

Thermal destruction of hexene-1-indene binary cooligomers has been carried out in the oil solutions. This is carried out according to known method; 5% solution of the polymer samples in turbine "L" oil is heated for 12 h at temperature 473 K and after certain time intervals a decrease of value of the initial kinematic viscosity is observed and certain information about destruction is obtained. The prepared results are presented in Fig.2 and 3.

It is seen from Fig.2 that an increase of a quantity of the indene links from 0.05 mol.p. to 0.20 mol.p in the composition of cooligomer increases a stability of concentrated oil to thermal influence, in this time the initial viscosity of the oil is decreased from 3% to 1,2%, and as has been already noted, it is connected with stabilizing effect of the indene links. An increase of the average molecular weight value of hexene-1-indene binary cooligomers from 600 to 1000 leads to the decrease of thermal stability, in this time a viscosity value of the concentrated oil decreases from 2,3% to 3,1% (Fig. 3).

The mechanical destruction solutions of the synthesized cooligomers of hexene-1-indene in the oil have been also studied. For this purpose there have been investigated the solutions of cooligomer samples in I-12 A oil with various composition and molecular weight values by means of device UZDN-1. The obtained results are very close to the results of thermal destruction, i.e. thermomechanical stability is also determined by average molecular weight value and composition of copolymer. However, it should be noted that the mechanical destruction leads to breaking of C-C bond composing the main chain of the viscous additives. Thermal destruction can be referred to all chemical bonds and if destruction occurs in air medium, firstly thermal oxidation of molecule takes place, i.e. the process is more correct to characterize as thermooxidation destruction.
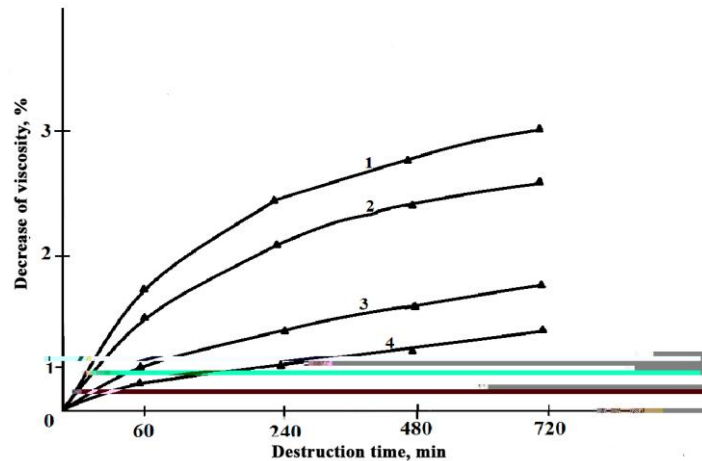
FIGURE 2 – DEPENDENCE OF THERMAL STABILITY OF HEXENE-1-INDENE COOLIGOMERS ON QUANTITY OF INDENE LINKS. QUANTITY OF INDENE LINKS, MOL.P.: 0.05 (1), 0.10 (2), 0.15 (3) AND 0.20 (4).

The properties of these cooligomers have been compared with results of destruction of viscous additives used for improvement of viscosity-temperature properties of the oils. So, a decrease viscosity during thermal destruction of polyisobutylene of mark KP-10 being industrial additive is 12%, for oligohexene – 9,4%. Thus, the binary cooligomers of hexene-1-indene possess excellent indices from the point of view thermomechanical destruction stability.
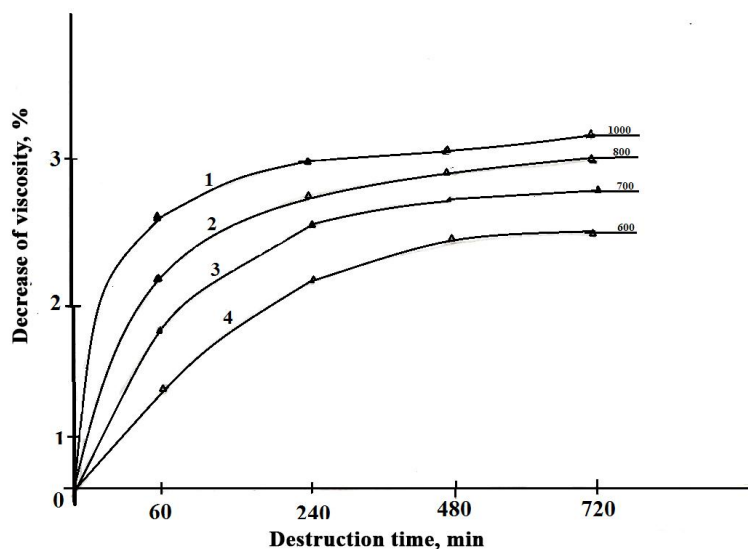
FIGURE 3 – DEPENDENCE OF THERMAL STABILITY OF HEXENE-1-INDENE COOLIGOMERS ON QUANTITY OF AVERAGE MOLECULAR WEIGHT VALUE. AVERAGE MOLECULAR WEIGHT OF COOLIGOMER: 1000 (1), 800 (2), 700 (3) və 600 (4).

The binary cooligomers of hexene-1-indene have been investigated as synthetic component in the composition of M-6 oil and the results are obtained in Table 3. As synthetic component it was used the cooligomer with average molecular weight – 1180, and a quantity of indene links – 0.10 mol.p.

TABLE 3
INFLUENCE OF HEXENE-1-INDENE BINARY COOLIGOMERS ON VISCOSITY-TEMPERATURE PROPERTIES OF M-6 OIL.

Quantity of cooligomer in the oil	Kinematic viscosity, mm^2/s		Viscosity index	Corrosion, g/m^2
	373 K-də	313 K-də		
0	5.8	39.40	78	180
5	6.3	42.10	83	150
10	6.5	45.00	83	100
20	7.6	50.30	94	50
30	8.4	59.80	106	10
40	8.8	64.20	108	5
50	9.1	65.40	110	4

As is seen from Table that an increase of concentration of synthetic component in M-6 oil leads to improvement viscosity-temperature properties of the prepared mixture, and for preparation of base oil with kinematic viscosity $8\pm0,5$ mm^2/c at 373 K it is enough to include 20-30% synthetic component in composition of M-6 oil. In this time a viscosity index value of M-6 oil rises from 78 to $94 \div 106$ (norm – no less 93).

When an increase of viscosity index of M-6 oil by synthetic component in 20-30% concentration is higher, a further increase of concentration has little effect on value of this parameter. At the same time, the investigated cooligomer shows anticorrosion property in the composition of M-6 oil. So, the oxidation products create corrosion. Due to availability of indene links in the composition of the investigated compound it is more stable to oxidation. It has been elucidated that the use of 30% of oligomer in the composition of M-6 oil leads to the decrease of a quantity of precipitate forming as a result of oxidation from $3\div4$% to $1,2\div1,3$%. Thus, by use of synthetic component in the composition of petroleum oil it is reached an improvement of its viscosity-temperature property and stability to oxidation and anticorrosion.

IV. CONCLUSIONS

It has been carried out the copolymerization reactions of hexene-1 and indene with participation of $BF_3 \cdot O(C_2H_5)_2$ as the catalyst, and the yield, the composition, the structure, the copolymerization constant and the average molecular weight values depending on cooligomerization condition have been determined. The cooligomerization constant values (for hexene-1 – $r_1 = 1.35\pm0,05$, for indene – $r_2 = 0.23\pm0,01$) have been determined at low depth of conversion of comonomers. It has been shown that a location of links in the prepared cooligomer has a statistic character, but the blocks prepared from molecules of hexene-1 may be included.

Thermal stability of the synthesized cooligomers of hexene-1-indene has been investigated both individually and in oil solution and it has been elucidated that an increase of quantity of indene links in cooligomer composition leads to increase of thermal stability, and an increase of molecular weight decreases a thermal stability.

An inclusion of the synthesized cooligomers in a quantity of 20-30% in composition of M-6 oil as synthetic component increases a viscosity index value from 78 to $94\div106$ and gives it anticorrosion property.

REFERENCES

[1] A. M. Kuliyev, Chemistry and technology of additives for oils and fuels. L.: Khimiya, 1985, 312p.

[2] Z. Yanovich, A. Yukich, E. Vidovich, "Tertiary copolymers of maleic anyhdride and long-chain alkylmethacrylates as viscosity additives to mineral oils," Chemistry and technology of fuels and oils, pp. 33-37, April 2009.

[3] A. I. Akhmedov, B. M. Farzaliyev, P. M. Aliguliyev, Polymer additives and oils. Baku: Elm, 2000, 175p.

[4] A. I. Akhmedov, "Viscosity additives to oil and synthetic oils on the basis of alkylmethacrylates," Az.oil industry, pp.36-41, February 2004.

[5] G. R. Gasanova, A. I. Akhmedov, V. S. Gasanov, "Synthesis of multifunctional additives polyalkylmethacrylate type," Chemistry and oil chemistry, pp. 31-344, February 2005.

[6] A. I. Akhmedov, Z. A. Lachinova, D. Sh. Hamidova, "Copolymers of alkylmethacrylates with α-olefins as viscous additives," Az. Chem. J., pp.117-119, April 2006.

[7] T. F. Ganiyeva, R. Z. Fakhrutdinova, "Additives to petroleum oils," Oil-refining and Petrochemistry, pp.38-39, August 2012.

Linear Quadratic Regulator Procedure and Symmetric Root Locus Relationship Analysis

Mariela Alexandrova[1], Nasko Atanasov[2], Ivan Grigorov[3], Ivelina Zlateva[4]

Department of Automation, Technical University of Varna, Bulgaria

Corresponding Authors Email: m_alexandrova@tu-varna.bg

Abstract— *The present paper is focused on linear quadratic regulator (LQR) synthesis. It is evident that the solution of the problem leads to finding a solution of symmetric root locus (SRL) problem. It is proven and analytical evidences is also presented that by using SRL synthesis method and further application of LQR method guarantees stability, minimum phase and gain margins of the closed loop system. The presented mathematical relationships are further proven with experimental investigation in MATLAB programming environment.*

Keywords— *linear quadratic regulator, minimum phase system, Riccati equation, stability, state space, symmetric root locus.*

I. INTRODUCTION

The scope of the present paper is LQR synthesis in the state space. According to the state feedback control chosen, the synthesis procedure is related to determination of the state feedback matrix elements in a manner that a compromise between achieving the desired settling time and the control effort needed. In the presence of immeasurable states, observers are typically used for state vector estimation. The prerequisites needed for the synthesis are the system to be completely controllable and observable although advanced state variable design techniques can handle situations wherein the system is only stabilizable and detectable. In the present paper it is assumed that the system is completely controllable and observable and all the state variables are measurable.

The procedure for LQR synthesis requires the feedback matrix to be chosen in order to satisfy the condition for minimum value of the cost function presented as integral performance estimation. The closed loop is considered optimal as it guarantees the minimum possible value of the cost function. The synthesis procedure allows the operator to choose the weights so that the compromise between the state cost and the control cost is acceptable. The major disadvantage of this technique is that the exact poles position and the control effort value are initially unknown.

The present paper aims to investigate the relationship between the linear quadratic regulator procedure and the symmetric root locus of the closed loop system.

For the provision of this analysis few main aspects should be investigated in details and further proven:

1. Find analytic solution of the LQR synthesis based on the Pontriagin's minimum principle.

2. Show that LQR synthesis can be solved by SRL.

3. Use SLR procedure to prove that when LQR synthesis is applied the closed loop system will always be stable and minimum phase.

II. LQR SYNTHESIS BASED ON THE PONTRIAGIN'S MINIMUM PRINCIPLE

For a given closed loop system, denoted in Fig.1, the state space open loop system model is:

$$\dot{\mathbf{x}} = \mathbf{A}\mathbf{x} + \mathbf{B}\mathbf{u}$$
$$\mathbf{y} = \mathbf{C}\mathbf{x}$$

(1)
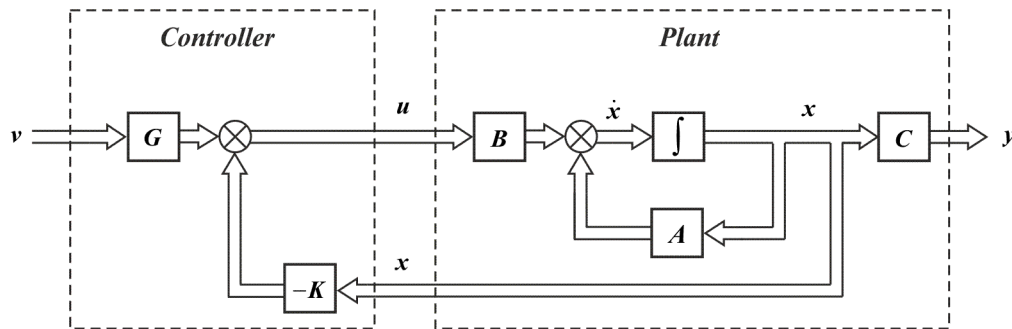
FIGURE 1. CLOSED LOOP BLOCK DIAGRAM

The feedback control law in the presence of a reference signal is:

$$\mathbf{u}(t) = \mathbf{-Kx}(t) + \mathbf{Gv}(t)$$

(2)

where $\mathbf{v}(t)$ is the reference value and the matrix $\mathbf{G}$ is given an auxiliary function to recalculate the reference value for steady state error free system [1]. Assuming the following transformation $\mathbf{v}(t) = 0 \Leftrightarrow t > 0$ the control design problem is known as regulator problem [2]. It has the following aspects: determination of $\mathbf{K}$ so that all initial conditions are derived to zero using a specified approach determined by the desired system performance which corresponds to the closed loop pole values.

The optimal control design (Fig.1) is a constrained optimization problem with cost function $J\left(\mathbf{x}, \mathbf{u}, t, t_f\right)$ which can be expressed as:

$$J = \frac{1}{2}\mathbf{x}^T\left(t_f\right)\mathbf{Sx}\left(t_f\right) + \int_0^{t_f}\left(\frac{1}{2}\mathbf{x}^T\mathbf{Qx} + \frac{1}{2}\mathbf{u}^T\mathbf{Ru}\right)dt$$

(3)

and the constrain given by equation (1) [4,6,7]. The matrices in (3) must satisfy $\mathbf{S} \geq 0$, $\mathbf{Q} \geq 0$ and $\mathbf{R} > 0$. The implementation of co-state vector λ [5] consisted of the Lagrange multipliers transforms (3) into unconstrained optimization problem, described by:

$$J = \frac{1}{2}\mathbf{x}^T\left(t_f\right)\mathbf{Sx}\left(t_f\right) + \int_0^{t_f}\left[\frac{1}{2}\mathbf{x}^T\mathbf{Qx} + \frac{1}{2}\mathbf{u}^T\mathbf{Ru} + \lambda^T\left(\mathbf{Ax} + \mathbf{Bu} - \dot{\mathbf{x}}\right)\right]dt$$

(4)

In order to obtain the minimum value of (4) all the derivatives of J with respect to $\mathbf{x}$, $\mathbf{u}$ and $\mathbf{x}\left(t_f\right)$ must be equal to zero. According to the last operation the closed loop dynamics can be determined by the following simultaneous equations for a given mixed boundary conditions $\mathbf{x}(0) = \mathbf{x}_0$ and $\lambda\left(t_f\right) = \mathbf{Sx}\left(t_f\right)$ [4]:

$$\begin{vmatrix} \dot{\mathbf{x}} = \mathbf{Ax} + \mathbf{Bu} \\ \dot{\lambda} = -\mathbf{Qx} - \mathbf{A}^T\lambda \\ \mathbf{u} = -\mathbf{R}^{-1}\mathbf{B}^T\lambda \end{vmatrix}$$

(5)

This is the so called two point boundary value problem (TPBVP) [8]. The system (5) can be presented as a homogenous vector-matrix differential equation:

$$\begin{bmatrix} \dot{\mathbf{x}} \\ \dot{\lambda} \end{bmatrix} = \underbrace{\begin{bmatrix} \mathbf{A} & -\mathbf{BR}^{-1}\mathbf{B}^T \\ -\mathbf{Q} & -\mathbf{A}^T \end{bmatrix}}_{\mathbf{H}} \begin{bmatrix} \mathbf{x} \\ \lambda \end{bmatrix}$$

(6)

Where $\mathbf{H}$ is the so called Hamiltonian matrix [5].

The substitution:

$$\lambda = \mathbf{Px}$$

(7)

and the equation system (6) leads to the following expression:

$$\dot{\boldsymbol{\lambda}} = \dot{\mathbf{P}}\mathbf{x} + \mathbf{P}\dot{\mathbf{x}} = \dot{\mathbf{P}}\mathbf{x} + \mathbf{P}\mathbf{A}\mathbf{x} - \mathbf{P}\mathbf{B}\mathbf{R}^{-1}\mathbf{B}^{T}\mathbf{P}\mathbf{x} = -\mathbf{Q}\mathbf{x} - \mathbf{A}^{T}\mathbf{P}\mathbf{x}$$

(8)

After the reduction of the common multiplier $\mathbf{x}$ equation (8) can be written in the form:

$$\dot{\mathbf{P}} = -\mathbf{A}^{T}\mathbf{P} - \mathbf{P}\mathbf{A} - \mathbf{Q} + \mathbf{P}\mathbf{B}\mathbf{R}^{-1}\mathbf{B}^{T}\mathbf{P}$$

(9)

known as differential vector-matrix Riccati equation.

This equation can be solved backward in time under the condition:

$$\mathbf{P}\left(t_{f}\right) = \mathbf{S}$$

(10)

It defines the optimal control law:

$$\mathbf{u}\left(t\right) = -\mathbf{R}^{-1}\mathbf{B}^{T}\mathbf{P}\left(t\right)\mathbf{x}\left(t\right) = -\mathbf{K}\left(t\right)\mathbf{x}\left(t\right)$$

(11)

The steady state value of equation (11) is the solution of the algebraic Riccati equation:

$$\mathbf{A}^{T}\mathbf{P} + \mathbf{P}\mathbf{A} + \mathbf{Q} - \mathbf{P}\mathbf{B}\mathbf{R}^{-1}\mathbf{B}^{T}\mathbf{P} = 0$$

(12)

and determines the control law in the form:

$$\mathbf{u}\left(t\right) = -\mathbf{R}^{-1}\mathbf{B}^{T}\mathbf{P}\mathbf{x}\left(t\right) = -\mathbf{K}\mathbf{x}\left(t\right)$$

(13)

III.   LQR SYNTHESIS AND SRL

The closed loop system dynamics is described by the equation (6). The eigenvalues of matrix $\mathbf{H}$ are the closed loop poles. They are doubled in number than the number of the eigenvalues of matrix $\mathbf{A}$ and can be further determined as a solution of the following equation:

$$\det\left(s\mathbf{I} - \mathbf{H}\right) = 0$$

(14)

The implication of the substitution $\mathbf{Q} = \mathbf{C}^{T}\mathbf{C}$ and introduction of the following notations are further used for the purpose of this analysis:

$$\mathbf{W}_{P}\left(s\right) = \mathbf{C}\left(sI - \mathbf{A}\right)^{-1}\mathbf{B}$$

(15)

$$\mathbf{W}_{P}^{T}\left(-s\right) = \mathbf{B}^{T}\left(-s\mathbf{I} - \mathbf{A}^{T}\right)^{-1}\mathbf{C}^{T}$$

(16)

$$D\left(s\right) = \det\left(s\mathbf{I} - \mathbf{A}\right)$$

(17)

According to some well known matrix relations and transformations described in [7] the equation given below can be obtained:

$$\det\left(s\mathbf{I} - \mathbf{H}\right) = \left(-1\right)^{n}D\left(s\right)D\left(-s\right)\det\left[\mathbf{I} + \mathbf{R}^{-1}\mathbf{W}_{P}^{T}\left(-s\right)\mathbf{W}_{P}\left(s\right)\right]$$

(18)

where n is the state vector dimension.

For SISO system equation (18) can be presented as:

$$\det\left(s\mathbf{I} - \mathbf{H}\right) = \left(-1\right)^{n}D\left(s\right)D\left(-s\right)\left[1 + R^{-1}W_{P}\left(s\right)W_{P}\left(-s\right)\right] = 0$$

(19)

The open loop system transfer function could be then described as a polynomial ratio:

$$W_{P}\left(s\right) = \mathbf{C}\left(s\mathbf{I} - \mathbf{A}\right)^{-1}\mathbf{B} = \frac{N\left(s\right)}{D\left(s\right)}$$

(20)

Considering (20) equation (19) is transformed into:

$$\det\left(s\mathbf{I}-\mathbf{H}\right)=\left(-1\right)^{n}\left[D(s)D(-s)+R^{-1}N(s)N(-s)\right]=0$$

(21)

Consequently the closed loop poles determination can be solved as standard root locus problem with variation of R^{-1} into the range $(0,\infty)$. The specifics here are that the locus is symmetric in accordance with the abscissa as well as with the ordinate and has $2n$ loci. Half of them are positioned in the left half of the complex plane and are related to the n stable closed loop poles corresponding to the state vector $\mathbf{x}$. The other half of loci are in the right half plane and are related to the n unstable closed loop poles which correspond to the co-state vector λ. The unstable poles can be transformed into stable if the differential Riccati equation is solved backward in time[7,8].

IV.   STABLE AND MINIMUM-PHASE CLOSED LOOP SYSTEM

As it was described above the weight matrices must be $\mathbf{Q}\geq0$ and $\mathbf{R}>0$. It is also known that only the state cost weight can be equal to zero. Thus according to the root locus it is more convenient weight factor ρ to be implemented under the assumption of $R=1$ [2]. The cost function can be then described by the following integral relation:

$$J=\frac{1}{2}\int_{0}^{\infty}\rho\mathbf{x}^{T}\mathbf{Q}\mathbf{x}+\mathbf{u}^{T}\mathbf{u}dt \quad\Leftrightarrow\quad =\frac{1}{2}\int_{0}^{\infty}\rho\mathbf{y}^{T}\mathbf{y}+\mathbf{u}^{T}\mathbf{u}dt$$

(22)

The SRL is determined by the equation [6]:

$$D(s)D(-s)+\rho N(s)N(-s)=0$$

(23)

and is expresses as a function of the weight factor ρ which varies into the range $[0,\infty)$.

For $\rho=0$ minimum settling time is not a requirement. The stable closed loop poles coincide with the system roots in the left half plane and/or with the reflection of the unstable open loop poles in accordance with ordinate. Thus the closed loop system stability is guaranteed with lower values of the control signal.

For higher values of ρ the poles are shifted following the root loci and respectively the control effort increases too.

For $\rho\to\infty$, m closed loop poles approaching open loop zeros in the left half plane and/or their reflection in the right half plane. In this so described case the impact of those poles and zeros is negligible. The rest $(n-m)$ poles approaching infinity following specific trajectories and form the so called Butterworth pattern. The settling time is shortest possible however the control effort rises dramatically which in some cases is unacceptable [2,8].

The solution of the following equation is investigated in order to confirm those statements:

$$\Delta(s)=D(s)D(-s)+\rho N(s)N(-s)=0$$

(24)

with variations of ρ within the range $[0,\infty)$. In accordance with the below polynomial form:

$$D(s)=s^{n}+d_{1}s^{n-1}+\cdots+d_{n}$$

(25)

and

$$N(s)=n_{0}s^{m}+n_{1}s^{m-1}+\cdots+n_{m}=n_{0}N_{1}(s)$$

(26)

is obvious that:

$$N(s)N(-s)=n_{0}^{2}N_{1}(s)N_{1}(-s)$$

(27)

For $\rho=0$:

$$\Delta(s)=D(s)D(-s)=0$$

(28)

Thus the roots of $\Delta(s)$, which are closed loop poles, coincide with the open loop poles and their ordinate symmetric reflections.

For $\rho \to \infty$ the first addend in equation (24) $D(s)D(-s)$ is neglected:

$$\Delta(s) = \rho N(s) N(-s) = \rho n_0^2 N_1(s) N_1(-s) = 0 \tag{29}$$

The polynomial $\Delta(s)$ is sum of the two addends $D(s)D(-s)$ and $\rho n_0^2 N_1(s) N_1(-s)$. Since the zeros of $N_1(s) N_1(-s)$ result in zero sum and zero second addend as well then they respectively zero the first addend too. Consequently it can be presented as:

$$D(s)D(-s) = N_1(s) N_1(-s) D_1(s) D_1(-s) \tag{30}$$

and $\Delta(s)$ is further transformed into the equation:

$$\Delta(s) = N_1(s) N_1(-s) D_1(s) D_1(-s) + \rho n_0^2 N_1(s) N_1(-s) =$$
$$= \underbrace{N_1(s) N_1(-s)}_{\Delta_1(s)} \underbrace{\left[D_1(s) D_1(-s) + \rho n_0^2 \right]}_{\Delta_2(s)} = 0 \tag{31}$$

The first multiplier $\Delta_1(s)$ roots are the zeros of the open loop system and their symmetric ordinate reflections. The second multiplier:

$$\Delta_2(s) = D_1(s) D_1(-s) + \rho n_0^2 \tag{32}$$

can be transformed as follows:

$$\Delta_2(s) = (-1)^{n-m} s^{2(n-m)} + \tilde{d}_1 s^{2(n-m)-1} + \tilde{d}_2 s^{2(n-m)-2} + \cdots + \tilde{d}_{2(n-m)} + \rho n_0^2 \tag{33}$$

For $\rho \to \infty$ the roots of $\Delta_2(s)$ converge to the roots of equation:

$$(-1)^{n-m} s^{2(n-m)} + \rho n_0^2 = 0 \tag{34}$$

Respectively the roots of $\Delta_2(s)$ converge to the roots of the binomial equation:

$$s^{2(n-m)} + \frac{1}{(-1)^{n-m}} \rho n_0^2 = 0 \tag{35}$$

The roots of equation (35) appear to be the apexes of regular $(2(n-m))$- dimensional polygon and are positioned on the circle centered in the origin with radius $\left(\rho n_0^2 \right)^{1/2(n-m)}$. For higher values of ρ they are shifted from the origin following the trajectories by the circle radiuses forming equal angles $\left(\dfrac{\pi}{n-m} \right)$. The resulted plot with $(2(n-m))$ rays is associated with the so called Butterworth pattern [1,2,3].

V.   NUMERICAL EXAMPLE

The open loop system investigated is unstable and non minimum-phase described by the below presented transfer function [4]:

$$W(s) = \frac{(s-2)(s-4)}{s^2 (s-1)(s-3)(s^2 + 0.8s + 4.16)}$$

The problem formulated is LQR synthesis aiming to minimize the value of the cost function J (22).

Specific algorithm has been developed in MATLAB for the purpose of this analysis. The resulted SRL is shown in Fig.2.

It is evident that:

➢ for $\rho = 0$ two of the SRL loci begin at the two stable complex roots of the open loop system $s_{1,2} = -4 \pm 2i$. Another pair loci begin at zero pair roots $s_{3,4} = 0$ and third pair begin at the ordinate symmetric unstable roots $s_5 = 1$ and $s_6 = 3$. The analysis shows that in this case in particular the closed loop system is at least considered stable;

➢ with the increase of the value of ρ the last pair loci described above are approaching the ordinate symmetric positive zeros $s = 2$ and $s = 4$; when ρ approaches infinity that pair ends at those zeros which leads to compensation of the influence of the zeros $s = -2$ and $s = -4$ with two of the poles. The rest four loci are shifting from the origin following the radiuses of central circle, forming equal angles of $\pi/4$. The result is retention of the closed loop system stability, short settling time, and increase in the natural system frequency; however the system requires higher control signal values.
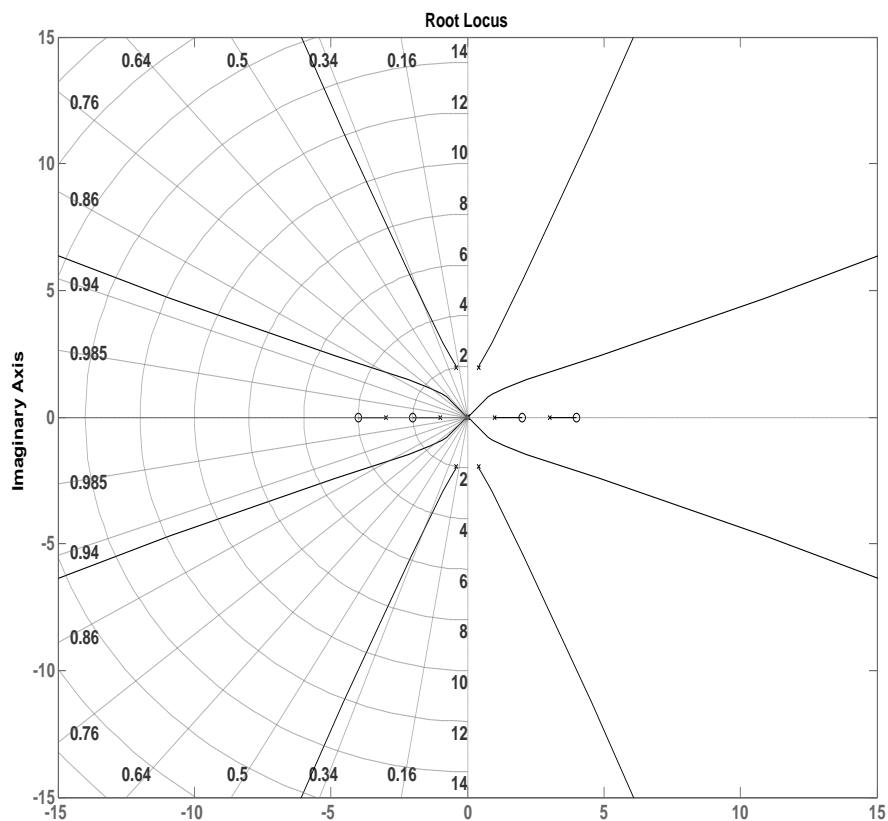
FIGURE 2. BUTTERWORTH MODEL FOR SRL

VI. CONCLUSION

The paper presents analytical evidence that LQR synthesis can be considered as SRL problem.

In the presence of evidence for completely controllable and observable (stabilizable and detectable) open loop system the state feedback synthesis is invariant in accordance with open loop system stability.

LQR can be also taken into consideration as a method for state feedback matrix generation with guarantees for stability, minimum phase and stability margins of the closed loop system.

This type of analysis, using graphic interpretation (*ex. Fig.2*) allows direct identification of the damping ratio and corresponding natural frequencies ω_n and respectively further calculation of the weight coefficient $\rho = \omega_n^{2(n-m)}$ for any point positioned on the loci.

The results delivered give further option for investigation of possible relationship and application of the pole placement synthesis and LQR synthesis based on SRL in the frequency domain.

REFERENCES

[1] Atanasov, N. and A.Ichtev, K.Ishtev (2012). Control Theory Part 1, Technical University of Varna, Bulgaria.

[2] Dorf, R. and R.Bishop (2008). Modern Control Systems, Eleventh edition, Pearson Prentice Hall.

[3] Franklin, G.F. and J.D.Powell, A.Emami-Naeini (2006). Feedback Control Of Dynamic Systems, Fifth Edition, Pearson Prentice Hall.

[4] How, J. (2001). Feedback Control Systems, http://hdl.handle.net/1721.1/45531.

[5] Kurtal, P. (2013). Dynamic Optimization in Continuous Time, Lecture notes (Econ210), https://web.stanford.edu/~pkurlat/teaching/14%20-%20Continuous%20Time.pdf.

[6] Perry, Y.Li (2017). Advanced Control Systems Design, ME8281, Lecture notes, http://www.me.umn.edu/courses/me8281/notes/LQ_Abiram.pdf, 156-179.

[7] M Plett, G. (2017). Multivariable Control Systems II, ECE5530, Lecture notes, http://mocha-java.uccs.edu/ECE5530/index.html, 3-1 – 3-37.

[8] Shahian, B. and M.Hassul (1993). Control System Design Using Matlab, Prentice-Hall Inc., New Jersey.

Validation and Integrity Mechanism for Web Application Security

Saher Manaseer[1], Ahmad K. Hwaitat[2]

[1,2]Department of Computer Science, The University of Jordan, Amman-Jordan

Abstract—Recently the world of web applications has witnessed a huge wave of attacks that caused a lot of web applications to get defaced and for a lot of businesses to lose financially and to lose the integrity between those companies and their users .since web hacking became common knowledge on the Internet and most of the defacements that happens on daily basis are going under a random way, the security specialists are trying to get new solutions that will help reduce the possibility of causing much damage to web applications even after the process of infiltration.

In this research an enhanced web application solution was proposed, which is a validation and integrity component that can be easily installed on any web application firewall (WAF), in order to help in solving the problem mentioned and raise the level of trust between user's and web application hosts/owners also restore the lost data caused by hacking attempts in simple and systematic way.

Keywords—Attack Prevention, Application Firewall, Cyber security, Firewall component, Internet Attacks.

I.   INTRODUCTION

Recently, the growth of web applications usage started to rise in a large way, which made the possibility of more web application vulnerabilities to appear and more hacking attempts to happen on daily basis [1]. The development of web applications witnessed a huge revolution along with the revolution of the Internet. Web applications are becoming very essential in the daily activities of persons and companies [1][2]. Some of these activities contain confidential information about the user such as credit card numbers, passwords, and money authorization transactions information.

The security of the user's information is a major concern for all companies' owners and administrators due to the successful attacks against web applications across the history. Many attackers   may be able to compromise some web applications and access private data across the global net by exploiting several known and un-known web application vulnerabilities [3][4]. Such cyber-attacks can cause financial loss for many parties including private companies and any other type of infrastructure. They are also a main reason for users to lose trust and integrity in many private and governmental institutions. Therefore, there is a major need for developing researches and find methods for preventing and detecting any possible attack against such web based infrastructure, securing databases and help making the data more private for the users. Furthermore, there is a need to take pre-steps and create a method to restore lost data after the occurrence of the attack as fast as possible and help raise the integrity level of the content inside the web application.

II.   RELATED WORK

Double Guard is an application used for checking the intrusions in multi-tier application. This application is used for back-end and front-end and its independent, it is also operated in dynamic and static servers in the web, these servers provide better protection for the application and information [5].

An approach based on learning was presented by [6], for securing web services against SQL and XPath Injection attacks. Valid requests patterns were learnt by the approach, and that is called the learning phase, then it was able of detecting and aborting requests which might harm the server, which is called the protecting phase. Some heuristics might be used to deal with suspicious cases when there isn't a possibility to have a finished learning phase. The technique was executed to keep TPC-App services safe, and for opening source service effect.

In [7], a mechanism was developed for the detection of SQL injection, by employing a Reverse proxy and MD5 algorithm to watch SQL injection in input. Using rules of grammar expressions for checking SQL injection in URL's. No changes are done in the application's source code by their method. Investigating and decreasing the attack is automatically done. The increasing in the number of proxy servers makes web applications able to handle any number of requests with no delay of time, and makes it able to protect the application from SQL injection attack.

A novel and an effective solution for the problem of XSS was suggested by [8], its purpose was to detect all SQLIA kinds. Their technique also checked the assigned value for a single quote, double dash and space given by the user through input sections. A space, single quotes or double dashes are ought to be used by the attacker in his input, when he is scripting an SQL injection.

The method of [9], is for combined static analysis and runtime validation. Legitimate queries are found in static analysis, it can be operated by the application, and it can also reform them into patterns of structure query. The query patterns resulted from it are kept in a separate respective tables, and that is for the reason of decreasing the runtime validation overhead the runtime query in the runtime validation is made into patterns and a comparison is made between them and the predetermined structure query patterns. The performance of the suggested technique has been evaluated by examining on weak web applications. The presented method can be performed on both web applications and applications which are linked to database

In [10], researchers have focused on one issue, namely the integrity of web content. It has been shown that given the limitations of SSL, a loss of web content integrity is possible because of the statelessness of HTTP. In an attempt to overcome this problem, a systematic web security framework was formulated to provide continued reliable and correct services to external users, even though a web data manipulation problem may have occurred. It was suggested that such a framework will offer an increased level of user confidence, since the framework provide a greater protection against web server subversion.

Novel approach for detecting SQL attacks which are based on information theory, was proposed by [11], the entropy of all queries, which exists in a program accessed before deploying a program, is computed during time of executing the program. This approach depends on the thought that dynamic queries with attack inputs result in a level of entropy that is decreased or increased. Three open source PHP applications which contain SQLI weaknesses, proved by report, validated the proposed framework. A prototype tool is implemented by them in Java for facilitating training and detection phase of the proposed technique. The result of the evaluation indicated that the technique checks all known SQLI weaknesses and might be an integral one to verify unknown weaknesses.

III. MATERIALS AND METHODS

The following figure (Fig.1) shows the main components of restoring the website.
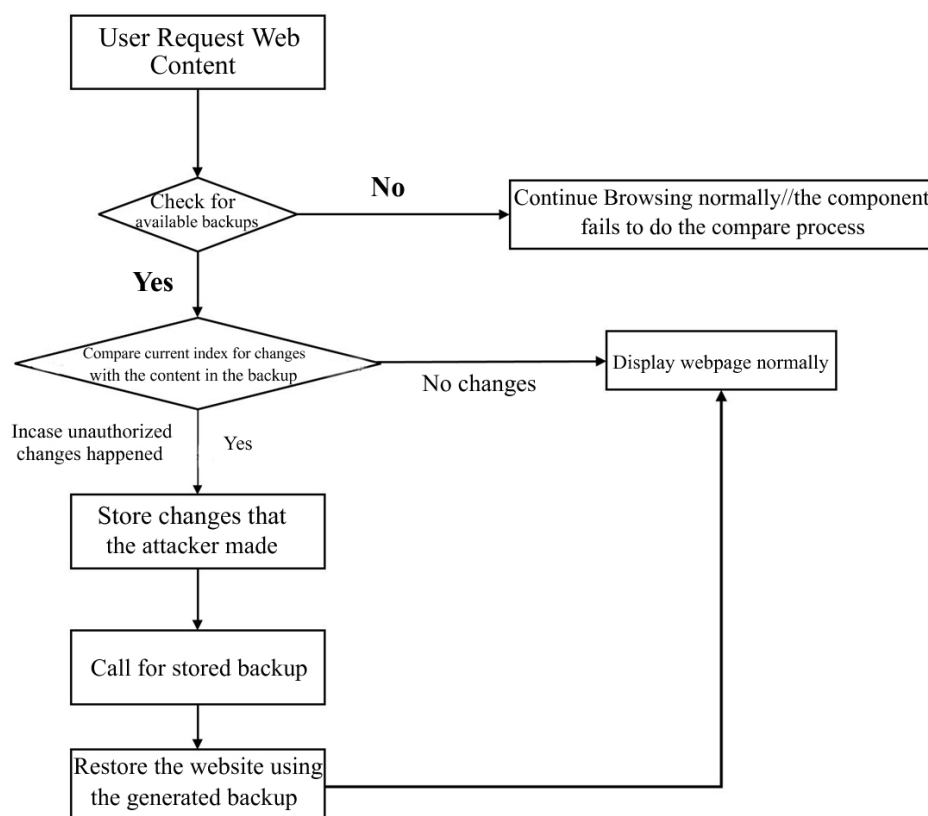

FIGURE 1: WEBSITE RESTORE COMPONENT

The proposed enhancement is triggered whenever a request is sent to the website, the enhanced component will check for available backups then start the process of comparison using a unique given hash for both the backup file and the website content [12], in-order to validate the current content and take actions in-case of any change on the website that wasn't permitted by the administrators [13]. The auto restore component will make sure to store all the changes that the attacker may have made after the infiltration also will make sure that the user gets the original website content and never endures the content that the attacker may have published on the server. this enhancement aims to protect the web application information and it also increases the level of integrity between the user and the web application owners and institutions, it also save the website from any misuse by the attacker if he/she aims to publish illegal, harmful or not suitable content through the hacked website, the proposed enhancement is a component that assures the integrity and safety of the content and only display the content that was only meant to be shown by the website's administrators.

When a change in the website's content is discovered by the component the process of validation will start checking for previous backups of the website on the server in order to restore the website content automatically, the enhanced component will use the last updated backup that has been generated previously to be restored.

A mechanism for generating auto backup has been added to the proposed component, which will be enabled by the administrator to create a backup for all the contents of the website at any time.
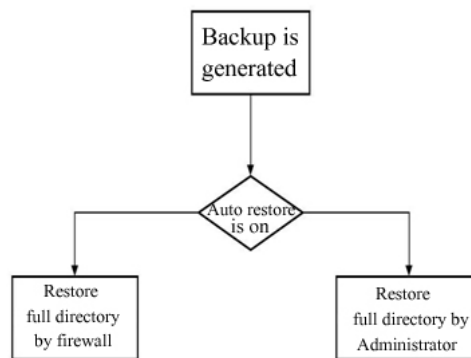
FIGURE 2: BACK UP IS GENERATED

3.1   Website restore component options

Two options for the proposed component has been added, which are the manual and automatic website restore. The manual restore option is left for the admin to decide to restore the changes or take whatever suitable actions in the case of infiltration. On the other hand the auto restore option will directly take automatic actions and fully restore the original website contents using the already stored backup files as explained in the fig. 2 above.

3.2   Store the changes that the attacker made

The added component has a feature to record and store all the changes that the attacker made to the web content, and make a report of these changes, this is done by comparing the code of the original web content with the content that the attacker have changed.

IV.   RESULTS OF TESTING THE WEBSITE RESTORE COMPONENT

4.1   Testing restore component

To test the restore component we have created a sample website for testing purposes consist of few web pages and an index page that is shown in fig.3 in one domain:

FIGURE 3: ORIGINAL SAMPLE INDEX PAGE OF THE DEMO WEBSITE

The option is set to auto restore in-order to restore the full directory in-case of change automatically see fig. 4,then a new index page is uploaded using the server hosting panel, as soon as the new index page is replaced the auto restore component gets triggered and restore the original   full directory from the backup file that we have generated before see fig.5.
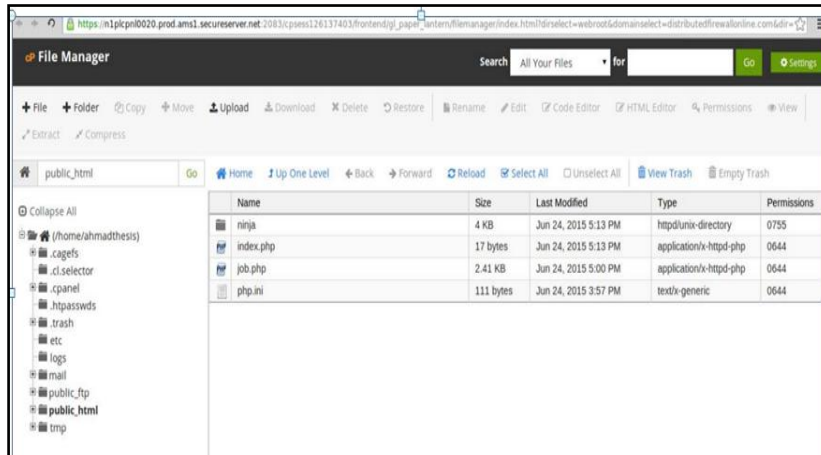
FIGURE 4: THE PROCESS OF CHANGING THE CONTENT FROM THE SERVER PANEL

FIGURE 5: THE RESTORED WEB PAGE

4.2   Testing the feature of Providing a report for the changes that the attacker have made

The enhanced component provides a feature for storing the changes that the attacker has made to the web application a GUI of the report section with the changes that has been done during the testing attack. It shows the changes that have been done. The administrator can view both the original and the changes by clicking the log option as shown in fig. 6.
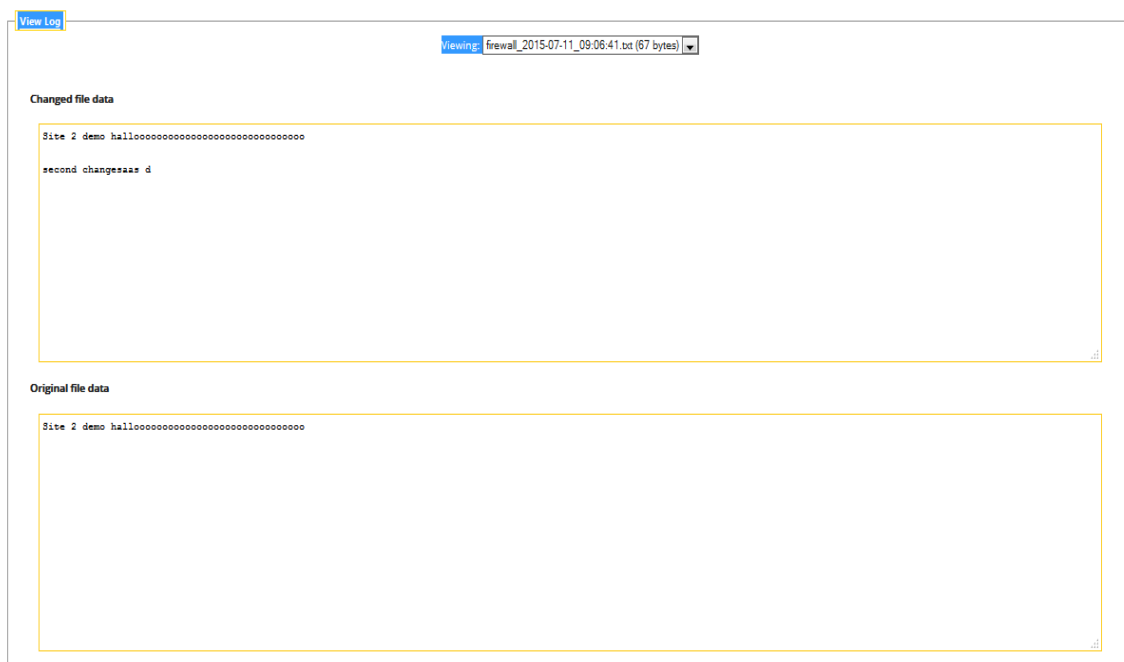
FIGURE 6: GUI THAT SHOW THE ORIGINAL AND THE CHANGES THAT THE ATTACKER MADE

V.   CONCLUSION

This research presented a component that aims to enhance the performance of web application firewalls and reduce the possibility of causing damage after the attack occurrence.

The enhanced component and phases are explained to show the process of interaction between the administrator and the installed component.

This research has made the following contributions:

- Provided a solution to strengthen the integrity between the users and the web-application owners.

- Prevent major content losses inside the web application after the infiltration.

- The proposed component can produce a report for the changes that the attacker made in-side the web application.

- The proposed component provides an easy and flexible solution with an easy to use GUI.

REFERENCES

[1] Lodha S, Dhande S.**Web Database Security Techniques.**International Journal of Advance Research in Computer Science and Management Studies. 2014; 2 (3): 300-305.

[2] Dodge R. **Information Assurance and Security in the ACM/IEEE CS2013.** Ronald C. Dodge; Lynn Futcher. 8th World Conference on Information Security Education (WISE), Auckland, New Zealand. Springer, IFIP Advances in Information and Communication Technology, AICT-406, 2017, Feb, pp.48-57.

[3] J. Gupta A, Kaur K. **Vulnerability Assessmentand Penetration Testing.** International Journal of Engineering Trends and Technology. 2013; 4 (3): 328-333.

[4] Subramanian T.K, Deepa B. **Security Attack Issues And Mitigation Techniques In Cloud Computing Environments**. International Journal of UbiComp (IJU), 2016; 7 (1): DOI:10.5121/iju.2016.7101.

[5] Reddy D. et al. **Detecting Attacks and Protecting From single To Multi Level application.** International Journal of Advanced Technology in Engineering and Science. 2015; 3 (1): 478 – 484.

[6] Laranjeiro N, et al. **A Learning-Based Approach to Secure Web Services from SQL/XPath Injection Attacks.** Pacific Rim International Symposium on Dependable Computing IEEE. 2010; 10 (24): 191-198.

[7] Hidhaya S, Angelina G. **Intrusion Protection against SQL Injection Attacks Using a Reverse Proxy.** Recent Trends in Computer Networks and Distributed Systems Security Communications in Computer and Information Science. 2012; 335: 252-263.

[8] Bangre S, Jaiswal A, et al. **SQL Injection Detection and Prevention Using Input Filter Technique**. International Journal of Recent Technology and Engineering (IJRTE). 2012; 1 (2): 145-150.

[9] Win W, Htun H. **Detection of SQL Injection Attacks by Combining Static Analysis and Runtime Validation.** International Conference on Advances in Engineering and Technology. 2014; 3 (20): 95-99.

[10] Aljawarneh S, Laing C, Paul Vickers. **Verification of Web Content Integrity: A new approach to protecting servers against tampering**. School of Computing, Engineering & Information Sciences North Umbria University, Newcastle upon Tyne.2013; 1-6.

[11] Shahriar H, North S, Chen W. **Early Detection Of sql Injection Attacks**. International Journal of Network Security & Its Applications. 2013; 5 (4): 53 -65.

[12] Ogini N, Ogwara N. **Securing Database passwords using a combination of hashing and salting techniques**. IPASJ International Journal of Computer Science (IIJCS). 2014; 2 (8): 52-58.

[13] Rewatkar L, Lanjewar U. **Implementation of Cloud Computing on Web Application. International Journal of Computer Applications**. 2010; 2 (8): 28-32.

Adaptive State Observer Synthesis Based On Instrumental Variables Method

Nikola Nikolov[1], Mariela Alexandrova[2], Ivelina Zlateva[3]

Department of Automation, Technical University of Varna, Bulgaria
Corresponding Authors Email: m_alexandrova@tu-varna.bg

Abstract— *The present paper presents non-recurrent adaptive observation algorithm for SISO linear time-invariant discrete systems. The algorithm is based on the instrumental variables method and the adaptive state observer estimates the parameters, the initial and the current state vectors of discrete systems. The algorithm workability is proved by using simulation data in the MATLAB/Simulink environment.*

Keywords— *adaptive observation, discrete adaptive state observer, non-recurrent algorithm, initial and current state vector estimation.*

I.   INTRODUCTION

State feedback control system design is often related to reconstruction of the state vector by measurements of the output variable and the input signal of the open loop system.

The reconstruction of the state vector is only possible by implication of state observer and the adaptive observation problem is related to observer synthesis with parameter estimator [6,7]. The matrices A and b or c (depending on the canonical form chosen for state space representation) are considered unknown.

The parameters are being estimated and the unknown matrices are determined during the observation process and the state vector is reconstructed.

The present paper investigates a non-recurrent algorithm for adaptive observation of single input single output (SISO) linear time invariant (LTI) discrete systems developed on the basis of the instrumental variables (IV) method [2].

The parameters estimator built-in in the adaptive observer is based on a simplified calculation procedure which also includes inversion of the informative matrix [5].

II.   PROBLEM FORMULATION

The system investigated is presented in the state space with the following systems of equations:

$$x(k + 1) = Ax(k) + bu(k), \qquad x(0) = x_0$$
$$y(k) = c^T x(k) + f(k) \qquad k = 0,1,2, \dots \tag{1}$$

where:

$$A = \begin{bmatrix} \mathbf{0} & \vdots & \mathbf{I_{n-1}} \\ \cdots & \cdots & \cdots \\ & \mathbf{a^T} & \end{bmatrix} \tag{2}$$

$$a = \begin{bmatrix} a_1 \\ a_2 \\ \vdots \\ a_n \end{bmatrix}; \; b = \begin{bmatrix} b_1 \\ b_2 \\ \vdots \\ b_n \end{bmatrix}; \; c = \begin{bmatrix} 1 \\ 0 \\ \vdots \\ 0 \end{bmatrix} \tag{3}$$

The system order n is a-priori known, $x(k) \in R^n$ is the unknown current state vector, $x(0) \in R^n$ is the unknown initial state vector, $u(k) \in R^l$ is a scalar input signal, $y(k) \in R^l$ is a scalar output signal, $f(k)$ is an additive noise signal, a and b are unknown vector parameters.

The following discrete transfer function corresponds to (1):

$$W(z) = \frac{h_1 z^{n-1} + h_2 z^{n-2} + \dots + h_{n-1} z + h_n}{z^n - a_n z^{n-1} - \dots - a_2 z - a_1} \tag{4}$$

The conformity between the elements b_i of vector $\boldsymbol{b}$ in relation to the chosen phase canonical form for representation and the coefficients h_i of the polynomial in the numerator of the discrete transfer function (4) are defined by the following expression[4]:

$$\boldsymbol{Tb} = \boldsymbol{h} \tag{5}$$

where:

$$\boldsymbol{h}^T = [h_1 \quad h_1 \quad \cdots \quad h_n]$$

$$\boldsymbol{T} = \begin{bmatrix} 1 & 0 & \cdots & 0 & 0 \\ -a_n & 1 & \cdots & 0 & 0 \\ -a_{n-1} & -a_n & \cdots & 0 & 0 \\ \vdots & \vdots & \ddots & \vdots & \vdots \\ -a_2 & -a_3 & \cdots & -a_n & 1 \end{bmatrix}$$

The elements a_i of vector $\boldsymbol{a}$, in relation to the chosen phase coordinate canonical form for representation, are the coefficients of the polynomial in the denominator of the discrete transfer function (4) presented in reversed order and with an opposite sign.

The problem to be solved is estimation of the unknown vector parameters $\boldsymbol{a}$ and $\boldsymbol{b}$, the initial state vector $\boldsymbol{x}(0)$ and the current state vector $\boldsymbol{x}(k)$, $k = 1,2, ...$

III.   SOLUTION

3.1   Algorithm for adaptive observation based on the instrumental variables (IV) method

The developed algorithm is based on the below calculation procedure:

Step 1.Form the input-output data massive [3,8]:

$$\boldsymbol{u}_1 = [u(0) \quad u(1) \quad \cdots \quad u(N-2)]$$

$$\boldsymbol{y}_1 = [y(0) \quad y(1) \quad \cdots \quad y(N-1)]$$

$$\boldsymbol{y}_2 = \left[y(n) \quad y(n+1) \quad \cdots \quad y\left(\frac{N-n}{2}+n-1\right) \right]^T$$

$$\boldsymbol{y}_3 = \left[y\left(\frac{N-n}{2}+n\right) \quad y\left(\frac{N-n}{2}+n+1\right) \quad \cdots \quad y(N-1) \right]^T$$

$$\boldsymbol{Y}_{11} = \begin{bmatrix} -y(n-1) & -y(n-2) & \cdots & -y(0) \\ -y(n) & -y(n-1) & \cdots & -y(1) \\ -y(n+1) & -y(n) & \cdots & -y(2) \\ \vdots & \vdots & \ddots & \vdots \\ -y\left(\frac{N-n}{2}+n-2\right) & -y\left(\frac{N-n}{2}+n-3\right) & \cdots & -y\left(\frac{N-n}{2}-1\right) \end{bmatrix}$$

$$\boldsymbol{Y}_{21} = \begin{bmatrix} -y\left(\frac{N-n}{2}+n-1\right) & -y\left(\frac{N-n}{2}+n-2\right) & \cdots & -y\left(\frac{N-n}{2}\right) \\ -y\left(\frac{N-n}{2}+n\right) & -y\left(\frac{N-n}{2}+n-1\right) & \cdots & -y\left(\frac{N-n}{2}+1\right) \\ -y\left(\frac{N-n}{2}+n+1\right) & -y\left(\frac{N-n}{2}+n\right) & \cdots & -y\left(\frac{N-n}{2}+2\right) \\ \vdots & \vdots & \ddots & \vdots \\ -y(N-2) & -y(N-3) & \cdots & -y(N-n-1) \end{bmatrix}$$

$$\boldsymbol{U}_{12} = \begin{bmatrix} u(n-1) & u(n-2) & \cdots & u(0) \\ u(n) & u(n-1) & \cdots & u(1) \\ u(n+1) & u(n) & \cdots & u(2) \\ \vdots & \vdots & \ddots & \vdots \\ u\left(\frac{N-n}{2}+n-2\right) & u\left(\frac{N-n}{2}+n-3\right) & \cdots & u\left(\frac{N-n}{2}-1\right) \end{bmatrix}$$

$$U_{22} = \begin{bmatrix} u\left(\dfrac{N-n}{2}+n-1\right) & u\left(\dfrac{N-n}{2}+n-2\right) & \cdots & u\left(\dfrac{N-n}{2}\right) \\ u\left(\dfrac{N-n}{2}+n\right) & u\left(\dfrac{N-n}{2}+n-1\right) & \cdots & u\left(\dfrac{N-n}{2}+1\right) \\ u\left(\dfrac{N-n}{2}+n+1\right) & u\left(\dfrac{N-n}{2}+n\right) & \cdots & u\left(\dfrac{N-n}{2}+2\right) \\ \vdots & \vdots & \ddots & \vdots \\ u(N-2) & u(N-3) & \cdots & u(N-n-1) \end{bmatrix}$$

Where Y_{11}, Y_{21}, U_{12} and U_{22} are Toeplitz matricesand $N = 3n + 2l, l = 1,2,3, \dots$

Step 2. Calculate the sub-matrices $G_{11}, G_{12}, G_{21}, G_{22}$:

$G_{11} = Y_{11}^T Y_{11} + Y_{21}^T Y_{21}; G_{12} = Y_{11}^T U_{12} + Y_{21}^T U_{22}; G_{21} = U_{12}^T Y_{11} + U_{22}^T Y_{21}; G_{22} = U_{12}^T U_{12} + U_{22}^T U_{22}$

Step 3. Calculate the covariance matrix C:

$$C = \begin{bmatrix} M_1 + M_1 G_{12} M_2 G_{21} M_1 & \vdots & -M_1 G_{12} M_2 \\ \cdots\cdots\cdots\cdots\cdots\cdots\cdots\cdots & \cdots & \cdots\cdots\cdots\cdots \\ -M_2 G_{21} M_1 & \vdots & M_2 \end{bmatrix}$$

where:

$M_1 = G_{11}^{-1}; M_2 = (G_{22} - G_{21} M_1 G_{12})^{-1}$

Step 4. Calculate the vectors $\hat{h}$ and $\hat{a}$ by using the following vector-matrix system and form the estimated system matrix $\hat{A}$:

$$\hat{p} = C \begin{bmatrix} Y_{11}^T y_2 + Y_{21}^T y_3 \\ U_{12}^T y_2 + U_{22}^T y_3 \end{bmatrix}$$

$\hat{h} = [\hat{h}_1 \quad \hat{h}_2 \quad \cdots \quad \hat{h}_n]^T = [\hat{p}_{n+1} \quad \hat{p}_{n+2} \quad \cdots \quad \hat{p}_{2n}]^T; \hat{a} = [\hat{a}_1 \quad \hat{a}_2 \quad \cdots \quad \hat{a}_n]^T = [-\hat{p}_n \quad -\hat{p}_{n-1} \quad \cdots \quad -\hat{p}_1]^T$

$$\hat{A} = \begin{bmatrix} 0 & \vdots & I_{n-1} \\ \cdots & \cdots & \cdots \\ & \hat{a}^T & \end{bmatrix}$$

Step 5. Calculate vector b estimation by implementing the following linear algebraic system of equations:

$$T\hat{b} = \hat{h}$$

where: $T = \begin{bmatrix} 1 & 0 & 0 & \cdots & 0 & 0 \\ -\hat{a}_n & 1 & 0 & \cdots & 0 & 0 \\ -\hat{a}_{n-1} & -\hat{a}_n & 1 & \cdots & 0 & 0 \\ \vdots & \vdots & \vdots & \ddots & \vdots & \vdots \\ -\hat{a}_2 & -\hat{a}_3 & -\hat{a}_4 & \cdots & -\hat{a}_n & 1 \end{bmatrix}$ is a lower triangular Toeplitz matrix.

Step 6. Estimate the initial state vector x_0:

$$\hat{x}_0 = (D^T D)^{-1} D^T (y_1 - Q u_1) = [\hat{x}_{01} \quad \hat{x}_{02} \quad \cdots \quad \hat{x}_{0n}]^T$$

(applicable only in case that $det(D^T D) \neq 0$), where:

$$D = \begin{bmatrix} c^T \\ c^T \hat{A} \\ c^T \hat{A}^2 \\ \vdots \\ c^T \hat{A}^{(N-1)} \end{bmatrix}_{(N\times n)}; Q = \begin{bmatrix} 0 & 0 & \cdots & 0 \\ c^T \hat{b} & 0 & \cdots & 0 \\ c^T \hat{A}\hat{b} & c^T \hat{b} & \cdots & 0 \\ \vdots & \vdots & \ddots & \vdots \\ c^T \hat{A}^{(N-2)}\hat{b} & c^T \hat{A}^{(N-3)}\hat{b} & \cdots & c^T \hat{b} \end{bmatrix}_{(N\times(N-1))}$$

Step 7. Calculate the estimate of the output variable $y(k)$:

$$\hat{x}(k + 1) = \hat{A}\hat{x}(k) + \hat{b}u(k), \qquad \hat{x}(0) = \hat{x}_0$$
$$\hat{y}(k) = c^T \hat{x}(k) \qquad\qquad k = 0,1,2, \dots, N-1$$

$$\hat{F} = \hat{A} - gc^T$$

Step 8. For the instrumental matrices V_{11}, V_{21}:

$$V_{11} = \begin{bmatrix} -\hat{y}(n-1) & -\hat{y}(n-2) & \cdots & -\hat{y}(0) \\ -\hat{y}(n) & -\hat{y}(n-1) & \cdots & -\hat{y}(1) \\ -\hat{y}(n+1) & -\hat{y}(n) & \cdots & -\hat{y}(2) \\ \vdots & \vdots & \ddots & \vdots \\ -\hat{y}\left(\frac{N-n}{2}+n-2\right) & -\hat{y}\left(\frac{N-n}{2}+n-3\right) & \cdots & -\hat{y}\left(\frac{N-n}{2}-1\right) \end{bmatrix}$$

$$V_{21} = \begin{bmatrix} -\hat{y}\left(\frac{N-n}{2}+n-1\right) & -\hat{y}\left(\frac{N-n}{2}+n-2\right) & \cdots & -\hat{y}\left(\frac{N-n}{2}\right) \\ -\hat{y}\left(\frac{N-n}{2}+n\right) & -\hat{y}\left(\frac{N-n}{2}+n-1\right) & \cdots & -\hat{y}\left(\frac{N-n}{2}+1\right) \\ -\hat{y}\left(\frac{N-n}{2}+n+1\right) & -\hat{y}\left(\frac{N-n}{2}+n\right) & \cdots & -\hat{y}\left(\frac{N-n}{2}+2\right) \\ \vdots & \vdots & \ddots & \vdots \\ -\hat{y}(N-2) & -\hat{y}(N-3) & \cdots & -\hat{y}(N-n-1) \end{bmatrix}$$

Step 9. Recalculate the submatrices G_{11} and G_{12}:

$$G_{11} = V_{11}^T Y_{11} + V_{21}^T Y_{21}; \; G_{12} = V_{11}^T U_{12} + V_{21}^T U_{22}$$

Step 10. Recalculate the parameters vector p:

$$M_1 = G_{11}^{-1}; M_2 = (G_{22} - G_{21} M_1 G_{12})^{-1}$$

$$C = \begin{bmatrix} -M_2 G_{22} M_1 & \vdots & M_2 \\ \cdots\cdots\cdots\cdots\cdots\cdots\cdots & \cdots & \cdots\cdots\cdots\cdots \\ M_1 + M_1 G_{11} M_2 G_{22} M_1 & \vdots & -M_1 G_{11} M_2 \end{bmatrix}; \; \hat{p} = C \begin{bmatrix} V_{11}^T y_2 + V_{21}^T y_3 \\ U_{12}^T y_2 + U_{22}^T y_3 \end{bmatrix}$$

$$\hat{h} = [\hat{h}_1 \quad \hat{h}_2 \quad \cdots \quad \hat{h}_n]^T = [\hat{p}_{n+1} \quad \hat{p}_{n+2} \quad \cdots \quad \hat{p}_{2n}]^T; \; \hat{a} = [\hat{a}_1 \quad \hat{a}_2 \quad \cdots \quad \hat{a}_n]^T = [-\hat{p}_n \quad -\hat{p}_{n-2} \quad \cdots \quad -\hat{p}_1]^T$$

$$\hat{A} = \begin{bmatrix} 0 & \vdots & I_{n-1} \\ \cdots & \cdots & \cdots \\ & \hat{a}^T & \end{bmatrix}$$

Step 11. Repeat steps 7 to 10 four times

Step 12. Estimate the current state vector $x(k)$:

$$\hat{x}(k+1) = \hat{F}\hat{x}(k) + \hat{b}u(k) + gy(k), \hat{x}(0) = \hat{x}_0; \; \hat{F} = \hat{A} - gc^T$$

Vector g can be easily obtained by solving the pole placement problem (PPP) also known as pole assignment problem (PAP). The synthesis of vector g must take into consideration the following options: the eigen values of the matrix $\hat{F}$ should be zeros or should be spread into the unit circle closer to the origin than the matrix $\hat{A}$ eigenvalues. The implementation of the above listed options ensures good dynamic characteristics of the observer synthesized.

IV. SIMULATION RESULTS

The simulation is held in MATLAB programming environment under the below conditions:

➤ For a given transfer function of the system under investigation, with input signal $u(k)$ and the respective output signal $y(k)$;

➤ Added colored noise signal $f(k)$ is applied to the system output;

➤ The input signal $u(k)$ and the noise-corrupted output signal $y(k)$ are used as an input data for the observation algorithm;

➤ Based on the input-output data massive, the algorithm developed calculates the estimates of the open loop system and the state vector.

The discrete transfer function of the system investigated, used for the simulations is presented as follows:

$$W(z) = \frac{0.6z^{-1} + 0.56z^{-2} + 0.2125z^{-3} + 0.308z^{-4} + 0.5488z^{-5} + 0.7221z^{-6}}{1 - 1.4z^{-1} + 0.7875z^{-2} - 0.2275z^{-3} + 0.035525z^{-4} - 0.002835z^{-5} + 0.00009z^{-6}}$$

and its corresponding representation in state space:

$$a = \begin{bmatrix} -0.00009 \\ 0.002835 \\ -0.035525 \\ 0.2275 \\ -0.7875 \\ 1.4 \end{bmatrix}; \; b = \begin{bmatrix} 0.6 \\ 0.2 \\ 0.1 \\ 0.3 \\ 0.4 \\ 0.5 \end{bmatrix}; \; c = \begin{bmatrix} 1 \\ 0 \\ 0 \\ 0 \\ 0 \\ 0 \end{bmatrix}; \; x(0) = \begin{bmatrix} 1 \\ 1 \\ 1 \\ 1 \\ 1 \\ 1 \end{bmatrix}$$

The matrix A eigenvalues are obtained by using $eig(.)$ function in MATLAB:

$$eig(A) = \begin{bmatrix} 0.4 & 0.3 & 0.25 & 0.2 & 0.15 & 0.1 \end{bmatrix}^T$$

Pseudo-random binary sequence (PRBS) is used as an input signal $u(k)$ which is generated in MATLAB by using the following functions: $u = \left(sign\left(randn(127,1)\right)\right) * 10$.

The output signal $y(k)$ is noise-corrupted by adding a color noise $f(k)$. The colored noise is obtained by filtering of white noise through filter with the following transfer function:

$$W_f(z) = \frac{1}{1 - 1.4z^{-1} + 0.7875z^{-2} - 0.2275z^{-3} + 0.035525z^{-4} - 0.002835z^{-5} + 0.00009z^{-6}}$$

The noise level η is calculated mathematically by division of the noise standard deviation σ_f to the output signal standard deviation σ_y in accordance with the equation given below:

$$\eta = \frac{\sigma_f}{\sigma_y}.100 = (0 \div 10)\%$$

Vector a estimation error e_a, vector b estimation error e_b and the state vector $x(k)$ estimation error e_x are relative mean squared errors (RMSE) and could be determined by the following equations:

$$e_a(k) = -\sqrt{\frac{\sum_{i=1}^{n}\left(a_i(k)-\hat{a}_i(k)\right)^2}{\sum_{i=1}^{n} a_i(k)}}; \; e_b(k) = -\sqrt{\frac{\sum_{i=1}^{n}\left(b_i(k)-\hat{b}_i(k)\right)^2}{\sum_{i=1}^{n} b_i(k)}}; \; e_x(k) = -\sqrt{\frac{\sum_{i=1}^{n}\left(x_i(k)-\hat{x}_i(k)\right)^2}{\sum_{i=1}^{n} x_i(k)}}$$

The results for the case of noise-free output signal (i.e. $f(k) = 0$) and $l = 0$ (i.e. minimum number of the input-output measurements: $N = 3n = 18$) are shown in Fig.1. In accordance with the initial settings the algorithm will start working at the 18th step of the calculations and in this case in particular the observation errors $e_a(k), e_b(k)$ and $e_x(k)$ are zeros.
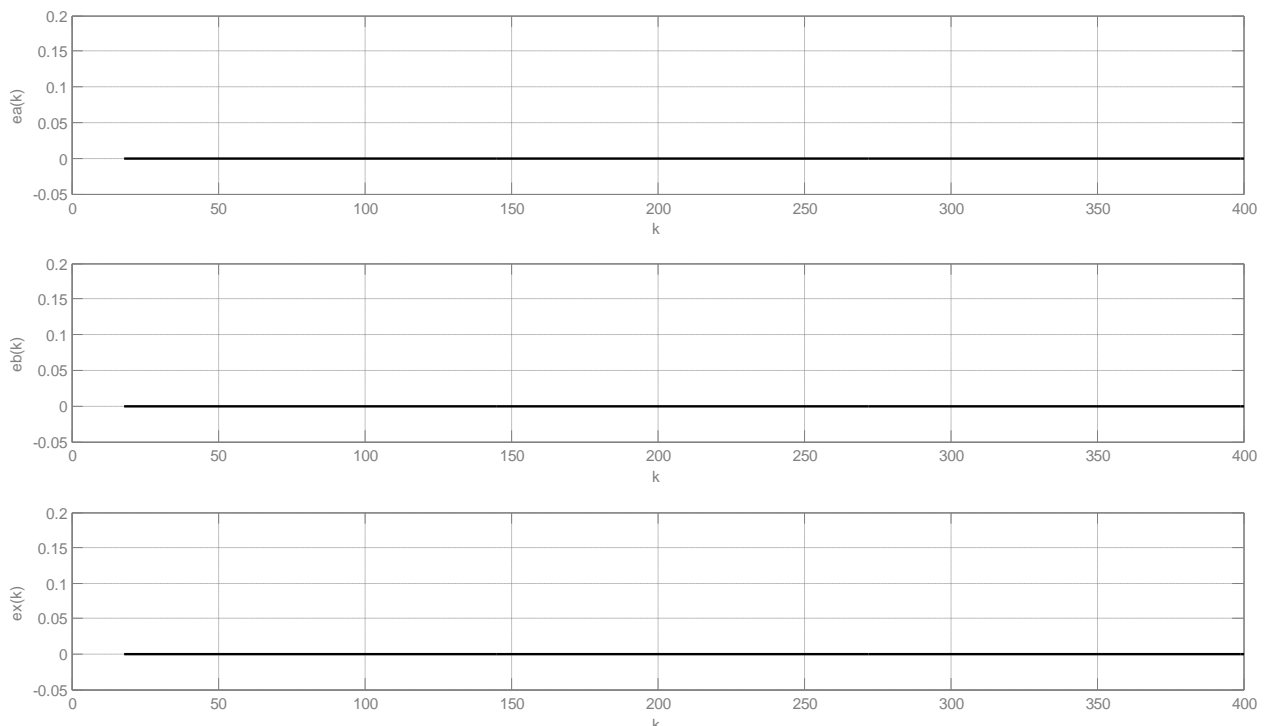
FIGURE 1. RMSE FOR THE CASE OF NOISE-FREE OUTPUT SIGNAL

In the case of noise-corrupted output signal an experiment is carried out for noise level $\eta = 10.018\%$ and $l = 40$ (i.e. $N = 3n + 2l = 98$). The results are shown in Fig.2. Under the above described initial settings the algorithm will start working at the 98th step of the calculations and the RMSE are as follows: $e_a(k) < 0.033, e_b(k) < 0.010, e_x(k) < 0.065$.
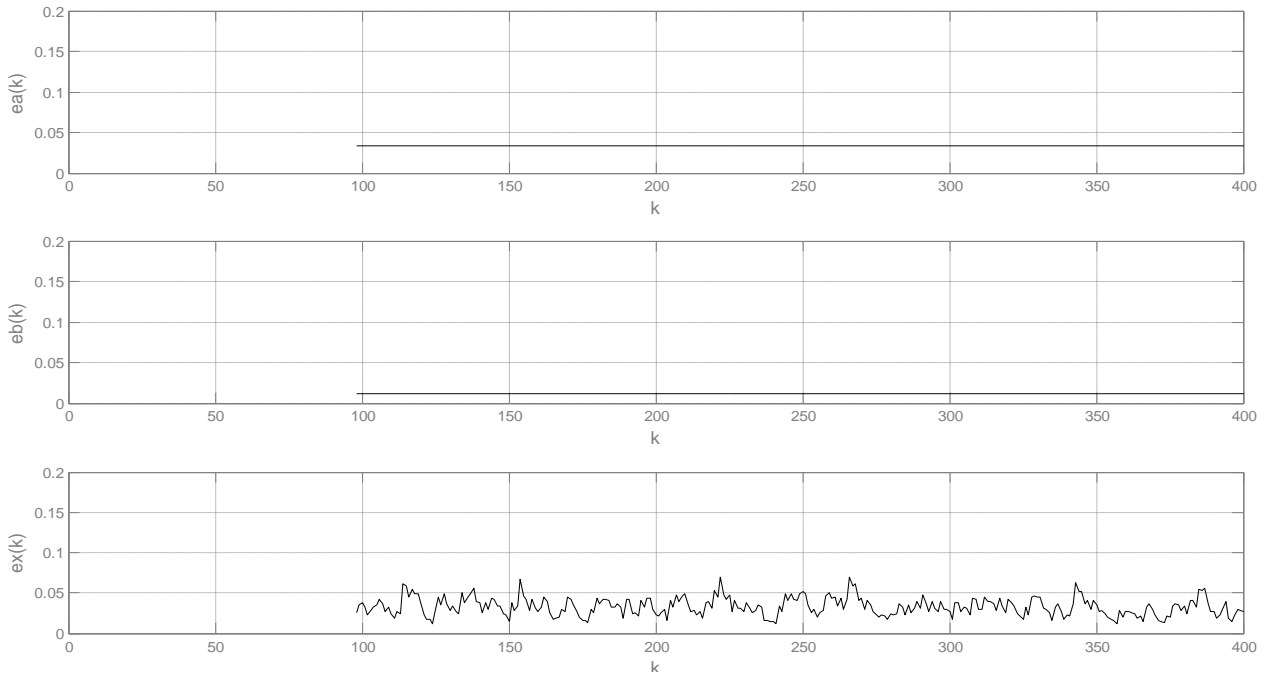
FIGURE 2. RMSE FOR THE CASE OF NOISE-CORRUPTED OUTPUT SIGNAL,$\eta = 10.018\%, N = 3n + 2l = 98$

An additional experiment is carried out for the provisions of noise-corrupted output signal analysis for noise level $\eta = 10.014\%$ and $l = 100$ (i.e. $N = 3n + 2l = 218$). The results show that the algorithm starts working at the 218th step of the calculations and the RMSE are as follows: $e_a(k) < 0.017, e_b(k) < 0.0057, e_x(k) < 0.024$, under the condition:$218 < k > 400 \Rightarrow e_x(k) = 0.01$ (see Fig.3).

FIGURE 3. RMSE FOR THE CASE OF NOISE-CORRUPTED OUTPUT SIGNAL,$\eta = 10.014\%, N = 3n + 2l = 218$

The simulation results delivered and graph analysis show that with the increase in number of the input-output measurements (N), the algorithm invariance to added noises increases proportionally however the time needed for collection of initial information rises.

V. CONCLUSIONS

The algorithm suggested for open loop system parameter estimations which serve as a basis for further reconstruction of the current state vector implements the method of the instrumental variables excluding the zero iteration which only uses the least squares method (steps 1 to 4 of the suggested calculation procedure).

The algorithm proposed estimates as well the initial state vector x_0 which allows the forming of the instrumental variables matrix even for nonzero initial conditions.
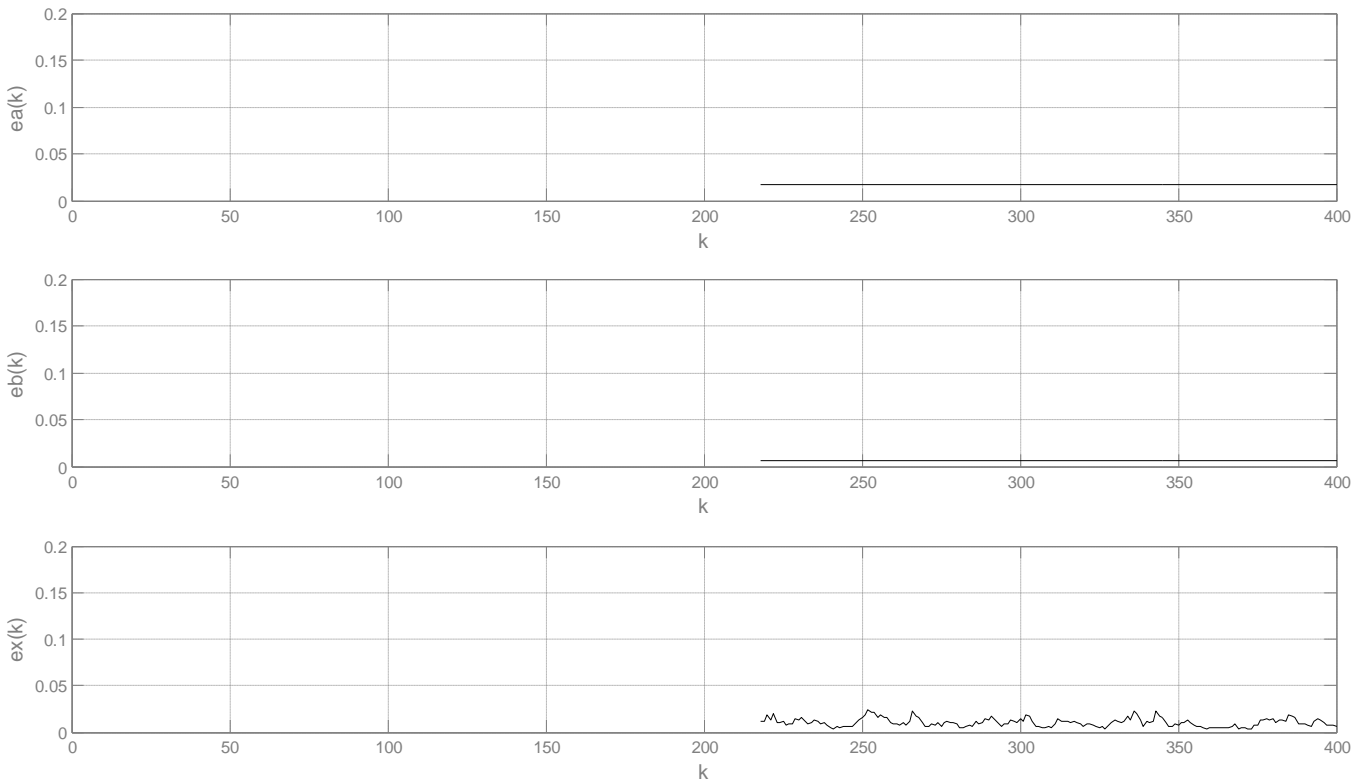
The results delivered show that the number of the input output data measurements (N) is of high significance in relation to accuracy of estimations in the case of noise corrupted output. The highest accuracy is to be expected for highest counts of N (see Fig.2 and Fig.3).

The method of the IV method gives best results in case of estimation of a-priori collection of data [3,8], however in relation to the closed loop system the added noise $f(k)$ is transferred to the input signal through the feedback channel. Thus invariance between the instrumental matrices and the added noise is not possible; it is only possible that the estimates are unbiased and significant in presence of a white noise however the real systems do not allow such solution of the problem. The used of IV method for investigation of the closed loop system is only applicable if additional input signal is implemented [8]. For this reason the implementation of the algorithm suggested above is not recommended for closed systems implications.

The algorithm for adaptive observation based on the instrumental variables (IV) method introduced in the present paper is developed on the basis of non-recurrent method which ensures the convergence of the iterative procedure [1,2].

The most positive feature of this algorithm however is related to the method used for informative matrix formation. It is formed through the four sub-matrices Y_{11}, Y_{21}, U_{12} and U_{22} which reduces the calculation complexity of the procedure for inversion of matrix G formed by the sub-matrices $G_{11}, G_{12}, G_{21}, G_{22}$. Independently of the N count in numbers for the estimation of the coefficients h_i and a_i is only needed to be inverted the matrices G_{11} and $(G_{22} - G_{21}M_1G_{12})$ which are always guaranteed $(n \times n)$ dimensions. In all other cases this procedure is related to inversion of a matrix at least $(N - n) \times (N - n)$ dimensional.

REFERENCES

[1] D.M. Strong, Iterative Methods for Solving Ax = b - Convergence Analysis of Iterative Methods, Journal of Online Mathematics and its Applications, 2005, https://www.maa.org/press/periodicals/loci/joma/iterative-methods-for-solving-iaxi-ibi-convergence-analysis-of-iterative-methods.

[2] I.D. Landau, R. Lozano, M. M'Saad, A. Karimi, Adaptive Control: Algorithms, Analysis and Applications, Second Edition, Springer, 2011.

[3] I. Vuchkov, Identification, Sofia, Yurapel Press, 1996 (in Bulgarian).

[4] L.N. Sotirov, Control Theory – part II, Technical University of Varna, 2000 (in Bulgarian).

[5] L.N. Sotirov, V. S. Dimitrov, N. N. Nikolov, Discrete Adaptive State Observer for Real-time, International conference "Automatics and Informatics'04", pp. 121-124, Sofia, Oct 2004.

[6] N. Nikolov, M. Alexandrova, V. Valchev, O.Stanchev, Adaptive State Observer Development Using Extended Recursive Least-Squares Method, 40th Jubilee International Convention on Information and Communication Technology, Electronics and Microelectronics (MIPRO), Proceedings pp.133-137, ISBN 978-953-233-093-9, 22-26 May, 2017, Opatija, Croatia.

[7] N. Nikolov, V. Lukov, M. Alexandrova, Discrete Adaptive Real-Time State Observer Development Using Least-Squares Method, XXVI International Scientific Conference electronics-ET2017, September 13-15, 2017, Sozopol, Bulgaria.

[8] T. Säderström, P. Stoica, System identification, Prentice Hall, New Jersey, Engle wood Cliffs, 1989.

Design of Alternative Automatic Transmission for Electric Mopeds

Ameya Bhusari[1], Saurabh Rege[2]

[1]Department of Mechanical, Maharashtra Institute of Technology, PUNE-38
[2]Department of Mechanical, Modern College of Engineering, PUNE-05

Abstract— *The number of automobiles has seen an alarming rise in the recent years. In the year 2014, the number of road vehicles produced annually increased to 87.23 million vehicles from around 40 million in 2000. This shows that production has increased to more than twice the volume in only 14 years. This has also caused a rise in the pollution levels. Global CO2 levels are on the rise due to increased pollution, contributing to the greenhouse effect. Hence it is very important to reduce our dependency on gasoline driven vehicles. Electric vehicles are a good alternative to these. The advent of electric vehicles is marred by factors like unavailability of charging stations and most importantly not being able to match the performance parameters offered by gasoline driven vehicles. Hence a driveline setup has been designed to increase the performance parameters like gradeability and top speed of an electric moped to set it at par with the gasoline powered mopeds available on the market. In this report we will focus on the design considerations, working principle and the mechanism for the said driveline as well as the design calculations and the CAD model.*

Keywords— *automatic, centrifugal clutch, drive train, electric vehicles, freewheel, mopeds, transmission.*

I. INTRODUCTION

Electric vehicles are said to be the future of the automobile technology. There are overwhelming advantages of electric vehicles over gasoline vehicles. With gasoline-electric hybrid power and all-electric power, we can achieve significant cost and environmental savings. By adding more batteries and recharging capability to gasoline-electric hybrid vehicles, we can have plug-in hybrids that offer the range of hybrids (500 miles or more), plus the benefit of all-electric power for short trips, which dramatically reduces the amount of gasoline used. EVs require no gasoline whatsoever and, when recharged from renewable energy sources, produce zero total emissions. In fact, even if we switched from gasoline cars to EVs and plug-in hybrids recharged by our existing utility grids (which mostly use fossil fuels), we would see a 42% national average reduction in CO2 emissions, according to research by Peter Lilienthal of the National Renewable Energy Laboratory. According to a study, the yearly cost of operating 50 miles per gallon vehicle is $1275 while the same for operating an electric vehicle is just $216. The main issue with using an electric vehicle, in this case an electric moped is the lack of performance. Electric mopeds fall very short in the performance parameters like gradeability, torque and top speed as compared to the gasoline mopeds dominating the market today. The maximum speed possible with an electric moped is just around 16 mph as compared to 40-50 mph top speed of their gasoline counterparts. Hence a mechanical system has been designed which offers both greater power and greater torque whenever the situation demands the need for the same.

II. LITERATURE REVIEW

5V. B. Bhandari in his book Design of Machine Elements talks about the various power transmitting components, their application and design. The design methodology explained in the book is considered while design of mechanical components like the two-stage gearbox, input and output sprockets, gear shafts etc. 1In the book, Electric Vehicle Technology Explained, James Larminie and John Lowry explain the history and evolution of electric vehicles in terms of their technology and various features that have developed over the years. The book also talks about the various components of the electric drive system like the motor, their types and their development that improve vehicle characteristics such as speed, range, safety and reliability. 2F. K. Sully in Motor vehicle mechanic's Textbook emphasizes the importance of automatic transmissions in automobiles. He describes the common kinds of automatic transmission modes that are widely applied in current automobiles. The chapter talks about their advantages and disadvantages when used in different kinds of vehicles and ways in which they can be better implemented in the systems. 6The Motor Vehicle by T. K. Garrett, K. Newton and W. Steeds,

provides essential reference work for various transmission systems. It discusses in detail about the continuously variable transmission (CVT) and its components and how the system has been developed to be practically implemented in today's vehicles.

III.   OVERVIEW OF COMPONENTS

The transmission system comprises of three main components namely a single-speed two stage gearbox, a centrifugal clutch and freewheels.

3.1   Gearbox

An automobile requires high torque while climbing hills and while starting. On the other hand, while running on high speeds on level roads, high torque is not required due to the vehicle momentum. The purpose of a gearbox in a vehicle is to vary the torque on the output shaft according to the required condition. Thus, the gearbox helps to convert the high speed low torque power generating device (engine, motor, etc.) to a high torque power transmitting system. In this system a single-speed two stage gearbox is used to increase the torque on the output shaft.

The main components of a gearbox are:

3.1.1   Counter shaft

Counter shaft is the shaft that is connected with the power producing device of the system. It is coupled with power transmitting devices like gears to transmit the power to the main shaft. The counter shaft runs with the same speed or different speed as that of the power producing device due to the gear ratio provided between them.

3.1.2   Main Shaft

The main shaft is the shaft which is coupled to the output shaft or the wheel. It carries power from the counter shaft by the use of gears according to the gear ratio and it runs at different speed and torque as compared to the counter shaft.

3.1.3   Gears

Gears are used to transmit the power from one shaft to the other. They are the most important components of the transmission system as they are responsible for the variation in the torque and speed of the gearbox. This takes place due to the gear ratio or reduction ratio of the gears. The gear ratio or the reduction ratio is the ratio of the driven gear teeth to the driving gear teeth. If the gear ratio is greater than one, the main shaft revolves at lower speed than the counter shaft and the torque on the main shaft is higher than the torque on counter shaft. On the other hand, if the gear ratio is less than one, the main shaft revolves at higher speed than the counter shaft and the torque on the main shaft is lower than that on the counter shaft.

3.1.4   Bearings

Bearings are used to support the rotating shafts and reduce friction. In the gearbox the main shaft and the counter shaft are supported by the bearings.

3.2   Centrifugal Clutch:

A clutch is a power transmitting component used to connect the driving shaft to the driven shaft, so that the driven shaft may be started and stopped at will, without stopping the driving shaft. A clutch provides an interruptible connection between two shafts. The driving shaft is connected to a boss assembly that consists of a number of shoes and springs that move radially outwards. The driven shaft is connected to another hollow boss. When the two shafts are aligned, the boss assembly can revolve inside the hollow boss. When the driving shaft is rotated, the centrifugal force due to rotation causes the shoes to move radially outwards and come in contact with the hollow boss of the driven shaft. With enough rpm and centrifugal force, the shoes maintain contact with the rim of the hollow boss, thus transmitting power from the driving shaft to the driven shaft.

The friction material used on the shoes and the inner rim of the hollow boss help in maintaining contact, while the spring ensures ease in expansion and retraction and hence provide effective power transmission.

3.3   Freewheel Sprocket:

A freewheel is a device in a transmission system that disengages the driveshaft from the driven shaft when the driven shaft rotates faster than the driveshaft. It uses a ratchet and pawl mechanism. It consists of two saw-toothed discs, pressing against each other, with the toothed sides pressing. When rotating in one direction, the saw teeth of drive disc lock with the teeth of the driven disc, making it rotate at the same speed. If the drive disc slows down or stops rotating, the teeth of the driven disc slip over the drive disc teeth and continue rotating. A freewheel sprocket has this mechanism enclosed in a boss and the teeth of a sprocket attached on the outer rim of the boss.

3.4   Sprocket:

A sprocket wheel is a power transmission device that looks like a profiled wheel with teeth or cogs that mesh with a chain, track or other perforated or indented material. The main difference between a gear and a sprocket is that gears mesh with each other while sprockets mesh with a chain which intern transfer power to other sprockets. They are useful in transmitting power when the shafts are located at a significant distance from each other.

3.5   Drive Shaft:

A drive shaft is a mechanical component used for transmitting torque and rotation, usually used to connect other components of a drive train that cannot be connected directly because of the distance or the need to allow for relative movement between them. The drive shaft is connected to the output wheels in an automobile that help in the forward locomotion of the vehicle.
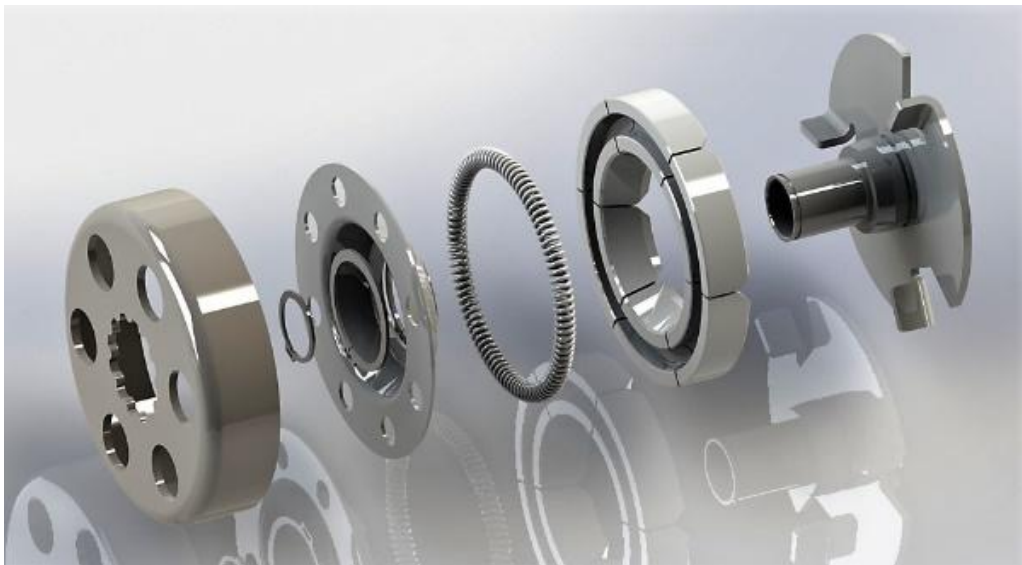
FIGURE 1: EXPLODED VIEW OF CENTRIFUGAL CLUTCH

IV.   BACKGROUND

Currently various modes of power transmission are implemented in vehicles. The most common modes are variable speed gearbox, continuously variable transmission (CVT), torque converter and hub drive systems. These systems face drawbacks such as reduced transmission efficiency, lower torque transmitting capacity, increased driver discomfort and higher costs. The electric vehicles inherently face certain issues like lower speeds, lower vehicle range, lack of charging infrastructure and higher costs. For the newly growing electric vehicle market, the implementation of such systems with drawbacks will seriously affect their impact and necessity among the customers. Thus, it has become important to develop a transmission system which can be effective in not only eliminating these flaws but also increase the performance of the electric vehicles. This automatic transmission system for electric vehicles enhances the performance parameters of the electric vehicle by increasing the torque on wheels thus providing better acceleration and gradeability as well as increasing the velocity of the

wheel at higher motor rpm thus increasing the top speed of the vehicle. This system provides very high efficiency and reliability. It is compact, light in weight and economical to manufacture. Being an automatic system, it provides comfort and ease in driving. It is a unique transmission system that can be incorporated in the modern day electric vehicles.

V. CONSTRUCTION AND WORKING

Figure 1 shows the diagram of the Automatic transmission system for electric vehicles. The motor and the driven wheel are connected by the automatic transmission system. The power source is an electric motor that has a double-ended shaft to ensure that power can be transmitted from both the sides of the motor. The transmission system consists of two drivelines connected on either side of the motor. One driveline consists of the gearbox coupled to the driven wheel using a chain and sprocket arrangement on one side while the other driveline consists of the centrifugal clutch coupled to the driven wheel using another chain and sprocket arrangement on the other side. Both the driven sprockets that have been coupled to the driven wheel have attached freewheel units that help convert the conventional sprockets into freewheel sprockets. The freewheel sprockets are bolted to the driven wheel that help the power transmission to the wheel in a single forward direction. The working of the two drivelines is as follows:

5.1 Driveline 1:

As the motor rpm increases from zero, the motor shaft, which also acts as the input shaft to the gearbox and the boss assembly of the centrifugal clutch, starts rotating. This drives gears on the counter shaft of the gearbox which intern drive the gears on the main shaft due to meshing of the gears. As the gears provide a higher reduction, the main shaft rotates at lower speed and can deliver higher torque. The main shaft of the gearbox is connected to the wheel by a chain and sprocket combination of which the output sprocket is the freewheel sprocket. On the other hand, the boss assembly that houses the shoes and springs, also rotates inside the hollow boss. Due to lower motor rpm, the centrifugal force created due to rotation is less and thus, the shoes do not expand enough to rotate the hollow boss and thus the output shaft of the centrifugal clutch. Hence, the power is transmitted only through driveline 1 as the motor rpm progresses from zero to increased revolutions. As the overall reduction through the gearbox side is higher, the transmission can provide a higher torque during starting conditions, as well as for climbing grades, thus providing maximum acceleration to the vehicle, up to the point when driveline 2 is engaged.

5.2 Driveline 2:

As the motor rpm increases, a continuously increasing centrifugal force acts on the shoes of the boss assembly of the centrifugal clutch. At a particular rpm, the shoes expand radially outward to the point where they make contact with the hollow boss of the centrifugal clutch. This rpm is called engagement rpm of the driveline 2. Due to a higher coefficient of friction between the inner rim of the hollow boss and the surface of the shoes, the hollow boss starts rotating along with boss assembly thus transferring power from the input shaft to the output shaft of the centrifugal clutch. As the output shaft of the centrifugal clutch is coupled with the driven wheel by a chain and sprocket combination, the power can now be transmitted through driveline 2. The driveline 2 offers a much lower reduction thus increasing the rpm of the driven wheel which eventually increases the top speed of the vehicle. Owing to driveline 2, as the driven wheel now rotates faster than the driving shaft of driveline 1, by the principle of freewheel design (ratchet and pawl mechanism) the freewheel sprocket disengages the power from driveline 1, and now the power is transmitted only through driveline 2. Thus, when the vehicle starts from static position or is about to climb an incline, driveline 1 is engaged which provides the required high torque and thus maximum acceleration to carry out the task. Once the vehicle gains momentum and increases its speed, the driveline 2 is engaged which provides higher speed and increases the maximum speed of the vehicle. As the driveline 2 engages, driveline 1 is disengaged due to the freewheel mechanism.

VI. CONCLUSION

The proposed automatic transmission for electric vehicles provides better acceleration as well as velocity as compared to the electric vehicles with the same power range. Thus, a lower wattage power source can be used with this system, which will also help in reducing the battery pack size, eventually reducing the weight of the vehicle. This can help in achieving a better range for the vehicle. As the system incorporates components like the gearbox, centrifugal clutch, chains and sprockets, the transmission efficiency and reliability are high while maintenance and manufacturing time and cost are low. The automatic system is easy to drive for amateur drivers and provides comfort reducing driver fatigue especially while riding in traffic. Hence, with some research the automatic transmission system can be effectively used in most modern day electric vehicles.
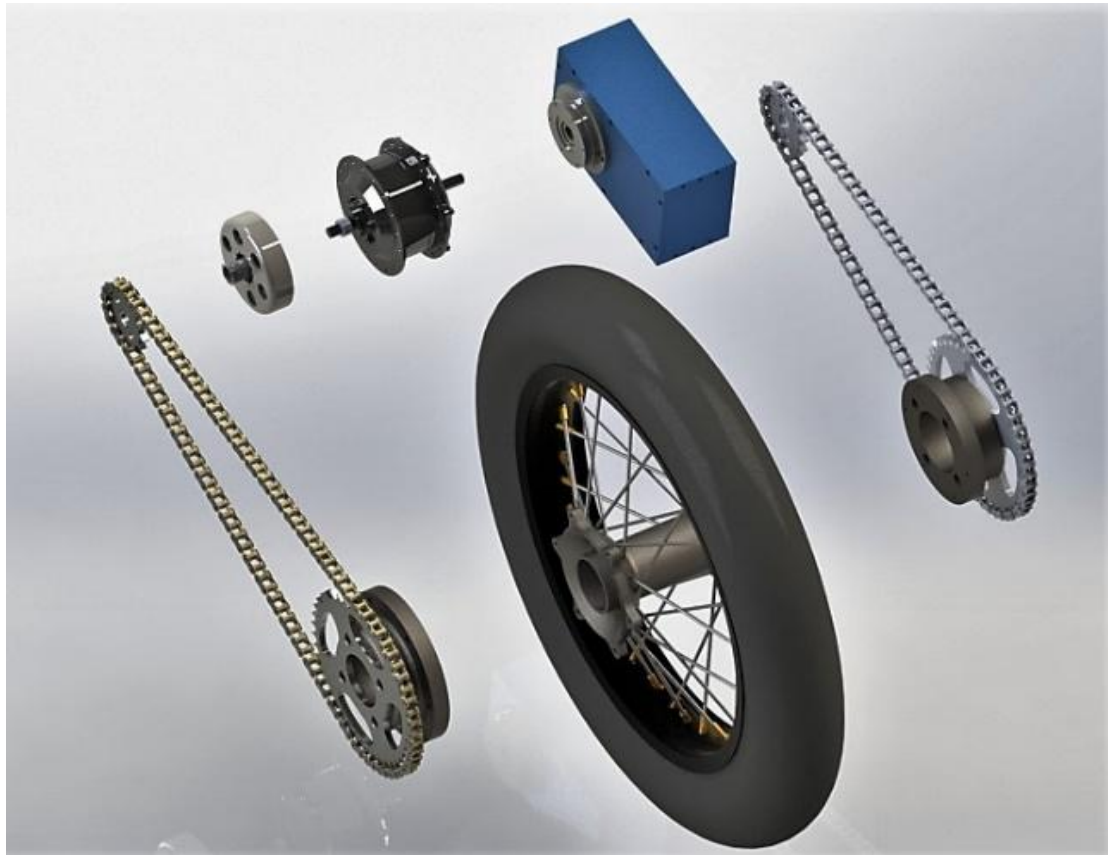
FIGURE 2: EXPLODED VIEW OF ENTIRE ASSEMBLY

VII.   FUTURE SCOPE

- The study does not include any design values and figures as they may vary according to various designs and applications. While incorporating the system into a particular vehicle with specific parameters and requirements, the system can be thoroughly designed.

- The study also does not include the manufacturing methodologies and processes used to build the system. Thus, the final system costs cannot be determined.

REFERENCES

[1] James Larminie and John Lowry, Electrical Vehicle Technology Explained,2003 John Wiley & Sons, ISBN: 0-470-85163-5.
[2] F.K. Sully, Automatic Transmission, Motor Vehicle Mechanics Textbook,1988, pp.235-240.
[3] H.Heisler, Semi and Fully Automatic Transmission, Advanced Vehicle Technology,2002,pp.117–192.
[4] Kirpal Singh, Automobile Engineering, Standard Publisher Distributors, 7th Edition, 1995.
[5] Bhandari V.B, Design of Machine Elements, Tata McGraw Hill Publishing Co. Ltd. 4th Edition, 1997.
[6] T.K. Garnett, K. Newton, W. Steeds, Semi-automaic gearboxes and continuously variable Transmission, Motor Vehicle, 2002, pp.841-863.
[7] R. Nicole, "Title of paper with only first word capitalized," J. Name Stand. Abbrev., in press.

Pharmacognostical, Phytochemical studies and Antibacterial activity of Wood from *Talipariti elatum* Sw. (Fryxell) in Cuba

José González[1*], Armando Cuéllar[2], Silvia C. Morales[3], Max Monan[4]

[1,2]Department of Pharmacy, Faculty of Pharmacy and Foods, Havana University, Cuba
[3]Department of Foods, Faculty of Pharmacy and Foods, Havana University, Cuba
[4]ARVARNAM, Martinica, France

Abstract— *A preliminary pharmacognostical and phytochemical evaluation of Talipariti elatum (Sw.) that grows in Cubawas realized to determine the macromorphology and micromorphology characteristics, the physicochemical and phytochemical parameters from the wood of this spice that grows in Cuba. This crude drug showed the characteristic physicochemical values such as moisture content (7.6 %), total ashes (1.14%), water soluble ashes (0.19 %), acid insoluble ashes (0.33 %) and extractable matter in ethanol at 70 % (10.87 %). Phytochemical screening revealed the possible presence of triterpenes and/or steroids, reductants sugars, tannins and/or phenolic compounds, flavonoids and bitter and astringent principles, realized under WHO parameters. The antibacterial activity of ethanolic extracts at 30, 50 and 70 % of the wood against Salmonella tiphymurium 14028, Bacillus cereus 11778, Escherichia coli 25922 and Staphylococcus aureus 25923showed varying degrees of inhibition on the tested organisms.*

Keywords— *Talipariti elatum, wood, pharmacognostical, phytochemical, antibacterial.*

I.   INTRODUCTION

The *Talipariti elatum* tree is quite attractive with its straight trunk, broad green leaves and hibiscus-like flowers (Fig.1). It grows quite rapidly, often attaining 20 meters (66 ft.) or more in height. The attractive flower changes color as it matures, going from bright yellow to orange red and finally to crimson. Endemic to West Indies; native to Cuba and Jamaica; cultivated in Hispaniola, Puerto Rico, Virgin Islands (Virgin Gorda), and Lesser Antilles (Dominica, Guadeloupe, Martinique, St. Lucia).The name mahoe is derived from a Carib word. The 'blue' refers to blue-green streaks in the polished wood, giving it a distinctive appearance (Acevedo-Rodríguez and Strong, 2012; U.S. Department of Agriculture, 2013; Missouri Botanical Garden, 2013). In wetter areas it will grow in a wide range of elevations, up to 1,200 meters (3,900 ft.) and is often used in reforestation. It is the national tree of Jamaica (U.S Department of Agriculture, 2009).

It is an excellent wood with a rich variety of colors and attractive grain, but surprisingly, very little mahoe is currently being produced anywhere else. Mahoe can vary greatly in color from tree to tree; the blue tone does not tend to endure for many years. The wood transforms over time to shades of browns, purples, greys, and bluesy-greens (Tropic Ventures Rainforest Enrichment and Sustainable Forestry Project, 2009).

Since 2007, Areces and Fryxell renamed the Blue Mahoe (from Hibiscus elatus Sw. to Talipariti elatum Sw.) due to their arborescent behavior, prominent stipules that close the terminal yams, foliar lameness coriaceous, entire margin and a relative higher chromosomal number (2n = ca. 80, 90, ca. 92, ca. 96 and 120) (Fryxell, 2001). The same procedure was done with Hibiscus tiliaceus L (now Talipariti tiliaceum L.). Both species belongs to Malvaceae family.

The present study aimed at investigating the macromorphology, pharmacognostic evaluation and phytochemical screening of the wood of *T. elatum* Sw. towards standardization and monograph development and to evaluate the antibacterial activity of an ethanolic extract of this part of the tree.

FIG. 1. TREE, FLOWER, LEAF AND WOOD OF *TALIPARITI ELATUM* (SW.)

II.   MATERIAL AND METHODS

2.1   Plant Material

The wood was collected in January 2016 in the gardens of the Faculty of Pharmacy and Foods at Havana University, and identified at the herbarium of National Botany Garden of Havana, where the voucher specimen no. HAJB 82587 has been deposited. Specimen is registered as *Talipariti elatum* Sw. (Fryxell) Malvaceae (Sin. *Hibiscus elatus* Sw).

2.2   Chemicals

Analytical grade ethanol (Merck), analytical grade acetic acid (Merck), analytical grade n-butanol (Merck) and analytical grade methanol (Merck) were used in the analysis work. HPLC MeOH, Ultrapure MilliQ water and HPLC EtOH were purchase from BDH (Darmstadt, Germany). All solvents were degassing previously before used in an ultrasonic bath without filtration.

2.3   Extract and Samples Preparation

The wood was dried in an oven with controlled temperature, at 40°C, during 5 days. The extracts were prepared with the ground material (60 g) without screen extracted in a Soxhlet apparatus with 675 mL of ethanol at 95% during 20 hours. The ethanolic extracts were concentrated and evaporated under vacuum to 200 mL at 120 rpm, a temperature of 70°C and 500 mbar.

2.4   Phytochemical Studies

Dried wood was ground to a coarse powder (grain size: 850 ± 29 μm) and packed in a suitable container for phytochemical identification. The powder was extracted with 70% ethanol, filtered and concentrated using vacuum distillation.

The chemical constituents were screened according to Chhabra *et al*., 1989 to ascertain the presence of chemical components in diethyl ether, etanol and water. The UV spectrometric experiments were carried out on a UV-VIS JASCO V-530 (Japan). The scan range was 200 to 400 nm; absorbance 0.000-3.0000, band width 2.0 nm,spectral resolution 0.1 nm and the analyzed samples were diluted in methanol, into quartz cuvettes (d = 1 cm).

TLC conditions: TLCP (thin-layer chromatography plate) on silica gel with fluorescent indicator 254 nm on aluminum cards (layer thickness 0.2 mm) (10×20 cm) using n-butanol: acetic acid: water (BAW 65:25:10) as developing agent (v/v/v), concentrated sulfuric acid plus heat, $FeCl_3$and $AlCl_3$ were the chromogenic agents. Rutin (R), quercetin (Q) and gossypitrin (G) were used as standard. The TLCP were examined under ultraviolet (254 nm and 365 nm) and ordinary light.

The total ash, acid insoluble ash, water soluble ash, extractable matter and moisture content were determined according to the standard procedures mentioned in the general rule of WHO, 1998.

2.5   Procedures, Instrumentation and Parameters

Chromatographic profile of ethanolic extract at 70 % was carried out in an HPLC equipment Knauer-Azura (Germany) with UV detector at 280 nm, flow 1mL/min, with chromatographic column RP-18e (Knauer 250 x 4,6 mm Lichrospher 100-5), injecting 50,00 μL of the sample twice, during 60 min, pump pressure at 11,7 MPa, using as eluent (A) H_2O and eluent (B)

MeOH. A gradient of 15-85% B during 30 min at 1mL/min followed by holding the gradient, increasing up to 50 % A during 10 min and reversing to 0 % B during 5 min and equilibrating during 5 min.

2.6   Antibacterial Activity

2.6.1   Bacteria strains and procedures

For antimicrobial evaluation 4 strains of ATCC bacteria were used (*Bacillus cereus* 11778, *Staphylococcus aureus* 25923, *Salmonella tiphymurium*14028, *Escherichia coli* 25922), and were elaborated ethanolic extracts from the drug at 30, 50 and 70 % according of methodology propose by Rogger *et al*., 1990, and Biavati *et al*., 2008 with some modifications. The microorganisms were obtained from the Mycological Laboratory, BioCen, Bejucal, Mayabeque province, Cuba. The maximum concentration of the extracts employed to determine the MICs and MBCs was 250 mg/mL in base of extracts solubility. None antibiotic were used as inhibition positive control for the realized microbiological studies.

The microorganisms were replanted into Brain-heart infusion, incubated at 35 ± 2 ^{0}C during 18-24 hours. The antibacterial activity was also evaluated by the microdilution method (Hanel and Raether, 1988; Espinel-Ingroff, 2001). The bacterial suspensions were adjusted visually to a turbid standard 0.5 McFarland scale with sterile saline to a concentration of 2 x 10^6CFU/mL. The inoculate were prepared daily and stored at +4 °C until use. Dilutions of the inoculate were cultured on solid medium to verify the absence of contamination and to check the validity of the inoculum.

The sensibility test was realized from isolated strains adjusted with PBS up to reach a standard turbidity of 0.5 in McFarland scale, after that were inoculated by diffusion method in Muller-Hinton Agar.To evaluate extracts antibacterial activity, disc diffusion method was carried out using 6mm filter discs (Verpoorte, Beek, Thomassen, Aandewiel, & Svendsen, 1983). Bacteria were cultured overnight at 37°C in Tryptic Soy Broth (TSB) medium and then adjusted with sterile saline to a concentration of 1.0×10^5CFU/mL. The suspension was added to the top of the agar plates in Petri dishes (300 µL/agar plate) with Mueller-Hinton agar and suspended. Filter discs with extracts (10 µL/disc) were placed on agar plates. After 24 h of incubation at 37°C the diameter of the growth inhibition zones was measured (Sokovic, Glamoclija, Marin, Brkic, & Griensven, 2010).

2.6.2 Statistical analysis

Three specimens were used and all the assays were carried out in triplicate. The results are expressed as mean values and standard deviation (SD). The results were analyzed using one-way analysis of variance (ANOVA) followed by Tukey's HSD Test with α= 0.05. This treatment was carried out using SPSS v. 18.0 program.

III.   RESULTS AND DISCUSSION

3.1   Macroscopical and Microscopical Identification

The macroscopical morphology evaluation let define that wood is irregular, green-yellowish in color, 60 cm long and between 8-10 cm wide, characteristic odor and taste lightly astringent (Fig. 2)

FIG. 2. MACROSCOPICAL CHARACTERISTIC OF WOOD FROM *T. ELATUM*.

The powdered drug show green color with blue-greenish zones and kept its characteristics odor and taste (Fig. 3).

FIG. 3. PULVERIZED DRUG

The micromorphological evaluation of pulverized dry drug showed the presence of fiber with circular and longed cells which seems starch grains inside them with lenticular form (Fig. 4)
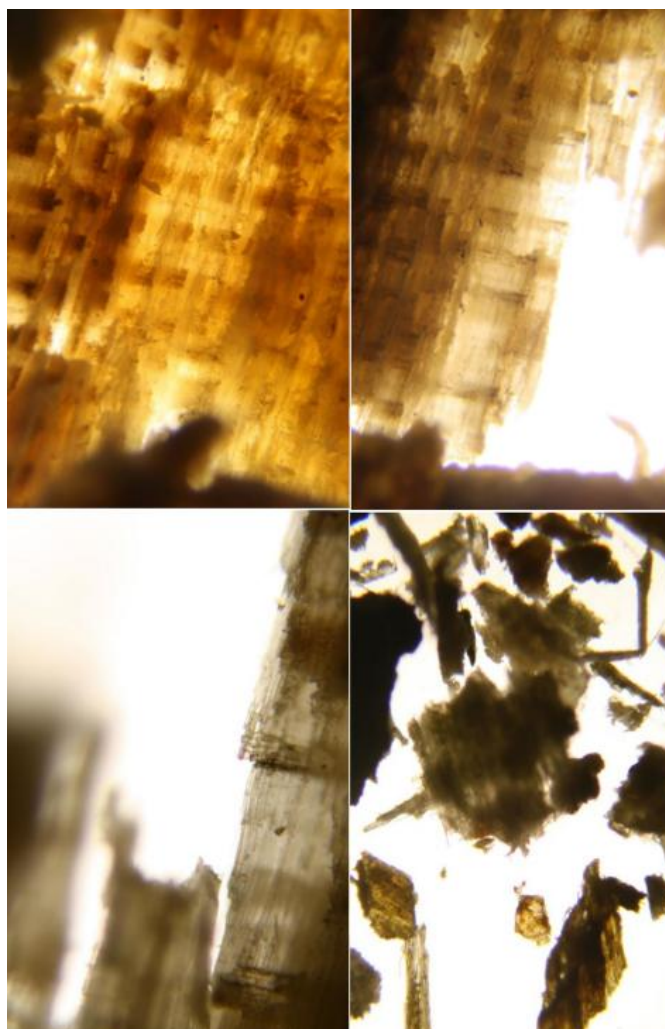

FIG. 4. MICROMORPHOLOGY OF PULVERIZED DRUG

3.2 Physicochemical Studies

3.2.1 Phytochemical Screening

Preliminary phytochemical screening showed the presence of at least 4 different chemical components in the extracts of the wood (Table 1). Phytochemical examination of the ethanolic extracts indicates the presence of tannins and/or phenolic

compounds, flavonoids, reductants sugars and triterpenes and steroids. Is obvious, at least preliminary, the absent of the rest of tested chemical compounds. A detailed information will be useful for the development of standardization parameters, isolation of phytoconstituents, screening of preclinical and clinical investigation, manufacturing of formulations and also distinguishing it from its closely related species.

TABLE 1
PHYTOCHEMICAL ANALYSIS OF WOOD OF *T. ELATUM* (SW.)

Test for constituent groups	Diethyl ether	Ethanol	Water
Dragendorff	-	-	-
Liebermann-Burchard	+	++	
Börntrager	-	-	
Baljet	-	-	
Sudan III	-		
Fehling		+	++
Shinoda		+	-
Kedde		-	
FeCl$_3$		-	+
Ninhydrin		-	
Foam		-	-
Bitter and astringent principles			Lightly astring.

3.2.2   Physicochemical Characteristics

The macroscopic and microscopic characters of any plant drug are considered to be the preliminary steps for establishing their quality control profile. As per the guidelines of WHO, pharmacognostical standards should be proposed as a protocol for the diagnosis and authentication of the herbal drugs (Pramanick, 2016).

An excess of water in medicinal plant materials will encourage microbial growth, the presence of fungi or insects, and deterioration following hydrolysis. Limits for water content should therefore be set for every given plant material. This is especially important for materials that absorb moisture easily or deteriorate quickly in the presence of water. Moisture content (7.6 %) was less than the limited index (8-14 %), indicating that the used dried method was highly efficient. Total ash (1.14 %), soluble ash in water (0.19 %) and acid insoluble ash (0.33 %) wereall lowerthan the official index accepted by the rules of WHO in 1998, which establishes that medicinal drugs must have those parameters around 3-5 % for total ash and less than 2 % for water soluble ash and acid insoluble ash, respectively.The value of extractable matter in ethanol was 10.87 %indicating that it is an appropriated solvent to realize the extraction of chemical constituents in this part of the plant.

3.2.3   Chromatographic analysis (TLC)

Chromatoplates analysis at ordinary light showed the presence of two spots yellow cream, the most closed to solvent front with an Rf of 0.90 and the second one 0.82. Long tile appear below but clearer ad a value of Rf of 0.75 almost at the same level of the spot that representing rutin as standard. Chromogenic reveal under UV$_{365 nm}$, showed that chromatoplates change in color, turning to purple, central spot darker. At UV$_{254 nm}$ the spots turn into bright blue, but central spot with high intensity.

Under ammoniac vapors all spots increased their color. Reveal with H$_2$SO$_4$ and heat the three same spots were observed again, darker both spots situated below the spot that appear near the solvent front. Chromogenic reveal with FeCl$_3$ showed that the spots were almost invisible, but the spot near solvent front acquired a greenish color indicating the presence of phenolic compounds relating with catecol.

Using AlCl$_3$ yellow color increased in spot situated below of the spot situated below solvent front could be related with chemical compounds like flavonoids. A change of color took place under UV$_{365 nm}$to dark purple and to bright purple underUV$_{254 nm}$ (Fig. 5).
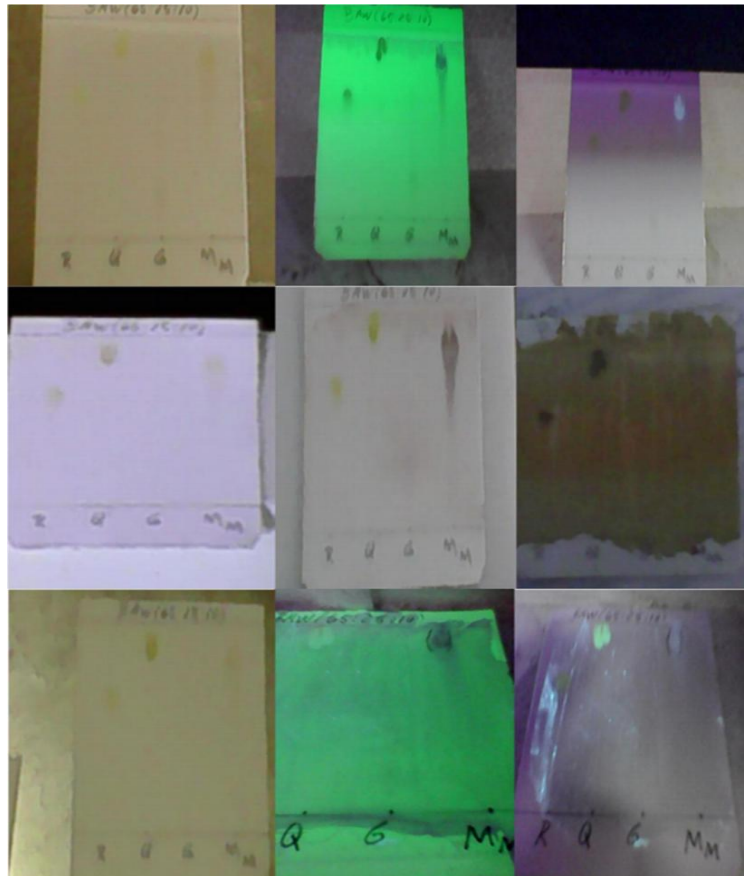
FIG. 5. CCD OF ETHANOLIC EXTRACT AT 70 % OF WOOD FROM *T. ELATUM*.
(Legend:Top left-ordinary light; top center-under UV$_{365}$ nm; top right-under UV $_{254}$ nm.
Center left-under ammoniac vapors; center middle-reveal with H$_2$SO$_4$;center left-reveal with FeCl$_3$.
Bottom left-reveal with AlCl$_3$; AlCl$_3$under UV$_{365}$ nm;AlCl$_3$ under UV$_{365}$ nm).

3.2.4   Chromatographic profile by HPLC

HPLC of ethanolic extract at 70 % of wood registered the presence of 44chromatographic peaks which is indicative that a great presence of chemical components into the extract, with retention times between 2.600 up to 48.250 min. The most important peaks belongs to compound 43 (45. 933 min) and 44 (48. 250 min), respectively (Fig. 6).

This solvent system showed good resolution of peaks within specific time and was finally selected as mobile phase system for analysis. The results allow infers that until now, the chemical constituents in this plant are included in the range of medium and high polarity.
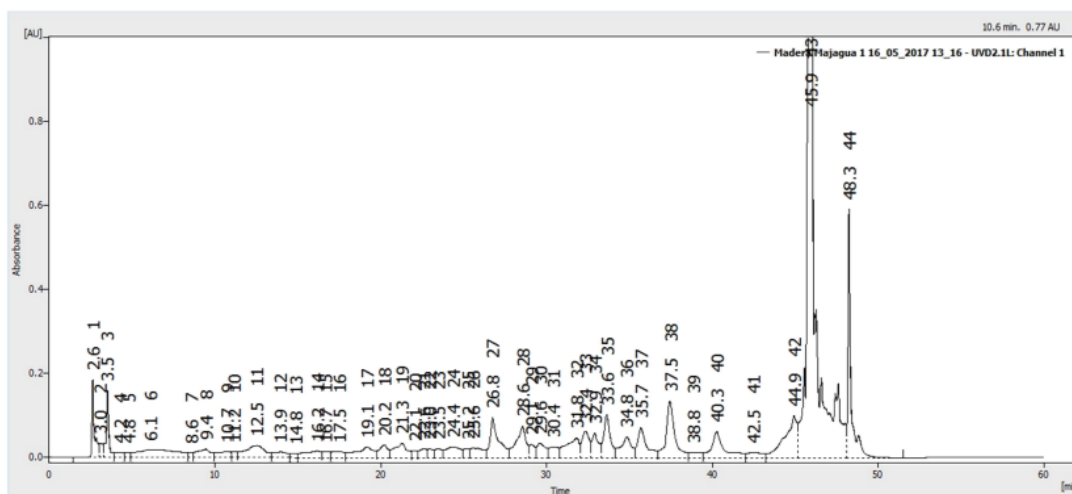

FIG. 6. CHROMATOGRAPHIC PROFILE OF ETHANOLIC EXTRACT AT 70 % OF WOOD FROM *T. ELATUM*.

3.2.5   Antibacterial activity

3.2.5.1   Determination of microbial charge using dilution method and deep culture

After microorganism accounting (36-72 h) was done the calculation of CFU/mL. The most interesting result was found in the plates at 10^{-6} and 10^{-7} with more than 300 colonies (3 000 000 CFU/mL), respectively (Fig. 7).
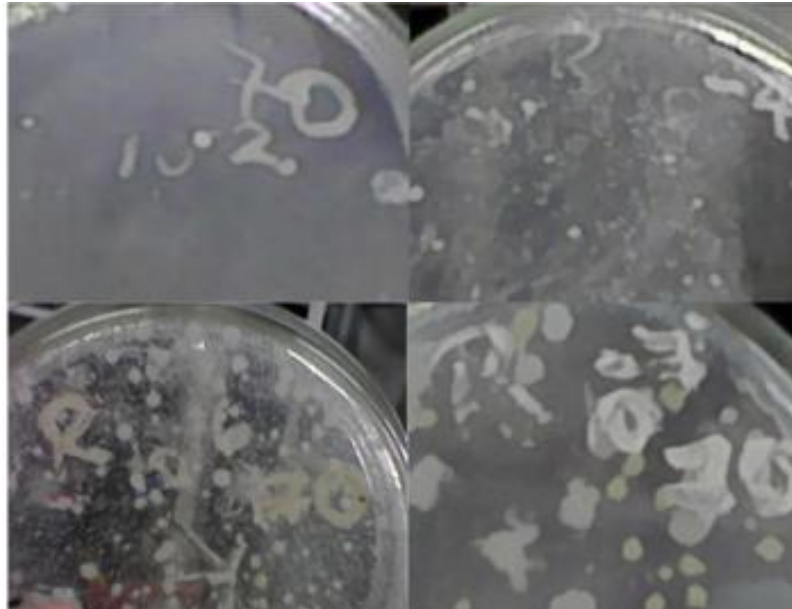

FIG. 7. CFU IN EXTRACT AT 70 % AFTER 24 HOURS

3.2.5.2   Colony selection to Gram tinction

After observation of microbial growth the selected plate was at 10^{-3} and we decided to isolate such colonies (the best and more defined). This isolation was done using the method of replanting by puncture (10^{-3}) or streak (10^{-5}) to observe the growing and procedure to realize the Gram tinction to define the morphology and cultural characteristics of microorganisms. Tinction were done by duplicate in both cases. Results are expressed in Table 2 and Figure 8.

TABLE 2
RESULTS OF COLONY SELECTION, CHARACTERISTICS AND GRAM TINCTION

Plates	Extract at 30 %	Extract at 50 %	Extract at 70 %
10^{-2}			Irregular, plane, undefined, white color Bacillus Gram +
10^{-3}	Circular, plane, entire, yellow color Tetracoccus Gram +		
10^{-4}		Irregular, plane, undefined, white color Bacillus Gram +	Circular, plane, entire, withe color Bacillus Gram +
10^{-5}	Circular, plane, entire, white color Staphylococcus Gram +	Irregular, plane, undefined, pale white color Bacillus Gram +	
10^{-6}		Irregular, plane, undefined, pale white color Bacillus Gram +	Irregular, plane, undefined, withe color Bacillus Gram +
10^{-7}		Irregular, plane, undefined, pale white color Staphylococcus Gram +	Irregular, plane, undefined, withe and yellow color Bacillus Gram +
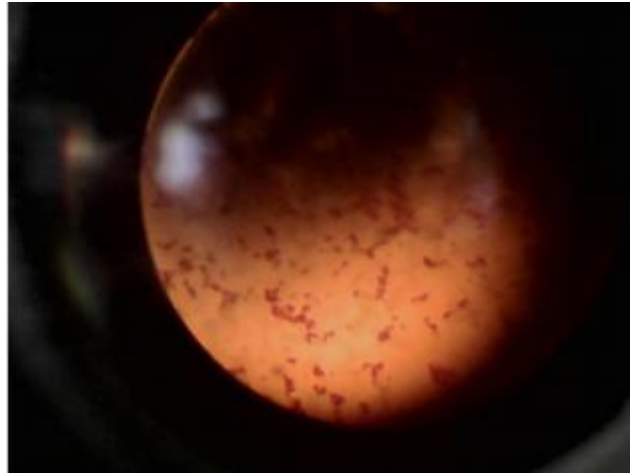
FIG.8. *STAPHYLOCOCCUS* GRAM +

3.2.5.3   Antimicrobial activity of ethanolic extracts

Extract at 30 % showed before 24 hours in Nutrient Agar solution inhibition zone (50 mm of diameter) of microorganism in front of *Salmonella tiphymurium*14028. In Muller-Hinton Agar was observed an inhibition zone of 30 mm in front of *Bacillus cereus* 11778(Fig. 9) using in both cases the disc inoculum at 10^{-3}.

FIG. 9. INHIBITION ZONE IN FRONT OF *BACILLUS CEREUS* 11778

Extract sample at 50 % after 24 hours of incubation in Nutrient Agar showed the presence of inhibition zone of 34 mm in *Bacillus cereus* 11778 and after 36 hours in *Escherichia coli* 25922 with the same measure of inhibition zone in inoculated disc at 10^{-1} and the full sample, respectively, because we propose that both strains are susceptive (Fig. 10).

FIG. 10. INHIBITION ZONE FOR BACILLUS CEREUS 11778 AND *ESCHERICHIA COLI* 25922.

Finally, ethanolic extract at 70 % after 24 hours in Nutrient Agar showed an inhibition zone of 54 mm in front of *Staphylococcus aureus* 25923 in inoculated disc at 10^{-2}, considering that the strain is susceptible. In the case of inoculated disc with pure sample was observed an inhibition zone of 15 mm in front of *Bacillus cereus* 11778, suggesting that this strain of bacteria is medium susceptible or resistant (Fig. 11).
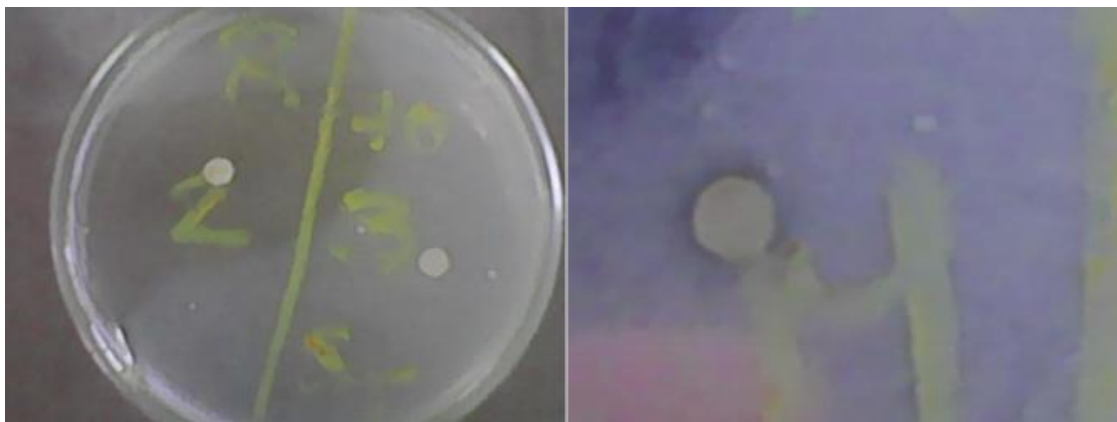

FIG. 11. INHIBITION ZONES IN *STAPHYLOCOCCUS AUREUS* 25923 AND *BACILLUS CEREUS* 11778.

In Muller-Hinton Agar was observed an inhibition zone of 18 mm in front of *Staphylococcus aureus* 25923 and 16 mm in front of *Bacillus cereus* 11778 using pure sample, suggesting that both strains are medium susceptible or resistant (Fig. 12).
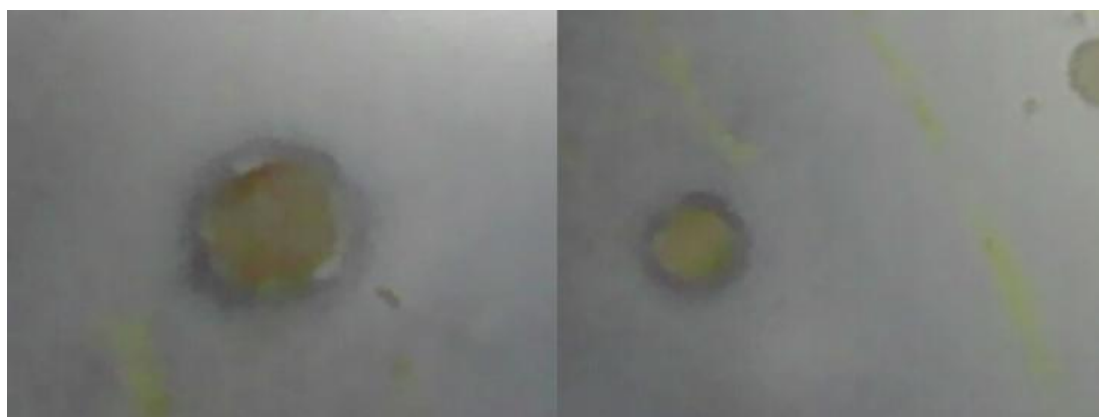

FIG. 12. INHIBITION ZONES IN *STAPHYLOCOCCUS AUREUS* 25923 AND *BACILLUS CEREUS* 11778.

IV.　CONCLUSION

Physicochemical values are all according with the parameters established by the WHO being in all cases below the describe values for vegetable drug, suggesting that the wood of *Talipariti elatum*(Sw.) can be used to elaborate a phytomedication without the risk of suffer any inconvenient for our health. The chemical compounds present in the ethanolic extracts lead to think that they are chemical metabolites useful to improve medical conditions related with oxidative stress and antidiarrheal illness. Chromatographic profile showed the high presence of chemical constituents in elaborated extracts with ethanol at 70 %. The analyzed ethanolic extracts at 50 and 70 % suggested that CFU belongs to Tetracoccus and Staphylococcus Gram + and Streptobacillus Gram +. Extracts at 30, 50 and 70 % showed antibacterial activity in front of four strains used in the research (*Salmonella tiphymurium* 14028, *Bacillus cereus* 11778, *Escherichia coli* 25922 y *Staphylococcus aureus* 25923) indicating good possibilities to use those extracts to combat bacterial infections in humans and animals.

Efforts have been made by the authors to bring out every detail on the macroscopical characters of the leaves of this medicinal plant. The study of pharmacognostical features had shown the standards, which will be useful for the detection of its identity and authenticity. It provides reference basis for formulating quality standard of *T. elatum*authenticity of medicinal plants and resource utilization.

CONFLICT OF INTEREST STATEMENT

We declare that we have no conflict of interest.

REFERENCES

[1] Acevedo- Rodríguez P and Strong MT. (2013). Catalogue of Seed Plants of the West Indies. Smithsonian Contributions to Botany, number 98. p. 507-508.

[2] Areces F y Fryxell PA. (2007). Flora de la República de Cuba. Fascículo 13. Malvaceae. p. 5-6.

[3] Chhabra, Sc., Uiso, F.C. and Mshin, E.N. (1989). Phytochemical Screening of Tanzanian Medical Plants. I. Journal of Ethnopharmacology, 11, 157-179.

[4] Espinel-Ingroff, A. (2001). Comparation of the E-test with the NCCLS M38-P method for antifungal susceptibility testing of common and emerging pathogenic filamentous fungi. Journal of Clinical Microbiology, 39, 1360-1367.

[5] Fryxell, P. A. (2001). *Talipariti* (*Malvaceae*), a segregate from *Hibiscus*.-Contr. Univ. Michigan Herb. 23: 225-270.

[6] Germplasm Resources Information Network. (2009). United States Department of Agriculture."*Talipariti elatum*". Retrieved 2009-01-27.

[7] Hanel, H., & Raether, W. (1988). A more sophisticated method of determining the ofwater-insoluble preparations with a cell harvester, using miconazole as an example. Mycoses, 31, 148-154.

[8] Sokovic, M., Glamoclija, J., Marin, P. D., Brkic, D., & van Griensven, L. J. (2010). Antibacterial effects of the essential oils of commonly consumed medicinal herbs using an in vitro model. Molecules, 15, 7532-7546.

[9] Tropic Ventures Rainforest Enrichment and Sustainable Forestry Project. (2009). "Eye on the Forest".Retrieved 2009-01-27.

[10] Tropicos.org. Missouri Botanical Garden. (2013)."*Talipariti elatum* (Sw.) Fryxell".Retrieved 6 September 2013.

[11] U. S. Department of Agriculture. (2013). *Hibiscus elatus* Sw. "mahoe". Natural Resources Conservation Service. Plants Database. Retrieved 6 September 2013.

[12] WHO (1998). Quality Control Methods for Medicinal Plant Materials. Typeset in Hong Kong Printed in England 95/10628-Bestset/Clays-6000.

Ignition Behavior of Al/Fe₂O₃ Metastable Intermolecular Composites

S K Sahoo[1*], S M. Danali[2], P. R. Arya[3]

High Energy Materials Research Laboratory, Pune-411021, INDIA

Abstract— *Nano size Al/Fe₂O₃ thermite system has been reported in the literature as metastable intermolecular composites (MIC). Nano Al/nano Fe₂O₃ MIC has been prepared in various proportions by ultrasonic method. A comparative study on heat output and thermal behavior has been made on MIC using DTA (Differential Thermal Analysis), STA (Simultaneous Thermal Analyzer) and bomb calorimeter. It has been observed that nano-size ingredients produce more heat output compared to micron size ingredients. The ignition temperature also reduces in case of MIC indicating faster release of energy at lower temperature. The impact of ignition of nano-thermite has been reported based on ignition DTA experiment. DTA analysis also shows complete reaction in case of MIC where as micron size thermite showed an endothermic peak of Al melting indicating incomplete reaction. The PXRD (Powder X-Ray Diffraction) data of combustion products has been used to establish the combustion mechanism of MIC. The activation energy of MIC has been calculated using Kissinger, Ozawa and Starink kinetic equations and compared with literature reported values.*

Keywords— *MIC, combustion kinetics, heat output, STA, DTA.*

Abbreviations used

ΔH= heat of combustion (cal/g)

E_a= activation energy (kJ/mol)

T_m= maximum peak temperature of DTA (K)

α = heating rate (K/min)

M= slope of the linear line

C_1 = intercept of the linear line and constant of Kissinger equation

C_2= intercept of the linear line and constant of Ozawa equation

Z_1 and Z_2 = pre–exponential factor (frequency factor)

R= universal gas constant (8.314 J/K mol)

I.   INTRODUCTION

The thermite systems give very high-temperature output and are prefered as heat source for several applications. The Al/Fe₂O₃ thermite system is a classical thermite system and can be used for welding of railway tracks (since 1898), cutting and perforation of materials, to produce alumina liners *insitu* for pipes, a portable heat source, a high-temperature igniter, a pyrotechnic heat producer as an additive to explosives [1] propellants [2], gas generating compositions [3], nanoenergetic microelectromechanical systems (MEMS) platform for micro-propulsion system [4] and incendiary grenade [5]. This system has also been investigated in environmental protection processes [6], namely for the treatment and recycling of zinc hydrometallurgical wastes [7, 8] and for the treatment of by-products of steel industry [9]. Other recent applications of this reactive system are the synthesis of ceramic reinforced metal–matrix composites [10, 11], of magnetic granular films [12], of iron aluminides [13-15], of transition metal carbide/ nitrides [16], alloying/welding [17] and energetic nanocomposites [18-20]. Al/Fe2O3 has been used for catalytic application of combustion of AP/HTPB system [21]. Recently fabrication of hybrid nano-composite from Al/Fe2O3 system has been reported in the literature [22].

Recent developments in the preparation and production of nanomaterials have created a new kind of energetic materials commonly known as nanoscale composite energetic materials, metastable intermolecular composites (MIC) or simply

nanoenergetics. MIC's are also known as superthermites. In these materials, nanosized particles of ingredients are used to produce dramatic changes in combustion behavior. Nanosized metals and metal oxides in the MICs have replaced the micron sized constituents which are used in conventional thermites. The reduction of particle size with increased surface area effectively enhances homogeneity of the mixture [23]. This change in particle size produces significant changes in the kinetics and reaction propagation characteristics of the thermite. Generally, nano-particles on approaching towards molecular size and intermixing at this level increase the characteristics of the thermite over micron size thermite mixtures [24, 25]. It is considered that ignition is generally a melting of one of the two components followed by a diffusion-controlled reaction. The melting point of aluminum is 660 °C whereas Fe_2O_3 begins to melt at 1565 °C. Nano-scale particles have been considered highly reactive and melting point independent wherein the solid-solid physical contact may be sufficient for ignition [26].

A number of studies have been carried out on Al/Fe_2O_3 thermite for its reaction mechanism and kinetics. Sarangi et al [27] investigated this system using different Al percent and studied its reaction kinetics. Duraes et al [28] studied the reaction intermediate and final product characterization of Al/Fe_2O_3 system taking various molar ratio of both the constituents. Mei et al [29] made an interesting investigation for the kinetics and combustion mechanism of the reaction as given in Eq. 1 below. Fan et al also studied the kinetics and combustion mechanism of the thermite reaction [30]. Bullian et al [31] investigated the reaction kinetics of 38.6% Al and 61.4% Fe_2O_3 thermite system. Weiser et al [32] investigated ignition of different stoichiometric proportion of Al/Fe_2O_3 system for their product under pressure. Cheng et al [33] studied the kinetics of thermally initiated reaction of Al/Fe_2O_3 nanothermite. Wang et al reported Al/Fe_2O_3 thermite reaction mechanism based on residue collected from DSC experiments at different temperature [34]. In this paper we have reported the reaction mechanism based on combustion product analysis obtained from bomb calorimeter experiments for different thermites.

Heat of reaction of the thermite system described by Eq. 1 is sufficient to raise its temperature to very high values (~3000 K), above the melting points or even the boiling points of reactants, intermediate and final products for the following reaction:

$$Fe_2O_3 + 2Al \rightarrow 2Fe + Al_2O_3 + \Delta H \tag{1}$$

However, the ignition behavior of MIC's based on nano Al and nano Fe_2O_3 has not been reported yet in the literature. An attempt has been made to study the ignition behavior of MIC using DTA, STA and bomb calorimeter. The PXRD has been used to study thermite reaction mechanism by the combustion product analysis.

II.   EXPERIMENTAL

Nano sized α-Fe_2O_3 (70nm) was prepared through emulsion route as described in literature [35]. Nano Al (100nm) was obtained from SIBTERMOCHIM Ltd, Russia. Other chemicals used for this work were: micron size (1.6 μ) α-Fe_2O_3 (Cyanide & Pigment Ltd, Kolkota, India), and cyclohexane (Thomas Baker, India). The scheme for preparation of thermite is described in Fig.1. Nano Al and Fe_2O_3 powder were mixed thoroughly with various weight ratio as given in Table-1. A composition was prepared by adding 5g dry mix of nano Fe_2O_3 and Al into 100ml cyclohaxane. The contents were ultrasonicated for 20 min. to break the agglomerates. The contents were then poured into a watch glass and slightly heated to allow evaporation of cyclohexane.

TABLE-1
COMPOSITION DETAIL.

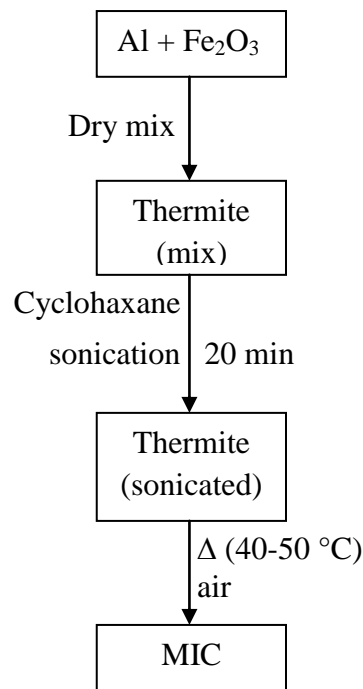| Composition Code	Al (100nm) %	Fe_2O_3 (70nm) %	Fe_2O_3 (1.6 μ) %
T1	25	-	75
T2	15	85	-
T3	25	75	-
T4	35	65	-

* Batch size = 5 g

FIG. 1. SCHEME FOR MIC PREPARATION

Heat output (calorimetric value) of the MICs was measured using LECO AC-350 Bomb Calorimeter (USA make) in argon medium at a pressure of 5 atm. Ignition temperature was measured using a DTA instrument (Stanton Redcroft, UK make) at a heating rate of 40 °C/min at ambient condition. For kinetic study, thermal analysis experiments were carried out at different heating rates of 20, 30 and 40 °C/min. Simultaneous thermal analysis (STA) experiments were carried out by purging nitrogen at a flow rate of 100 mL/h using TA instruments (model SDTQ600 of USA make). Powder X-ray diffraction (X'Pert pro, Panalytical, The Netherland) studies of the combustion products (residue obtained from bomb calorimeter experiments) were carried out using Cu Kα radiation of wave length 1.5405Å.

III.   RESULTS AND DISCUSSION

3.1   Heat output

The heat output values of MIC obtained from bomb calorimeter experiment have been given in Table-2. The value for MIC of 25:75 ratio of Al/Fe_2O_3 (T3) was 665 cal/g. The thermite composition with same percentage of Al & Fe_2O_3 (T1) produced 515 cal/g heat output. This indicated that MICs provided efficient combustion compared to thermite. The heat output value with 35% aluminium increased to 689 cal/g and with 15% Al heat output decreased to 210 cal/g. The decreasing trend in heat output result with decreasing fuel percentage has also been reported in literature [36]. The variation in heat output result in all the MIC was due to incomplete reaction which could be due to non availability of adequate oxidizer or fuel in the composition. According to Eq. 1, for the stoichiometric reaction, 25:75 weight ratio is required for Al/Fe_2O_3 thermite system. According to the result reported by Sarangi et al, [27] a complete reaction takes place for Al/Fe_2O_3 thermite system for the ratio of 8:1. Bullian et al [31] studied Al/Fe_2O_3 thermite system with ratio of 38.6: 61.4.

TABLE-2
CALORIMETRIC VALUES OF THERMITE COMPOSITIONS.

Composition	T1	T2	T3	T4
Cal val (cal/g)	515	210	665	689

3.2   Ignition of thermite and MIC using DTA

The ignition behavior of T1 and T3 mixture was measured with the help of DTA at a heating rate of 40 °C/min (Fig. 2). In case of thermite mixture T1 (micron size Fe_2O_3), a very smooth and broad exothermic peak at 615 °C was observed. Whereas a strong and sharp ignition peak at 605 °C could be seen for the MIC T3 (with nano Fe_2O_3). However, T4 mixture showed similar ignition behavior. The DTA data indicated that T3 and T4 mixture provided faster heat release as compared to thermite mixture T1.

Sarangi et al [27] reported that the reduction reaction in air always took place at 890 °C and could not be ignited in inert atmosphere. Mei et al [27] has mentioned that the combustion reaction takes place in two stages, Fe_2O_3 first completely decomposes to Fe_3O_4 and O_2 at 960 °C, and then Al reacts with Fe_3O_4 to produce Al_2O_3 at 1060 °C. Wang et al [37] reported that first exothermic peak appears at 853 °C at a heating rate of 10 °C. They also observed an endothermic peak near 660 °C for the melting point of Al. Cheng et al [33] reported the ignition temperature of different Al/Fe_2O_3 nano thermite system in the range of 686-1036 °C.
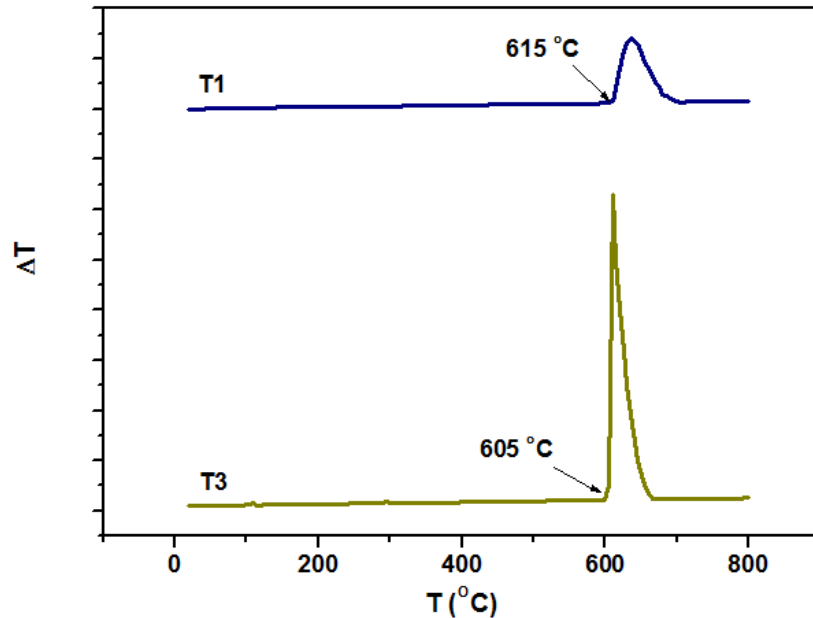
FIG. 2. DTA GRAPH AT 40 °C/MIN FOR MIC.

However, it has been observed the ignition behavior of MIC T3 with a strong and sharp exotherm at 605 °C (Fig. 2), which is lower than the earlier reported values. The alumina crucibles after the DTA experiments are shown in this Fig. 3. The crucible remained intact after experiment in case of sample T1 (Fig. 3a and 3b). However, it has been observed that crucibles were broken after experiments (Fig. 3c and 3d). The vigorous exothermic reaction for nano sized MIC seems to be of high impact with much faster release of heat energy. Due to this very high impact upon ignition the crucible got broken.
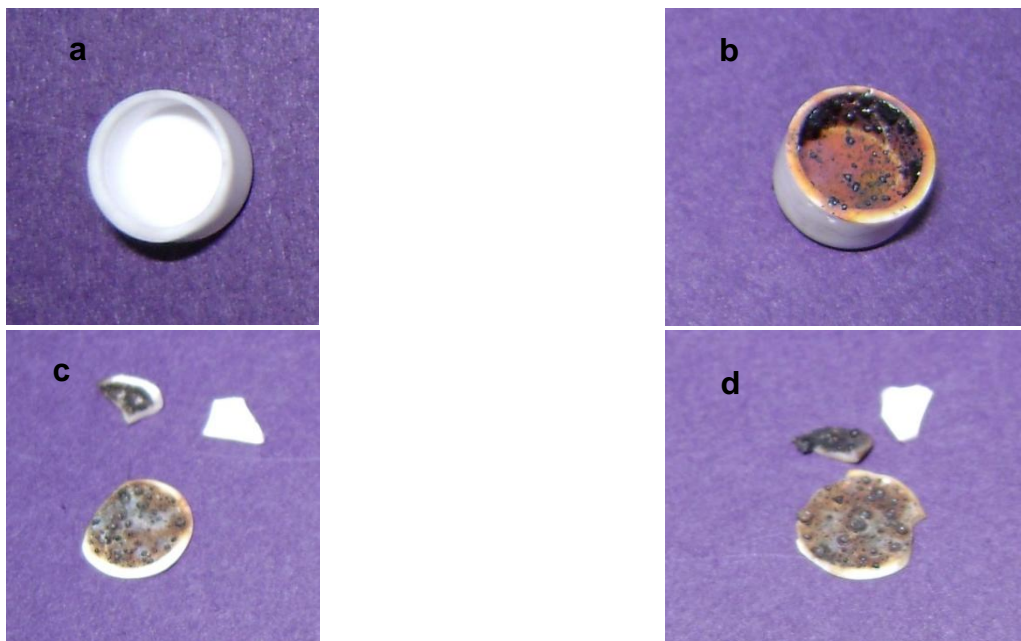
FIG. 3. CRUCIBLES USED BEFORE (A) AND AFTER DTA EXPERIMENTS. (B) FOR THERMITE T1AND (C) AND (D) FOR MIC T3.

In the present study, no any endothermic peak was observed in MIC and thermite composition. However, a sharp exothermic peak was obtained at nearly 605 °C before ignition. It may be due to the melting of nano Al. Soon after melting, reaction of nano Al with nano Fe_2O_3 continues followed by fast combustion reaction. Due to nano-sized particles, the distance between fuel and oxidizer particles is reduced. The sharper ignition peak of MIC than for micron size thermite (T1) may be understood based on the explanation given by Plantier [26]. Thermite reactions are diffusion controlled and hence decrease in the diffusion distance causes reduction in ignition time and increased reaction rate of the mixture. Because of the contact distance of both the constituents (fuel and oxidizer) is reduced almost to the molecular dimension, these reactions are capable of producing higher rates of energy release and resulting in enhanced reactivity [38-40]

3.3   Thermogravimetric and Differential Thermal Analysis

STA measurements were carried out at a heating rate of 20 °C/min (Fig. 4 and Fig. 5). The details of STA results have been given in Table-3. DSC curve showed the exothermic peak between 616-621 °C for all the three samples (T1, T3 and T4). The peak intensity/area under the curve was found maximum in case of T4 as compared to T1 and T3. The peak area under the curve is proportional to enthalpy change (ΔH) of the material. Hence from the graph and Table-3, the values of ΔH was higher in case of T4 (906 J/g) and T3 (821 J/g) as compared to T1 (597 J/g). Along with exothermic peak, there was an endothermic peak at 654 °C in the DSC curve of T1, which was due to the melting of unreacted Al remained after ignition. This peak was not observed in case of T3 and T4. XRD data confirmed that No unreacted residual Al was left in case of T3 and T4.

The TGA experiment was carried out at a heating rate of 20 °C/min. Continuous weight gain was observed at a true onset temperature of 550 °C (Fig. 5a). Similar behavior has been reported for nano Alex by Jones et al. [41]. They have explained that the weight gain is due to nitridation on the surface of nano Al or of the un-reacted Al core [42] which is described as follows (Eq. 2)

$$2Al(s) + N_2 (g) = 2AlN(s) \tag{2}$$
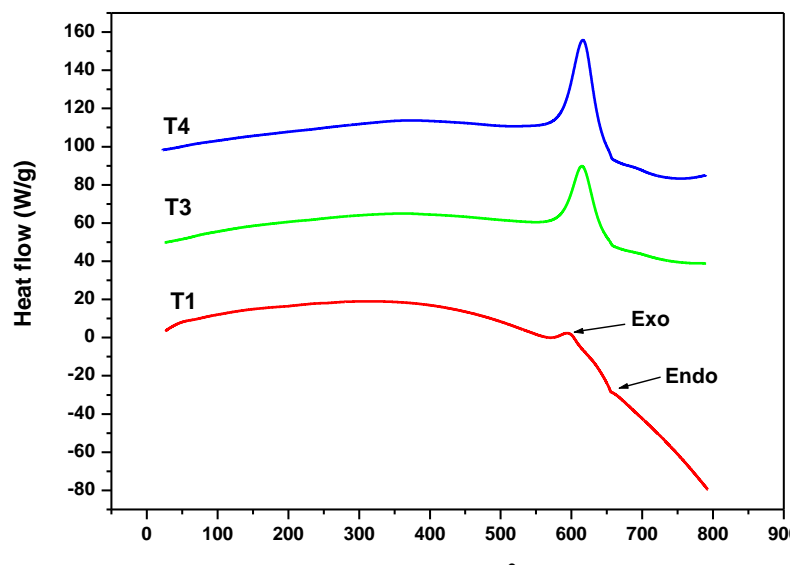

FIG. 4. DSC CURVES FOR MIC T1, T3 AND T4 AT A HEATING RATE OF 20 °C/min. INSERT IS THE ENLARGEMENT OF ENDOTHERMIC PEAK FOR T1

TABLE-3
DATA OBTAINED FROM STA ANALYSIS.

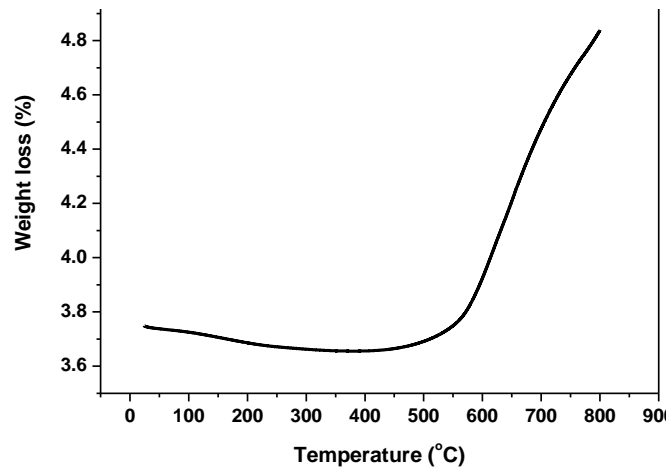| Sample	DSC peak position (°C)	ΔH (J/g)	Wt. gain (%)
T1	621 ↑ 654 ↓	597	4.01
T3	616 ↑	821	4.71
T4	620 ↑	906	8.53

↑- exo, ↓-endo

FIG. 5. (A) TG PLOTS FOR NANO AL AT A HEATING RATE OF 20 °C/MIN.
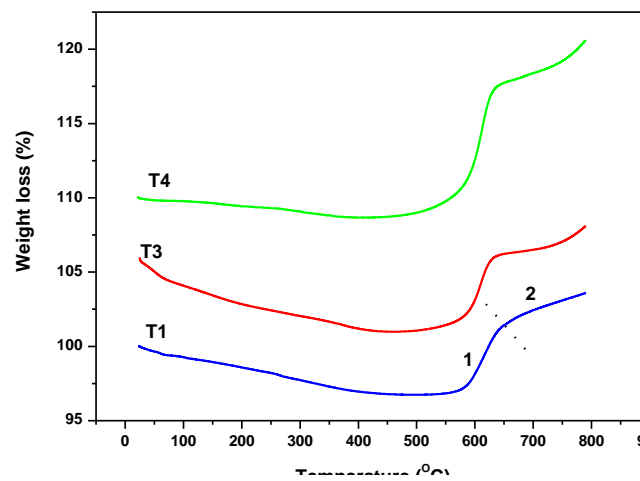
FIG. 5. (B) TG PLOTS FOR T1, T3 AND T4 AT A HEATING RATE OF 20 °C/MIN

Nitridation leads to exotherm in DTA graph. But due to lower peak temperature and higher heating rate it did not appear on corresponding DTA graph. The DTA peak at around 660 °C was due to melting of un-reacted core Al. In TG graph of MIC T1, T3 and T4 (Fig. 5b) weight gain was observed in two steps for sample T1. Step 1 (weight gain =4.01%) was due to nitridation along with thermite reaction and step 2 was due to melting of un-reacted Al. In case of T3 and T4 sharp weight gain was observed. This is due to the much faster ignition reaction of nano size MIC than micron size. This result is in agreement with DSC and ignition DTA peaks. More weight gain, observed in case of T4 (8.53%) as compared to T3 (4.71%), was due to the presence of more amount of Al undergone nitridation.

3.4   Combustion Kinetics

Based on DTA plot at a heating rate of 20, 30 and 40 °C/min, kinetics of the combustion parameters were studied. Three different methods have been applied for the calculation of activation energy (E_a) for comparison. Those are (a) Kissinger method, (b) Ozawa method and (c) Starink method.

3.4.1   Kissinger Method

According to Kissinger "during the rise in temperature the reaction passes by a maximum before decreasing"[43]. It is based on the equation below

$$\ln\left(\frac{\alpha}{T_m^2}\right) = -\frac{E_a}{RT} + C_1 \tag{3}$$

$$C_1 = \ln\left(\frac{E_a}{RZ_1}\right) \tag{4}$$

The plot of $1000/T_m$ and $ln(\alpha/T_m^2)$ gives a straight line (Fig. 6) and from the slope M activation energy can be calculated as

$$E_a = -RM \tag{5}$$
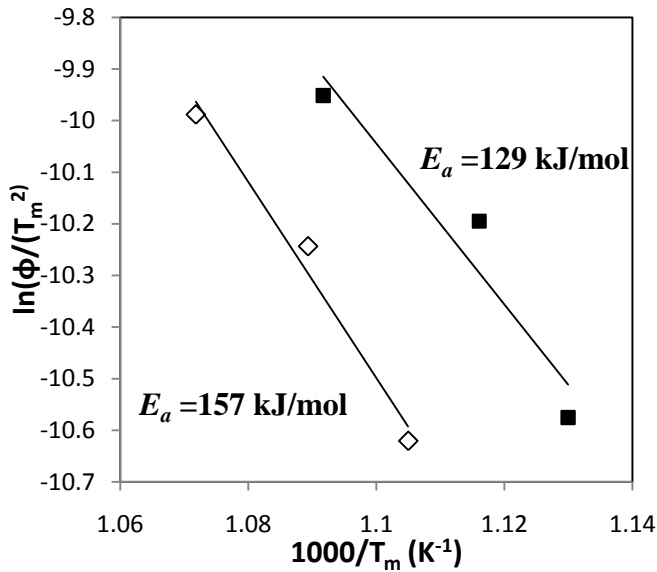
FIG. 6. PLOT OF $1000/T_m$ and $ln(\alpha/T_m^2)$ USING KISSINGER'S METHOD
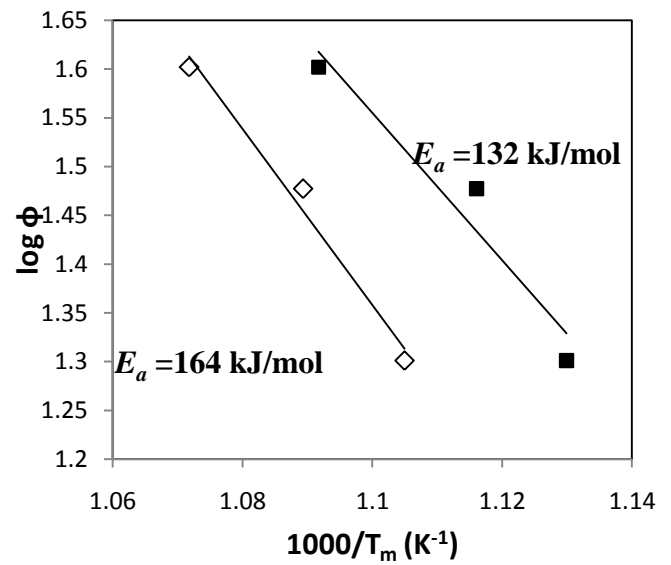
FIG. 7. PLOT OF $1000/T_m$ and log α USING OZAWA'S METHOD

3.4.2   Ozawa Method

Ozawa proposed the following kinetic equation for the determination of activation energy [44]

$$ln\alpha = -\frac{E_a}{RT} + C_2 \tag{6}$$

The plot of $1000/T_m$ and log α gives a straight line (Fig. 7) and from the slope M activation energy can be calculated as

$$E_a = -2.19R.M \tag{7}$$

3.4.3   Starink Method

A new method for the derivation of activation energies is proposed by Starink [45]. According to him

$$ln\left(\frac{T_m^{1.8}}{\alpha}\right) = Z_2\frac{E_a}{RT_m} + C_3 \tag{8}$$

$$Z_2 = 1.0070 - 1.2 \times 10^{-5} E_a \tag{9}$$
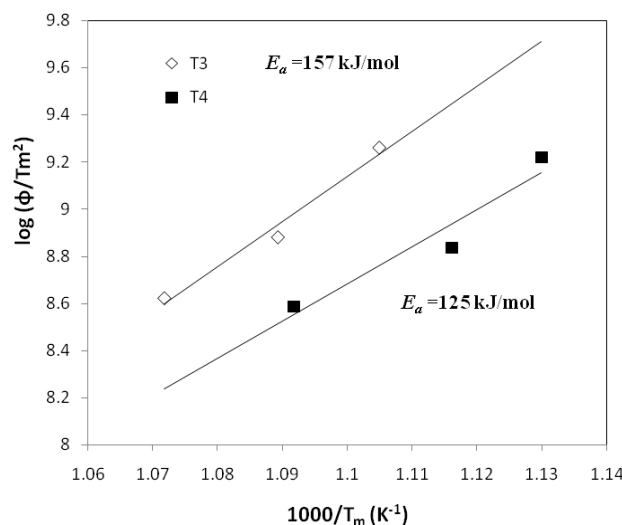
FIG. 8. PLOT OF $1000/T_m$ and $ln(T_m^{1.8}/\alpha)$ USING STARINK METHOD

The plot of $1000/T_m$ and $\ln(T_m^{1.8}/\alpha)$ produces a straight line (Fig. 8). From the slope M and A, activation energy can be calculated as

$$E_a = \frac{RM}{A} \qquad\qquad (10)$$

TABLE-4

ACTIVATION ENERGY (E_a) of MIC in kJ/mol.

MIC	Kissinger method	Ozawa method	Starink method
T3	157	164	157
T4	129	132	125
Ref 28	-	-	145
Ref 29	-	248	-

Activation energies estimated by Kissinger, Ozawa and Starink methods are tabulated in Table-4. E_a is found to be 157, 164 and 158 kJ/mol for MIC T3 and that of 129, 132 and 126 kJ/mol for MIC T4 respectively. Fan et al [28]reported that the value of E_a by Starink method was 145 kJ/mol for the thermite reaction. Bulian et al [31].found the nearest value of 247.76 kJ/mol for the similar nano thermite reaction applying Ozawa method.

3.5 Combustion Mechanism

The thermite compositions and the products obtained after heat of combustion experiments of the compositions were analyzed by powder XRD. The XRD patterns of compositions and the combustion products have been shown in Fig. 9 and 10. The phases present in the products after combustion have been presented in Table-5. The corresponding Miller planes have been shown against their peaks of both Al and α -Fe_2O_3.

In case of thermite (T1), as shown in Fig. 10, the products obtained were cubic-Al_2O_3, cubic-Fe and cubic-Fe_3Al. The later one Fe_3Al, an intermetallic phase, was detected with higher intensity in the products of sample. The intermetallic phase peak coincided with Fe phase. As from DSC graph (Fig-4), the presence of Fe_3Al phase was confirmed by the observation of endothermic peak for Al melting. In case of MIC's T2 and T3, hercynite (cubic-Al_2FeO_4 which is $Fe+2Al_2O_4$) was widely identified as an intermediate product of the thermite reaction [24]. In case of T2, other than hercynite, cubic-FeO phase was found. Along with hercynite, rhombohedral-α-Al_2O_3 and cubic-Fe phases were found in MIC T3. Formation of Fe phase in this case may be due to reduction of FeO to Fe. Fig-10 revealed the presence of rhombohedral α-Al_2O_3 phase along with low intensity peak of cubic-Fe for the combustion of T4. No other products were found is in this case.

TABLE-5

FINAL COMBUSTION PRODUCT OF MICs (BASED ON XRD ANALYSIS).

Composition	Products
T1	Al_2O_3, Fe, Fe_3Al
T2	Al_2FeO_4(i.e. $Fe+2Al_2O_4$), FeO
T3	Al_2O_3, Fe, Al_2FeO_4
T4	Al_2O_3, Fe
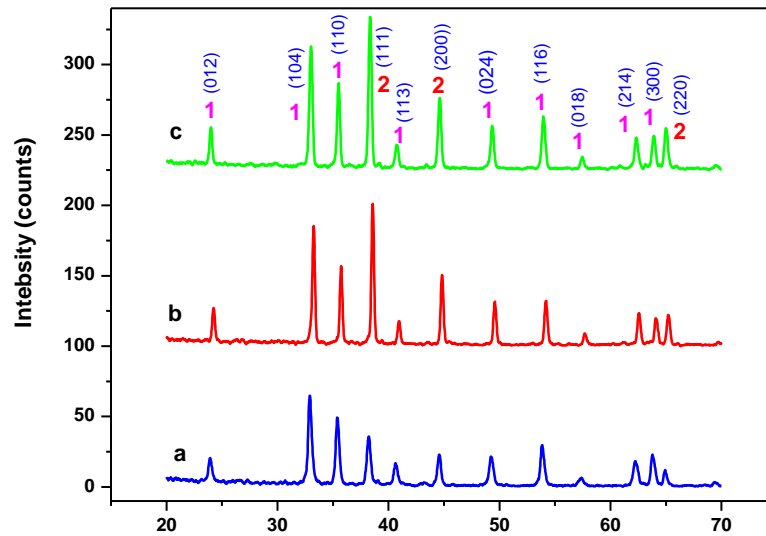
FIG. 9. XRD PATTERNS MICS (a) T1, (b) T3 and (c) T4. THE PHASES INDICATED IN THE PATTERNS ARE 1-Fe$_2$O$_3$ (Rhombohedral), 2-Al (Cubic) WITH THEIR CORRESPONDING PLANES.

The probable mechanism for the micron size thermite reaction (for T1) can be discussed on the basis of the above results and literature review. Fe–Al intermetallic phases produce when Fe phase obtained product is in contact with melted aluminum [11, 13-14]. Due to the presence of nano Al, the reaction proceeds in case of T1 as nitridation followed by melting of Al and then reaction with Fe$_2$O$_3$ to form Al$_2$O$_3$ and FeAl$_3$. Micron size iron oxide could not get reduced completely, But in case of MIC's, a violent reaction (also recognized by DTA) occurs among the nano reactants as the ignition point reached and energy release is much faster than thermite. In case of T2, excess of oxidizer turned out to FeO. Sample T3 showed intermediate product hercynite. Similar products have been reported in the literature also [34]. The difference in reaction mechanism for thermite and MICs can be explained as reduction of thermite fuel and oxidizer particle size from the micron regime to nano-scale dimensions has been shown to produce more favorable combustion behavior. Such fine-sized particles make greater intermixing and reduced diffusion distance between fuel and oxidizer. As discussed earlier, because of diffusion controlled molecular level reactions, decrease in the contact distance among the fuel and oxidizer could decrease ignition time and higher energy release rate.
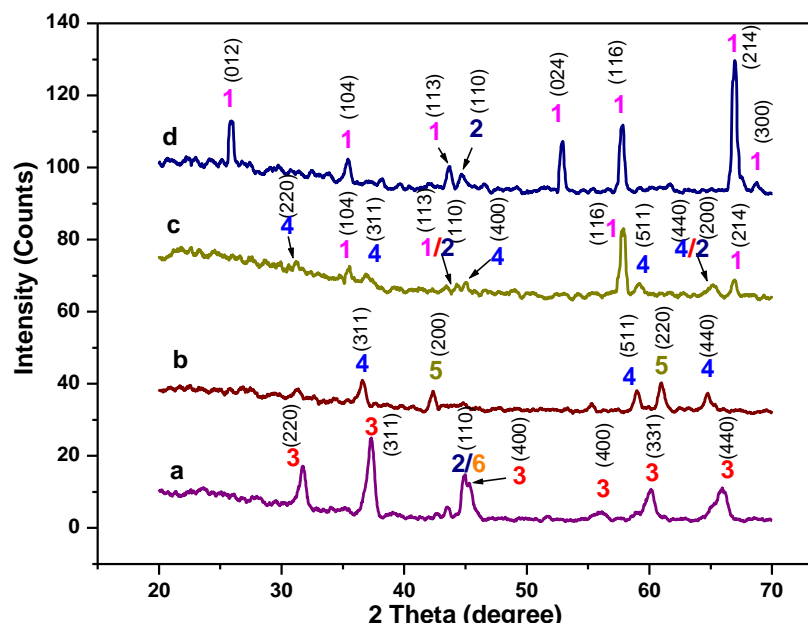

FIG. 10. XRD PATTERNS FOR COMBUSTION PRODUCTS OF (a) T1, (b)T2, (c) T3 and (d) T4 THE PHASES INDICATED IN THE PATTERNS ARE 1-Al$_2$O$_3$ (Rhombohedral), 2-Fe (Cubic), 3-Al$_2$O$_3$ (Cubic), 4-Al$_2$FeO$_4$ (Cubic i.e. Fe+2Al$_2$O$_4$) 5-FeO (Cubic), 6-Fe$_3$Al (Cubic)

IV.   CONCLUSION

Nano thermite compositions (MICs) were prepared by ultrasonic method using nano Al and nano iron oxide of different weight percentage which were found to be more efficient than micron size thermite composition. Heat of combustion obtained by bomb calorimeter increased upon increasing Al content. Ignition temperature measured by DTA of MICs was lower than micron size thermite composition and combustion reaction was very fast with faster release of thermal energy. In the thermo-gravimetric analysis, two transitions were observed, one for nittridation ignitation with exo followed by melting of Al with endo peak for thermite. MIC showed only one nitridation ignitation with exo peak. The activation energy was calculated using Kissinger, Ozawa and Starink kinetic equation and found to be 164, 157 and 158 kJ/mol. MIC's are more efficient in energy release than micron size thermite composition. The mechanism of the combustion reaction was investigated by XRD of combustion products. Micron size thermite composition produced byproducts such as Al_2O_3 and $FeAl_3$, whereas in case of MIC's, hercynite was the intermediate product along with FeO and with increasing Al content in MIC, formation of Fe phase took place along with Al_2O_3.

ACKNOWLEDGEMENT

REFERENCES

[1] Fisher SH, Grubelich MC, Theoretical energy release of thermites, intermetallics and combustible metals, Proceedings of the 24th International Pyrotechnics Seminar, IIT Research Institute Chicago, July 1998;27–31:231–286.

[2] Bezmelnitsyn A, Thiruvengadathan R, Barizuddin S, Tappmeyer D, Apperson S, Gangopadhyay K, Gangopadhyay S, Mmodified nanoenergetic composites with tunable combustion characteristics for propellant applications, Propellants Explos. Pyrotech. 2010;35:384 – 394.

[3] Martirosyan KS, Wang L, Luss D, Development of Nanoenergetic Gas-Generators, NANO '08, 8th IEEE Conference on Nanotechnology, 2008; 817-818.

[4] Martirosyan KS, Hobosyan M, Lyshevsk SE, Enabling nanoenergetic materials with integrated microelectronics and MEMS platforms (2012) 12th IEEE International Conference on Nanotechnology (lEEE-NANO) The International Conference Centre Birmingham, Birmingham, United Kingdom August 2012; 20-23, .

[5] Song E, Tracy GV, Enhanced incendiary grenade, Proceedings of the 27th International Pyrotechnics Seminar, IIT Research Institute Chicago, July 16-21, 2000;393-411.

[6] Cao G, Orr`u R, Self-propagating reactions for environmental protection: state of the art and future directions, Chem. Eng. J. 2002;87: 239–249.

[7] Sannia M, Orr`u R, Concas A, Cao G, Self-propagating reactions for environmental protection: remarks on the treatment and recycling of zinc hydrometallurgical wastes, Ind. Eng. Chem. Res. 2001;40:801–807.

[8] Porcu M, Orr`u R, Cao G On the use of industrial scraps for the treatment of zinc hydrometallurgical wastes by self-propagating reactions, Chem. Eng. J. 2004;99:247–256.

[9] Kallio M, Ruuskanen P, M¨aki J, P¨oyli¨o E, L¨ahteenm¨aki S, Use of the aluminothermic reaction in the treatment of steel industry by-products, J. Mater. Synth. Process. 2000;8(2): 87–92.

[10] Travitzky N, Kumar P, Sandhage KH, Janssen R, Claussen N, Rapid synthesis of Al_2O_3 reinforced Fe–Cr–Ni composites, Mater. Sci. Eng. A 2003;344: 245–252.

[11] Dong Y, Yan D, He J, Li X, Feng,W, Liu H, Studies on composite coatings prepared by plasma spraying Fe_2O_3–Al self-reaction composite powders, Surf. Coat. Technol. 2004;179:223–228.

[12] Miagkov VG, Polyakova KP, Bondarenko GN, Polyakov VV, Granular Fe–Al_2O_3 films prepared by self-propagating high temperature synthesis, J. Magn. Magn. Mater. 2003;258–259: 358–360.

[13] Yang J, La P, Liu W, Hao Y, Microstructure and properties of Fe_3Al–$Fe_3AlC_{0.5}$ composites prepared by self-propagating high temperature synthesis casting, Mater. Sci. Eng. A 2004;382: 8–14.

[14] Deevi SC, Sikka VK, Swindeman CJ, Seals RD, Application of reaction synthesis principles to thermal spray coatings, J. Mater. Sci. 1997;32: 3315–3325.

[15] Chakraborty SP, Sharma IG, Suri AK, Bose DK, Studies on preparation, characterisation and evaluation of properties of Fe_3Al-based intermetallic alloy of composition Fe–16Al–5.44Cr–1Nb–0.5C, J. Mater. Process. Technol. 2001;115: 413–422.

[16] Jin S, Shen P, Zhou D, Jiang Q, A common regularity of stoichiometry-induced morphology evolution of transition metal carbides, nitrides, and diborides during self-propagating high-temperature synthesis, Cryst. Growth Des.2012;12: 2814 – 2824.

[17] Collins ES, Pantoya ML, Daniels MA, Prentice DJ, Steffler ED, Arche SPD, Heat flux analysis of a reacting thermite spray impingent on a substrate, Energy Fuels 2012;26: 1621 – 1628.

[18] Schoenitz M, Dreizin EL Consolidated energetic nanocomposites: mechanical and reactive properties", Proceedings Of Thirty-Sixth Annual Conference of I.C.T. and Thirty-Second International Pyrotechnics Seminar, 28 June-1 July 2005, Karlsruhe, Federal Republic of Germany, Poster 133.

[19] Tillotson TM, Gash AE, Simpson RL, Hrubesh LW, Satcher Jr JH., Poco JF, Nanostructured energetic materials using sol–gel methodologies, J. Non-Cryst. Solids 2001;285: 338–345.

[20] Menon L, Patibandla S, Bhargava Ram K, Shkuratov SI, Aurongzeb D, Holtz M, Berg, J Yun J, Temkin H, Ignition studies of Al/Fe$_2$O$_3$ energetic nanocomposites, Appl. Phys. Lett. 2004; 84(23): 4735–4737.

[21] Zhao N, He C, Liu J, Gong H, Zhang J, Dependence of catalytic properties of Al/Fe2O3 thermites on morphology of Fe2O3 particles in combustion reactions Journal of Solid State Chemistry, 2014:219: 67-73

[22] Roeen GA, Bozorg SFK, Nosko M, Švec P, Reactive mechanism and mechanical properties of in-situ hybrid nano-composites fabricated from anAl–Fe2O3 system by friction stir processing, Mater Character, 2017;127: 279-287

[23] Sanders VE, Asay BW, Foley TJ, Tappan BC, Pacheco AN, Son SF, Reaction propagation of four nanoscale energetic composites (Al/MoO$_3$, Al/WO$_3$, Al/CuO, and B1_2O$_3$), J Propul. Power 2007;23(4): 707-714.

[24] Aumarm CE, Skofronick GL, Martin JA, Oxidation behaviors of aluminum nanopowders, J. Vac. Sci. Technol. B 1995; 13(2): 1178-1183.

[25] Yong Lde, Park B, Valenta F, A study of the radiant ignition of a range of pyrotechnic materials using a CO$_2$ Laser, MRL Technical Report, MRL-TR- 1990; 90,20.

[26] Plantier K, Combustion behavior of Nano composite Al/Fe$_2$O$_3$, MSc Thesis, Texas Tech University (USA), May 2004.

[27] Sarangi B, SarangI A, Ray HS, Kinetics of aluminothermic reduction of MnO$_2$ and Fe$_2$O$_3$: A thermoanalytical investigation, SIJ Int. 1996; 36(9): 1135-1141.

[28] Duraes L, Costa BPO, Santos R, Correia A, Camposd J, Portugal A, Fe$_2$O$_3$/aluminum thermite reaction intermediate and final products, Mater. Sci. Eng. A 2007;465: 199–210.

[29] Mei J, Halldearn RD, Xiao P, Mechanisms of the aluminium-iron oxide thermite reaction, Scripta Mater. 1999; 41(5): 541–548.

[30] FanRH, Lu HL, Suna KL, Wang WX, Yi XB, Kinetics of thermite reaction in Al-Fe$_2$O$_3$ system, Thermochim. Acta 2006; 440: 129–131.

[31] Bullian CJ, Swiatkiewicz JJ, Puszynski JA, Investigation of reaction mechanisms and combustion characteristics of nanothermites, Particle Technology Forum-03, AlChE Annual Meeting, Oct-Nov-2005, No-511d.

[32] Weiser V, Roth E, Raab A, Mar M del, Lorenzo J, Kelzenberg S, Eisenreich N, Thermite type reactions of different metals with iron-oxide and the influence of pressure, Propellants Explos. Pyrotech. 2010;35 :240 – 247.

[33] Cheng JL, Hng HH, Lee YW, Du SW, Thadhani NN, Kinetic study of thermal- and impact- initiated reactions in Al-Fe$_2$O$_3$ nanothermite. Comb.Flame 2010;157:2241-2249.

[34] Wang Y, Song Xl, , Jiang W,, Deng GD,, Guo XD, Liu HY, Li FC, Mechanism for thermite reactions of aluminum/iron-oxide nanocomposites based on residue analysis Trans. Nonferrous Met. Soc. China 2014;24: 263-270

[35] Sahoo SK, Agarwal K, Singh AK, Polke BG, Raha KC, Characterization of γ- and α-Fe$_2$O$_3$ nano powders synthesized by emulsion precipitation-calcination route and rheological behaviour of α-Fe$_2$O$_3$, Int J Eng. Sci Technol., 2010; 2(8): 118-126.

[36] Berger B, Parameters influencing the pyrotechnic reaction, Propellants Explos. Pyrotech. 2005;30: 27-35.

[37] Wang SX, Liang KM, Zhang XH Wang GL, Influence of heating rate on DTA curve on aluminothermic reaction, J. Mater. Sci. Lett. 2003;22: 855-856.

[38] Jian G, Chowdhury S, Sullivan K, Zachariah MR, Nanothermite reactions: Is gas phase oxygen generation from the oxygen carrier an essential prerequisite to ignition?, Comb. Flame 2013;160: 432–437.

[39] Asay BW, Son SF, Busse JR, Oschwald DM, Ignition characteristics of metastable intermolecular composites, Propellants, Explos., Pyrotech. 2004;29: 216-219.

[40] Bockmon BS, Pantoya ML, Son SF, Asay BW, Mang JT, Combustion velocities and propagation mechanisms of metastable interstitial composites, J. Appl. Phys. 2005;98: 064903.

[41] Jones DEG, Fouchard RC, Turcotte AM, Kwok QSM, Brousseau P, Thermal characterization of passivated nanometer size aluminium powders, 27th International Pyrotechnics Seminar, IIT Research Institute Chicago, July 16-21, 2000; 821-830.

[42] Kwok QSM, Fouchard RC, Turcotte AM, Lightfoot PD, Bowes R, Jones DEG, Characterization of aluminum nanopowder compositions, Propellants Explos., Pyrotech. 2002;27: 229 - 240.

[43] Bensouyad H, Hamana D, Analysis methods for the determination of energies activation and the study of the precipitation reactions in Al-4.5% weight Cu alloys, J Eng Appl Sci, 2008;3(7): 583-586,

[44] Heireche L, Belhadji M, The methods Matusita, Kissinger and Ozawa in the study of the crystallization of glasses, the case of Ge-Sb-Te alloys, Chalcogenide Lett. February 2007;4(2): 23 – 33.

[45] Starink MJ, The determination of activation energy from linear heating rate experiments: a comparison of the accuracy of isoconversion methods, Thermochim. Acta 2003; 404:163.

Parametric Analysis on Buildings with Connecting Corridors

Afiya V N

Research Scholar, Department of Civil Engineering, FISAT, Mahathma Gandhi University, Kerala
Email: afiyavn@gmail.com

Abstract—The architectural design of modern buildings has been highly integrated and multi-functional. Connected high-rise structures, which comprise of main towers and corridor in between at a certain height falls under the category of irregular building structure system. This thesis presents a study on the various buildings with connecting structures, under lateral loading conditions such as the seismic loads. The software ETABS was used for modeling the structure. Linear static analysis and linear dynamic analysis was conducted to analyse the models. For seismic loading, the parameters such as storey displacements, storey drifts, overturning moment, base shear, axial and bending moments in the corridor beams are studied. It is understood that each building behaved differently under seismic loads.

Keywords—base shear, connected corridors, drift, overturning moment seismic analysis.

I.   INTRODUCTION

Earthquakes has always been a major hazard to human beings as well as structures which serve humans important facilities. Seismic analysis is the branch of structural analysis which calculates the response of structures to earthquakes. Double tower connected building is a kind of complicated structure form with two single towers as major structure which are connected by linkwork such as corridors. The connecting body is provided at a certain height and forms an irregular building structural system. More and more connected structures with long- span corridors have been constructed during the years.

The connection provide convenience for communication among different towers and is an important means of escape when one tower suffers calamities like fire. Static performance of high rise connected structure is simple and mature. Location of connection will change the dynamic characteristics of tall buildings and can also change the response caused by earth quake, wind or other loads. The behaviour of the structure as well as the members of the corridor depends on the type of connection used for the corridor.

II.   OBJECTIVES

The objective has been formulated based on gaps that have been faced in study related to connected structures. The objectives of this study include the study on the behaviour of twin buildings with connecting corridor under dynamic loading and its behaviour with changes of connecting beam location with varying span.

III.   MODELLING OF THE STRUCTURE

The building used for the study is a reinforced concrete ten storied twin tower with connecting corridors at different storey levels and with varying spans of corridors. Both in the transverse and longitudinal directions the model has 3 bays with each bay having 8m as centre to centre distance. The story height is 3 m for all storeys. The base nodes of all columns are restrained against translation and rotation about all the 3 global axes. The properties of various frame member sections are listed in table 1.

TABLE 1
MEMBER SPECIFICATIONS

Member type	Dimension	Material property
Column	650 mm x 650 mm	M_{30} & Fe_{415}
Beam	300 mm x 800 mm	M_{25} & Fe_{415}
Slab	120 mm thick	M_{25} & Fe_{415}
Shear wall	200 mm thick	M_{30} & Fe_{415}

TABLE 2
MODELS USED FOR STUDY

Sl No	Model	Configuration
1	Model 1	Corridor connected on second storey with 4m span
2	Model 2	Corridor connected on second storey with 6m span
3	Model 3	Corridor connected on second storey with 8m span
4	Model 4	Corridor connected on fifth storey with 4m span
5	Model 5	Corridor connected on fifth storey with 6m span
6	Model 6	Corridor connected on fifth storey with 8m span
7	Model 7	Corridor connected on tenth storey with 4m span
8	Model 8	Corridor connected on tenth storey with 6m span
9	Model 9	Corridor connected on tenth storey with 8m span

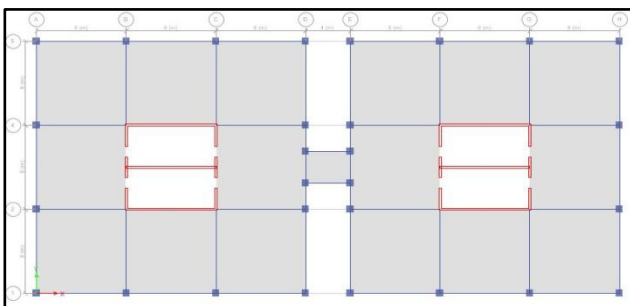## IV.   STRUCTURAL MODELLING IN ETABS

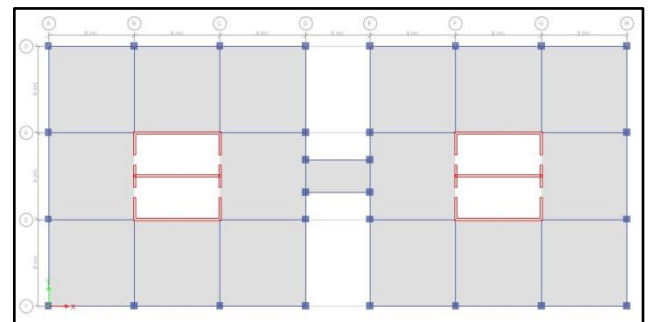FIG 1: PLAN VIEW OF THE BUILDING WITH 4m SPAN CONNECTING CORRIDOR

FIG 2: PLAN VIEW OF THE BUILDING WITH 6m SPAN CONNECTING CORRIDOR
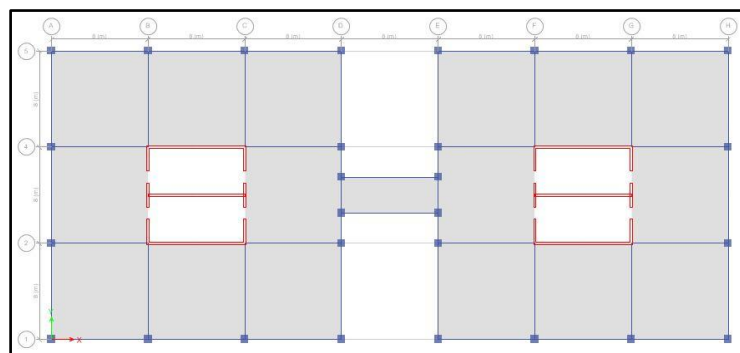

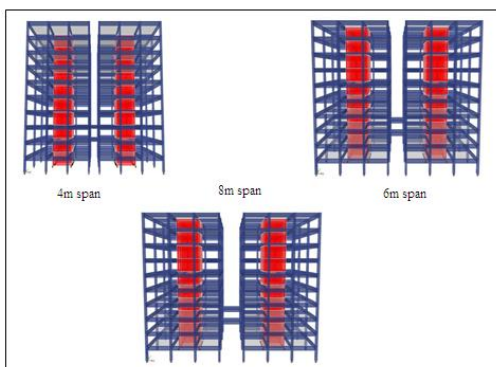FIG 3: PLAN VIEW OF THE BUILDING WITH 8m SPAN CONNECTING CORRIDOR

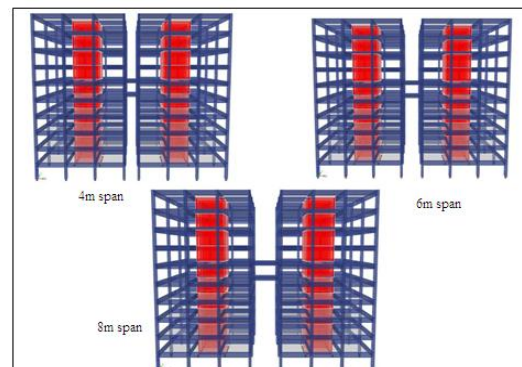FIG 4: 3D RENDERED VIEW OF MODEL WITH CORRIDOR CONNECTION AT 2nd storey

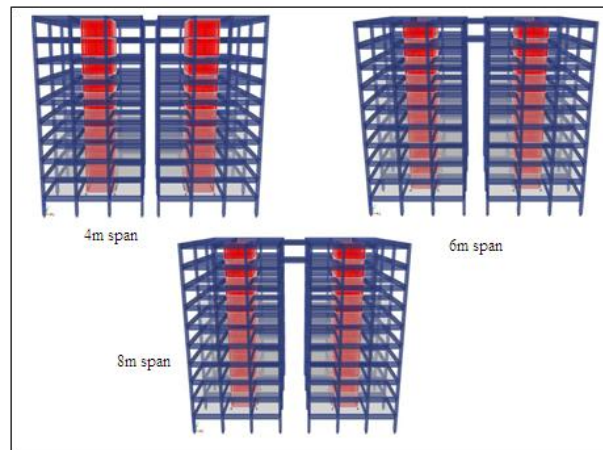FIG 5: 3D RENDERED VIEW OF MODEL WITH CORRIDOR CONNECTION AT 5th storey

FIG 6: 3D RENDERED VIEW OF MODEL WITH CORRIDOR CONNECTION AT 10thstorey

TABLE 3
LOAD DETAILS

Gravity loads	Wind load	Earthquake load
Dead Load (beams and columns) = ETABS calculated	V_b = 39m/s	Zone = III (0.16)
Self weight of slab = 3kN/m^2	Risk coefficients, k1 = 1	Importance factor = 1
Floor finish = 1kN/m^2	Topography factor, k3 =1	Site is hard/rocky site (Type I)
Frame loads = 12kN/m	Terrain category = 2	Response reduction factor taken = 5
Live load (except corridor) = 2kN/m^2	Structure class = B	The seismic load calculations are done by the program by default.
Live load (corridor) = 3kN/m^2	C_p (windward) = 0.8 ,C_p (leeward) = 0.5	

V.   STRUCTURAL ANALYSIS

The structural analysis is a mathematical algorithm process by which the response of a structure to specified loads and actions is determined.

5.1   Linear Dynamic Analysis

Linear Dynamic Analysis can be either the Modal Response Spectrum Method or the Numerical Integration Linear Time History Method using a structural model but in both cases, the corresponding internal forces and displacements are determined using linear elastic analysis. The ground motion histories used in the Numerical Integration Linear Time History Method shall be compatible with a response spectrum constructed from the design spectral acceleration values. The advantage of these linear dynamic procedures with respect to linear static procedures is that higher modes can be considered.

5.2   Response-spectrum analysis

Response-spectrum analysis (RSA) is a linear-dynamic statistical analysis method which measures the contribution from each natural mode of vibration to indicate the likely maximum seismic response of an essentially elastic structure. Response-spectrum analysis provides insight into dynamic behavior by measuring pseudo-spectral acceleration, velocity, or displacement as a function of structural period for a given time history and level of damping. It is practical to envelope response spectra such that a smooth curve represents the peak response for each realization of structural period.

VI.   RESULTS AND DISCUSSIONS

6.1   Storey Displacement

The maximum displacement is determined after the analysis for 9 models. The curve shows storey displacement graphs for different cases studied.

FIG 7: STOREY DISPLACEMENTS ALONG X DIRECTION

TABLE 4
STOREY DISPLACEMENTS ALONG X DIRECTION

STOREY	CORRIDOR AT STOREY 2			CORRIDOR AT STOREY 5			CORRIDOR AT STOREY 10		
	4m span	6m span	8m span	4m span	6m span	8m span	4m span	6m span	8m span
10	23.8	23.9	23.9	23.6	23.7	23.8	23.5	23.5	23.6
9	21.3	21.3	21.4	21.1	21.1	21.2	21	21.1	21.2
8	18.4	18.5	18.5	18.2	18.3	18.3	18.1	18.1	18.2
7	15.5	15.5	15.6	15.3	15.3	15.4	15.2	15.2	15.3
6	12.6	12.6	12.7	12.3	12.4	12.5	12.3	12.3	12.3
5	9.7	9.8	9.8	9.5	9.6	9.6	9.4	9.4	9.5
4	7	7.1	7.1	6.8	6.8	6.9	6.8	6.8	6.8
3	4.6	4.6	4.7	4.4	4.4	4.5	4.4	4.4	4.4
2	2.5	2.5	2.5	2.4	2.4	2.4	2.4	2.4	2.4
1	0.9	0.9	0.9	0.9	0.9	0.9	0.8	0.8	0.9
0	0	0	0	0	0	0	0	0	0
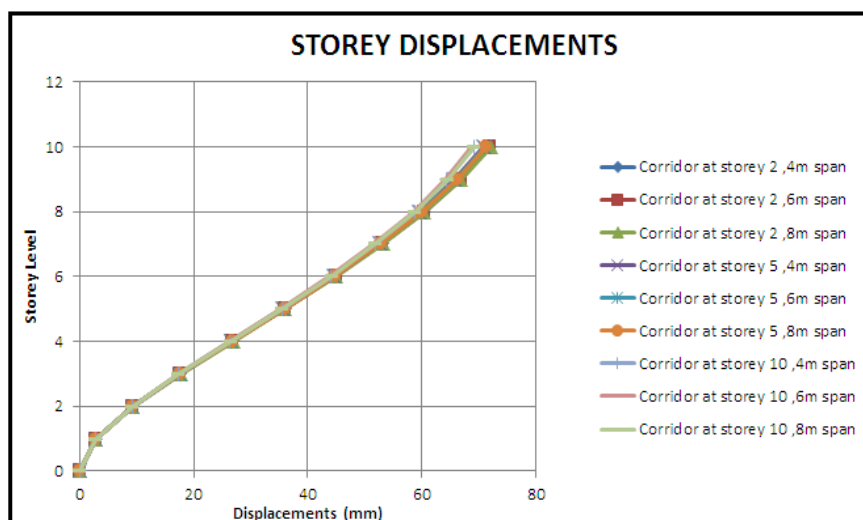
FIG 8: STOREY DISPLACEMENTS ALONG Y DIRECTION

TABLE 5
STOREY DISPLACEMENTS ALONG Y DIRECTION

Storey	Corridor at storey 2			Corridor at storey 5			Corridor at storey 10		
	4m	6m	8m	4m	6m	8m	4m	6m	8m
10	71.9	72	72.1	70.8	71.1	71.2	69.1	68.8	69.1
9	66.6	66.8	66.9	65.7	66	66.1	64.4	64.2	64.6
8	60.3	60.4	60.5	59.6	59.8	59.9	58.7	58.5	58.9
7	53	53.1	53.2	52.5	52.7	52.8	51.9	51.7	52
6	44.8	44.9	45	44.5	44.7	44.8	44.1	43.9	44.2
5	36	36	36.1	35.6	35.8	35.9	35.5	35.3	35.6
4	26.7	26.8	26.9	26.5	26.6	26.7	26.4	26.3	26.5
3	17.6	17.6	17.7	17.5	17.6	17.6	17.4	17.3	17.4
2	9.2	9.2	9.3	9.3	9.3	9.3	9.2	9.2	9.2
1	2.9	2.9	2.9	2.9	2.9	2.9	2.9	2.9	2.9
0	0	0	0	0	0	0	0	0	0

It is seen that the maximum displacement occurs for buildings with corridor at storey 2. The displacement is independent of the span of corridor and shows variation when the level of connection change. The displacement is maximum along the Y direction.
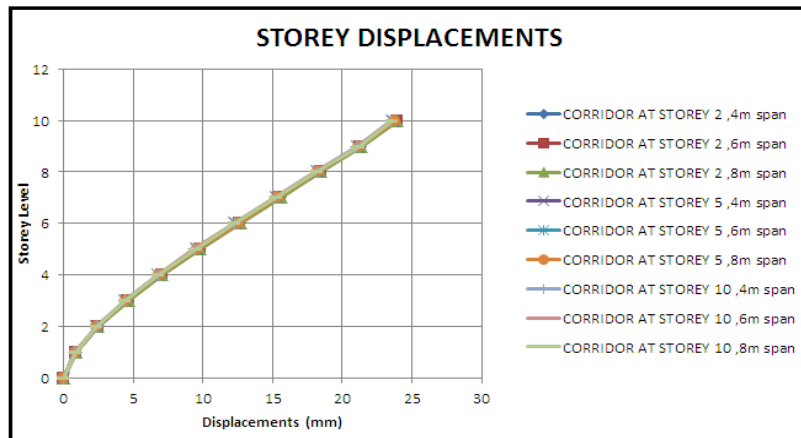
6.2   Storey Drift
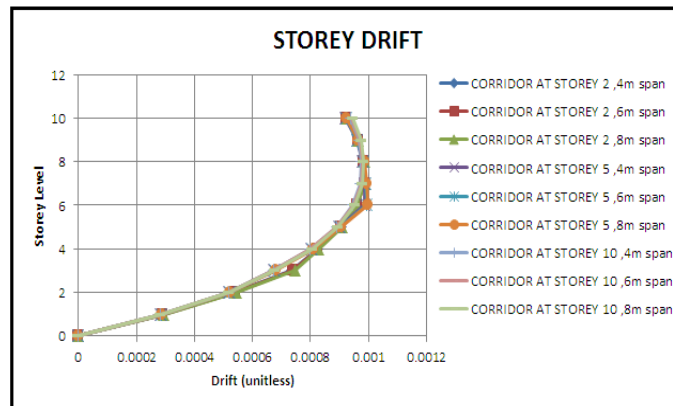
FIG 9: STOREY DRIFT ALONG X DIRECTION

TABLE 6
STOREY DRIFT ALONG X DIRECTION

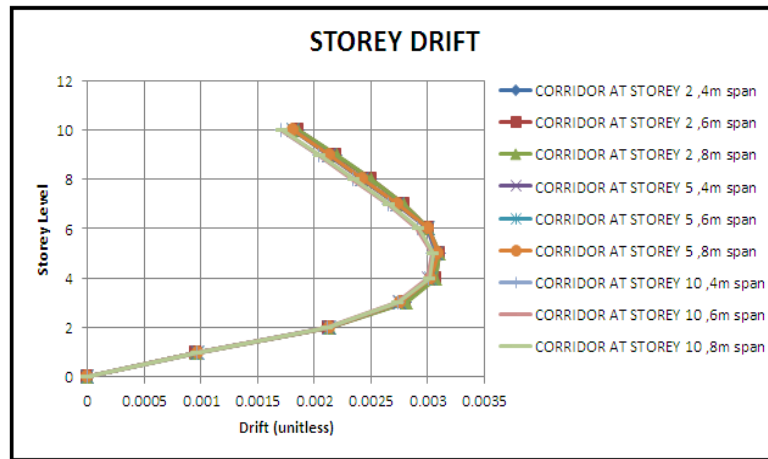| STOREY	CORRIDOR AT STOREY 2			CORRIDOR AT STOREY 5			CORRIDOR AT STOREY 10		
	4m span	6m span	8m span	4m span	6m span	8m span	4m span	6m span	8m span
10	0.000923	0.000923	0.000924	0.00092	0.000922	0.000925	0.00094	0.000942	0.000946
9	0.000963	0.000964	0.000966	0.000959	0.000962	0.000965	0.000969	0.000972	0.000977
8	0.000983	0.000984	0.000986	0.00098	0.000983	0.000986	0.000976	0.000978	0.000983
7	0.000983	0.000985	0.000987	0.000986	0.000989	0.000993	0.000973	0.000975	0.00098
6	0.000958	0.00096	0.000962	0.000987	0.000993	0.000998	0.000946	0.000948	0.000953
5	0.000904	0.000906	0.000908	0.000899	0.000903	0.000907	0.00089	0.000891	0.000895
4	0.000823	0.000825	0.000828	0.000802	0.000806	0.000809	0.000799	0.0008	0.000804
3	0.000737	0.000741	0.000746	0.000674	0.000677	0.00068	0.000672	0.000673	0.000676
2	0.000537	0.00054	0.000543	0.000519	0.000521	0.000523	0.000517	0.000517	0.000519
1	0.00029	0.000291	0.000293	0.000284	0.000285	0.000286	0.000283	0.000283	0.000284
0	0	0	0	0	0	0	0	0	0

FIG 10: STOREY DRIFT ALONG Y DIRECTION

TABLE 7
STOREY DRIFT ALONG Y DIRECTION

STOREY	CORRIDOR AT STOREY 2			CORRIDOR AT STOREY 5			CORRIDOR AT STOREY 10		
	4m span	6m span	8m span	4m span	6m span	8m span	4m span	6m span	8m span
10	0.001857	0.001858	0.00186	0.00181	0.001811	0.001811	0.001709	0.001707	0.001715
9	0.002192	0.002194	0.002198	0.002129	0.002134	0.002135	0.002042	0.002038	0.002045
8	0.002498	0.002501	0.002505	0.002418	0.002424	0.002426	0.00234	0.002334	0.002348
7	0.002785	0.002788	0.002792	0.002727	0.002735	0.002738	0.002654	0.002648	0.002664
6	0.002998	0.003002	0.003006	0.002993	0.003003	0.003009	0.002906	0.002898	0.002915
5	0.003098	0.003102	0.003106	0.003069	0.003081	0.003087	0.003043	0.003033	0.003052
4	0.00306	0.003065	0.00307	0.003011	0.003024	0.00303	0.003011	0.003	0.003018
3	0.002798	0.002805	0.00281	0.002743	0.002755	0.002761	0.002735	0.002722	0.002739
2	0.002119	0.002127	0.002131	0.002124	0.002134	0.002139	0.002109	0.002099	0.002113
1	0.000952	0.000956	0.000958	0.000969	0.000974	0.000977	0.000961	0.000956	0.000963
0	0	0	0	0	0	0	0	0	0

Along both the directions, the storey drift shows a smooth curve and shows a small variation along the span of corridor and the level of connection.

6.3   Overturning Moment

Response to earthquake ground motion results in a tendency for structures and individual vertical elements of structures to overturn about their bases. Although actual overturning failure is very rare, overturning effects can result in significant stresses. The overturning moment at the base for different locations and for different spans of corridors are compared below.

TABLE 8
OVERTURNING MOMENT AT THE BASE ALONG X DIRECTION

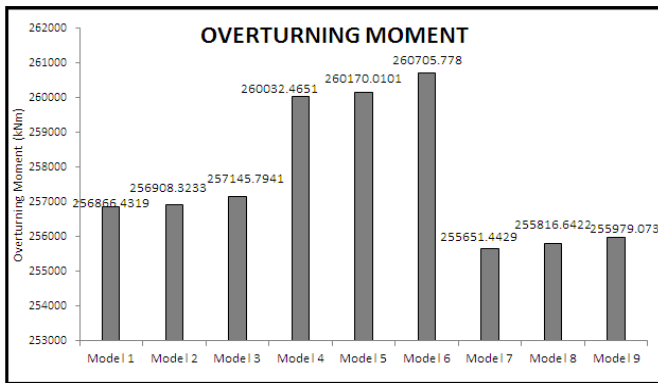|	Corridor at Storey 2			Corridor at Storey 5			Corridor at Storey 10		
	4m	6m	8m	4m	6m	8m	4m	6m	8m
X	256866.4	256908.3	257145.8	260032.5	260170	260705.8	255651.4	255816.6	255979.1
Y	409298.3	409481	409853	410716.2	411253.2	411581.3	411910.6	412030.4	413668.1

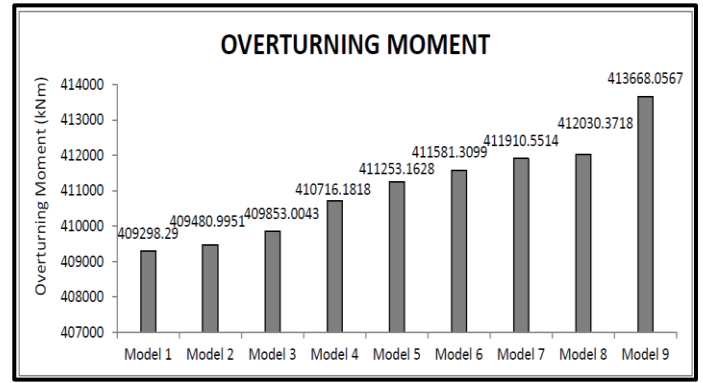**FIG 11: OVERTURNING MOMENT AT THE BASE ALONG X DIRECTION**

FIG 12: OVERTURNING MOMENT AT THE BASE ALONG Y DIRECTION

It is observed that the building experiences lesser overturning moment when the corridor location is at storey 2 with 4m span. The overturning moment is observed higher when the corridor is at storey 10 with 8m span. There is an increasing variation of overturning moment when corridor location increases to the top and with increasing span.

6.4 Base Shear

Base shear is an estimate of the maximum expected lateral force that will occur due to seismic ground motion at the base of a structure.
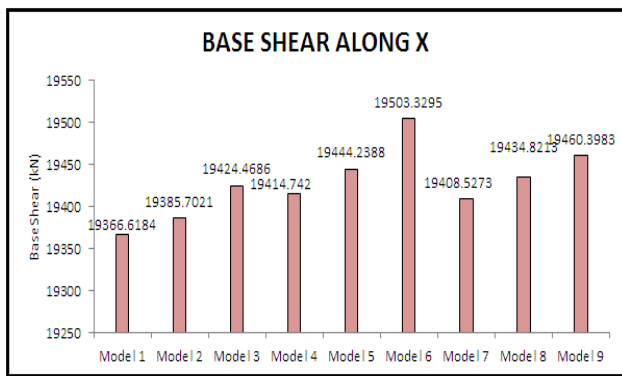
FIG 13: BASE SHEAR ALONG X DIRECTION
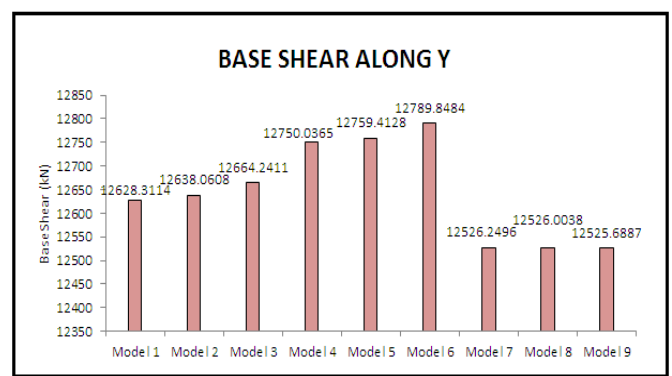
FIG 14: BASE SHEAR ALONG Y DIRECTION

TABLE 9
BASE SHEAR ALONG X AND Y DIRECTION

Span	Corridor at storey 2			Corridor at storey 5			Corridor at storey 10		
	4m	**6m**	**8m**	**4m**	**6m**	**8m**	**4m**	**6m**	**8m**
Base shear along X	19366.62	19385.7	19424.47	19414.74	19444.24	19503.33	19408.53	19434.82	19460.4
Base shear along Y	12628.31	12638.06	12664.24	12750.04	12759.41	12789.85	12526.25	12526	12525.69

The maximum base shear is seen along the X direction. The maximum shear occurred in model 6 in which the corridor is located at the midspan (5th storey) with 8m span. The minimum occurred in model 1 where corridor is at 2nd storey with 4m span.

6.5 Axial force in the connecting beams

The variation of axial force in the connecting beam of the corridor are plotted both for the beams at the top and bottom section.
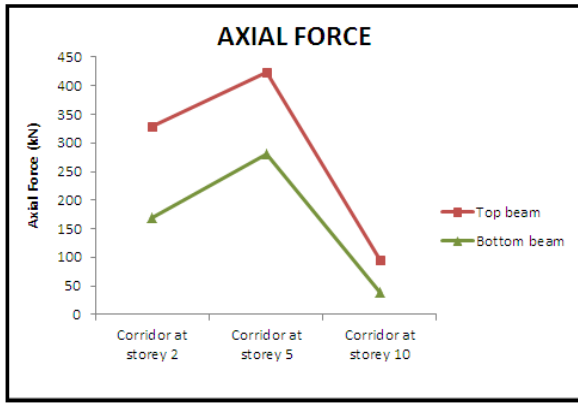
FIG 15: AXIAL FORCE VARIATION FOR SPAN 4m
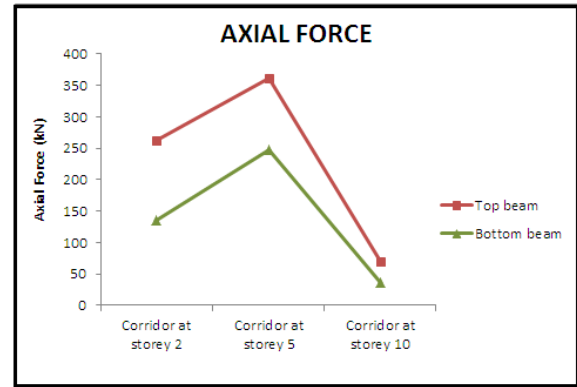
FIG 16: AXIAL FORCE VARIATION FOR SPAN 6m
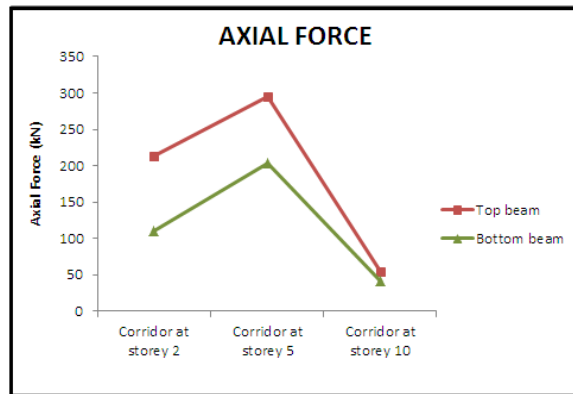
FIG 17: AXIAL FORCE VARIATION FOR SPAN 8m

TABLE 10
AXIAL FORCE IN THE CONNECTING BEAMS OF CORRIDOR

	Corridor at storey 2			Corridor at storey 5			Corridor at storey 10		
Span	4m	6m	8m	4m	6m	8m	4m	6m	8m
Top beam	329.8088	261.5162	213.134	424.2818	362.1466	295.3945	95.9864	69.5933	55.2068
Bottom beam	169.1094	136.1904	110.9416	279.7786	247.0731	203.8297	38.1974	36.0298	31.3848

From the table 10, it is seen that the axial force developed in the beams increases to the to the mid-span and then decreases when the location of connecting beams shifts to the top storey. Maximum axial force is developed when the corridor is connected at the mid-span with 4m span and minimum axial force is when the corridor is located at the top storey.

6.6   Bending moment in the connecting beams
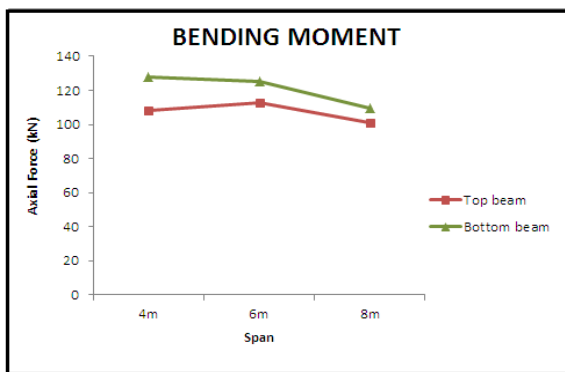
FIG 18: BENDING MOMENT VARIATION FOR CORRIDOR AT STOREY 2
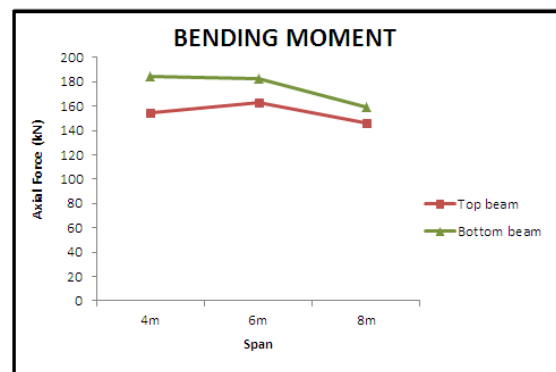
FIG 19: BENDING MOMENT VARIATION FOR CORRIDOR AT STOREY 5
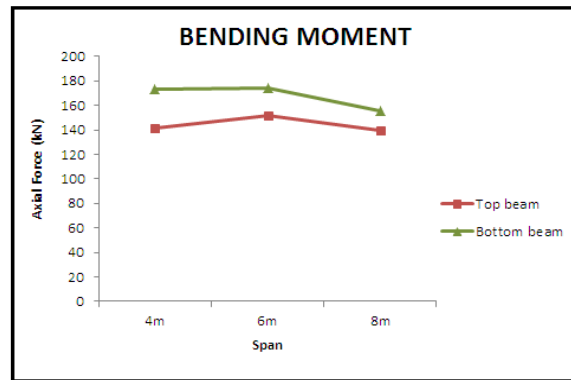
FIG 20: BENDING MOMENT VARIATION FOR CORRIDOR AT STOREY 10

TABLE 11
BENDING MOMENTS IN THE CORRIDOR BEAMS

Span	Corridor at storey 2			Corridor at storey 5			Corridor at storey 10		
	4m	6m	8m	4m	6m	8m	4m	6m	8m
Top beam	108.2642	112.7959	101.2085	154.9681	162.8562	146.0776	141.68	151.8728	139.717
Bottom beam	127.6075	125.1119	109.5206	184.5692	182.2704	159.2228	173.5324	174.0001	155.2175

The bending moments increases from 4m span to 6m span models and then decreases in 8m span models for top beams. As the location of the corridor changes bending moment increases and maximum obtained when the corridor is at the midspan. In the case of bottom beams bending moment shows a decreasing tendency with span.

6.7   Discussion

The discussion of the results obtained for the models can be explained by taking into consideration each parameter.

➤ **Storey displacement and Storey drift**

The storey displacements and storey drifts for seismic loading are found. Maximum displacement occurred along the Y direction and is seen in models where the corridor is connected at the second storey. The maximum displacement depends on the span of the corridor and is less varied with changing location of corridors. The minimum displacement is obtained when the corridor is located on the tenth storey. The storey drift is maximum along the Y direction. A sudden variation in drift is seen after the location of corridors in case of wind loading along the X direction.

➤ **Overturning Moment**

The overturning moment is seen maximum when the corridor is connected at the tenth storey with maximum span. The least value of overturning moment is observed for models with corridors at storey 2. The overturning moment increased with increasing altitude of connection of corridor and with increasing span.

➤ **Base Shear**

The maximum base shear is seen along the X direction. The maximum base shear is seen when the corridor location is at mid-span of the structure.

➤ **Axial Force and Bending Moments**

The axial force and bending moment developed in the corridor beams is maximum when they are located to the midspan of the structure. As the location of beams shifts to the top storey the axial force gets decreased. As the location of the corridor changes bending moment increases. In the case of beams at the bottom bending moment shows a decreasing tendency with span.

VII.   CONCLUSION

Compared with the ordinary buildings, the characteristics of connected buildings are complex and changes with the connection location. These high and flexible structures have large movements under lateral forces like earthquakes and

winds. The effort of the connecting corridor location changes the structure behaviour in terms of displacement, drift, overturning moment, base shear, axial force and bending moments. The results indicate that the horizontal displacement and drift under seismic loading in Y direction is larger than the displacements and drifts in X direction. Overturning moment depends on location and span of the corridors. The effort to maximum base shear is larger in X direction than Y direction. The above results provide references for design and for further study.

VIII.   SCOPE OF FUTURE WORK

This research and investigation has opened a vast scenario for future studies. In this subject, extensive explorations can be conducted with a wide range of variation in connecting corridors and building characteristics.

Further studies may be carried out by adding the following variations to the research prototypes;

- Variation in span of the connecting corridors.

- Incorporating multiple corridors within the structure.

- Steel connections for the corridor.

- Corridors between varying altitude towers.

- Changing the type of connection of corridor to the structure.

IX.   REFERENCES

[1]   ETABS 2015 Tutorial, *https://www.csiamerica.com/products/etabs/watch-and-learn*

[2]   Huang, Zhenkang Chen Xing, Jiao Ke, Lai Hongli, *"The Elastic-plastic Dynamic Analysis Software GSEPA And Its Application In Seismic Analysis Of Tall Buildings"*, The 14th World Conference On Earthquake Engineering, October 12-17,2008, Beijing, China

[3]   IS: 456-2000," *Indian Standard Plain and Reinforced Concrete - Code of Practice (Fourth Revision)"*, Bureau of Indian Standards, New Delhi.

[4]   IS: 875 (Part I)-1987, *"Indian Standard Code of Practice for Design Loads (Other than earthquake) for Building and Structures"*, Bureau of Indian Standards, New Delhi.

[5]   IS: 875 (Part II)-1987, *"Indian Standard Code of Practice for Design Loads (Other than earthquake) for Building and Structures"*, Bureau of Indian Standards, New Delhi.

[6]   IS: 875 (Part III)-1987, *"Indian Standard Code of Practice for Design Loads (Other than earthquake) for Building and Structures"*, Bureau of Indian Standards, New Delhi.

[7]   IS: 1893 (Part 1) 2002- Indian standard, *"Criteria for earthquake resistant design of structures",* Bureau of Indian Standards, New Delhi.

[8]   Jiachan Cui, Chengming Li, Wei Tian, Dongya An, *"The Application Of ABAQUS In Seismic Analysis Of Connected Structures"*, SIMULA Customer Conference, 2010

[9]   Ji Dongyu, Li Xiaofen *"Seismic Behavior Analysis Of High-Rise Connected Structure",* International Conference On Mechatronics, Electronic, Industrial And Control Engineering (MEIC 2014)

[10]   Ji Dongyu , Song Chunca, *"Dynamic Characteristics Analysis of High-rise Connected Structure" ,* International Conference on Mechatronics, Electronic, Industrial and Control Engineering (MEIC 2014)

[11]   Liu Wei,   Shu   Ganping,   *"Performance   Analysis   of   Key   Joints   and   Seismic   Design   of High-rise Structures"*, The Open Construction and Building Technology Journal , 2015, 9,7-11

[12]   W. Lin, G. M. Zhang, A. Qi , *"Seismic Behavior of Long-span Connected Structures under Multi-supported and Multi-dimensional Earthquake excitations"*, 15 World Conferences on Earthquake Engineering (*WCEE*) *2012*

[13]   Xilin Lu, Ying Zhou, *"Seismic Performance of Multi-tower Hybrid Structure",*Earthquake Engineering and Engineering Vibration, 8(1): 1-13

[14]   Ying Zhou, Xilin Lu, Jiang Qian, *"Dynamic Test On A Multi-tower Connected Building Structure",*Proceedings Of The 3rd International Conference On Advances In Experimental Structural Engineering, San Francisco, USA, 2009

[15]   Y. Zhou, W J Yi, *"Ambient Vibration Measurement and Earthquake Resistant Behaviour Analysis on a Two-tower tall Building with Enlarged Base",* The 14th World Conference On Earthquake Engineering , October 12-17,2008, Beijing, China

[16]   Zheng Nina, Yang Zhihong, Yang Qiong, Dai Xun, Ji Shuyan, *"Influence Analysis of Connecting Style on Vertical Earthquake Response of High Rise Buildings with Connecting Structure",* The 14th World Conference on Earthquake Engineering, 2008.

Contact angle measurements with constant drop volume. Control of wettability of some materials by physico-chemical treatment

Vladimir I. Bredikhin[1*], Nikita M. Bityurin[2]

Institute of Applied Physics RAS, Nizhny Novgorod, Russia
Email: bredikh@appl.sci-nnov.ru (*corresponding author)

Abstract— *A modified express method of contact angle measurement based on determining the diameter of a drop with a known volume has been elaborated. The method offers a number of advantages: it can be used in an express manner for in situ dynamic investigation and makes it possible to observe inhomogeneity and anisotropy of hydrophilicity. The method is convenient in comparative measurements and does not require any special equipment.*

Using the proposed method, the possibility of hydrophilic control of some materials (silicate glass, TiO_2 (anataze) and polymetilmetacrylate (PMMA)) by UV (ultra violet) and chloroform vapor treatment has been studied. In particular, hydrophilicity of PMMA after UV irradiation was observed, and it is shown that changes in hydrophilicity are connected with the surface oxidation of PMMA. The observed phenomenon of hydrophilicity control can be used in various technologies, such as liquid coating, printing, spray quenching, nanolithography, pharmacology and others.

Keywords— *Contact angle, constant drop volume, control of hydrophilicity, physico-chemical treatment, PMMA, inorganic glass, TiO_2.*

I.   INTRODUCTION

Wetting between different liquids and solids have received tremendous interest from both fundamental and applied points of view. It plays an important role in many chemical technologies, such as oil recovery, lubrication, liquid coating, printing, spray quenching, and lithography [1, 2]. In recent years, there has been an increasing interest in the study of superhydrophobic and superhydrophilic surfaces, due to their potential applications in, for example, self-cleaning, nanofluidics, electrowetting, and nanolithography. Traditional way to study wetting is quantitative measurement of contact angle θ, which characterizes the shape of a liquid drop on a solid surface (or on another liquid) (see Fig. 1) [1, 2].
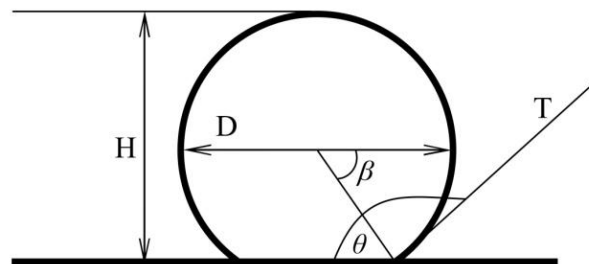
FIG. 1. DROP ON A SOLID SURFACE.

Currently, the primary method of measuring the contact angle θ is to observe the shape of the drop (volume of the order of 1 µcL) and measure the angle between the drop tangent T and the solid surface at the drop–solid contact point either directly or by calculating it from the drop diameter D and height H. Several methods and apparatuses were developed which permit to investigate wetting over the whole range of contact angles $0° < \theta < 180°$ in static and in dynamic regimes. Nevertheless, these methods have some limitations: they are not fast enough, do not allow investigating the anisotropy and homogeneity of wetting, and require special equipment.

II.   CONTACT ANGLE MEASUREMENT FROM A TOP VIEW IMAGE OF A DROP AT KNOWN DROP VOLUME

In Fig.1 it is evident that knowing the drop diameter D only is not enough to calculate the angle θ. For this purpose, it is convenient to use the drop volume V. In Fig.1 it can be clearly seen that the volume V and the drop radius R (in the spherical drop approximation) are related to the angle θ by

$$V = \pi R^3 \left| \int_{\pi-\theta}^{0} (sin\beta)^3 \, d\beta \right| \tag{1}$$

$$V = \pi R^3 \left(\frac{2}{3} + \left(\frac{\cos\theta^3}{3} \right) - \cos\theta \right)$$ (1a)

Expression (1a) gives limit cases:

$\theta \to \pi$ $R \to (3/4\pi)^{1/3} V^{1/3}$ (superhydrophobic case)

$\theta \to 0$ $R \to \infty$ (superhydrophilic case)

III. DROPS OF KNOWN VOLUME

From Eqs. (1) and (1a) it can be seen that it is possible to compare wetting for different measurements immediately if the volumes of drops are the same: larger diameter means better wetting and smaller angle θ. Therefore, this method is suitable for rapid, comparative investigations. For quantitative measurements of the contact angle θ by analyzing the drop shape from above one has to know the drop volume V and then calculate θ from Eq. 1a. It is useful to have drops of constant volume. To produce such drops, different micro dozers can be used, in particular, micro dozers based on capillary. In our experiments, the results of which will be discussed below, we used a standard syringe (~ 1 mL) with a normally clipped needle tip. The needle played the role of a micro-capillary when it was immersed in water (without additional piston force). Then the drop was pushed carefully from the capillary to a substrate by the piston. By using such a simple technique and maintaining stable operation conditions, water drops of ~ 1.5 µcL stable volume were produced.

The value of the drop volume V can be determined by measuring the volume of a sum of drops or alternatively by using the method of comparison, i.e. by fixing the drop on a substrate with a known contact angle θ known and calculating V from Eq. (1a). Fig. 2 shows an example of the dependence of contact angle θ on drop radius on logarithmic scales when the drop volume is 1 µcL. Note that the comparison method is very effective for express investigation of different substrates or in the process of treatment of the substrate or the liquid.
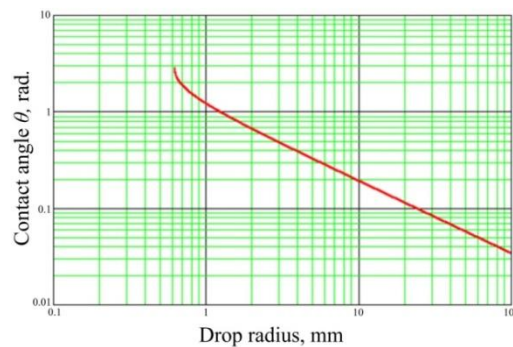

FIG. 2. DEPENDENCE OF CONTACT ANGLE θ ON DROP RADIUS. DROP VOLUME IS 1 µcL

IV. EXPERIMENTS ON WETTING CONTROL IN SEVERAL MATERIALS

4.1 Comparative study of the effect of UV irradiation on wetting of selected materials

We studied the impact of ultra violet UV irradiation (UV adaptation, UVA) on wettability of some transparent materials: silicate glass, polymetilmetacrylate (PMMA) and ~0.1 µm TiO_2 film (anataze) deposited on an object plate by the sol-gel method in a centrifuge [3,4]. In our experiments we used the "classic" conventional method of contact angle measurement, in which the drop shape is measured laterally, and the above-discussed modified method, in which areas of drops of the same volume are compared. We compared the shape and transverse size of a water drop on a substrate surface (i.e. top view of the drop) before and after treatment of the surface. The schematic diagram of the experiments is presented in Fig. 3.

The substrate surface was irradiated by a mercury-discharge lamp PRK-4 (Russia, (nominal power of optical radiation 220 W, spectral UV range 180-400 nm) with exposure time up to 40 min for the distance between the lamp and the substrate ~ 20 cm, half of the substrate being shielded. The samples were illuminated by a full-spectrum light of the lamp, as well as by sections of the spectrum isolated by color filters. After irradiation, several water drops of the same volume (~$1.5 \cdot 10^{-3}$ µcL) on the substrate were recorded by a digital photo camera. Similar measurements were made using the conventional method.

The bulk of experiments were done using the fixed drop volume method as it appeared to fit well the purpose of our study. This method is an express one, enables to directly compare results of surface treatment, makes it possible to visually see the non-uniformity and anisotropy of wetting, requires no unique equipment and can be used in any laboratory. Results of the

series of experiments revealed that hydrophilicity increased substantially (fig. 4) under illumination by full-spectrum light for all the three materials. Wettability of the PMMA exposed to UV radiation became comparable to the wettability of glass, and its contact angle changed due to treatment from ~ 60° to ~35°.
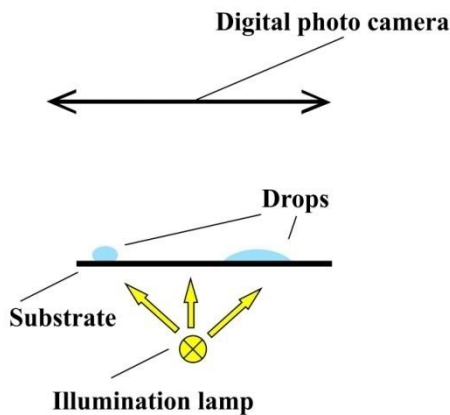
FIG.3. SCHEMATIC DIAGRAM OF DROP PARAMETERS MEASUREMENTS AT FIXED DROP VOLUME
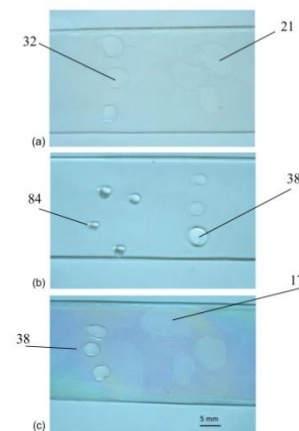
FIG. 4. WATER DROPS ON SILICATE GLASS (A), PMMA (B) AND TiO$_2$ FILM (ANATAZE) (C): LEFT – BEFORE UV IRRADIATION, RIGHT – AFTER UV IRRADIATION. NUMBERS SHOW CONTACT ANGLE IN DEG. CALCULATED FROM EQ. (1a)

Note that the UV-exposed TiO$_2$ film wettability increased most of all (superhydrophilicity [3, 4]), and characterization of wetting by the contact angle only is not enough. The diameter variation and asymmetry of drops (especially at large hydrophilicity) are seen in Figs. 4a and 4c, indicating inhomogeneity and anisotropy of wetting.

A more detailed study of PMMA hydrophilicity with isolation of dedicated spectral sections, more exactly, when the shortwave section shorter than 240 nm was cut off, did not reveal any significant increase of wettability. This fact shows that the radiation at the wavelength less than 240 nm influences PMMA hydrophilicity only.

4.2 Comparative study of the effect of UV irradiation on PMMA wetting by different methods

Results of the experiments on measuring the dependence of PMMA wettability contact angle on the time of exposure to full-spectrum lamp PRK 4 using the conventional method are shown in fig. 5 for two distances (11 and 21 cm) from the sample to the lamp. The contact angle was measured conventionally by making lateral photos of a drop having volume ~ 1.5·10^{-3} mL by a digital photo camera. Each point in fig. 5 corresponds to an individual sample averaged by 5 drops. Comparing data Fig.5 and Fig. 4 for PMMA it is seen that the modified and "classic" methods give practically the same results.

FIG. 5. DEPENDENCE OF CONTACT ANGLE OF H$_2$O ON PMMA ON UV EXPOSURE TIME. 1 AND 2 – DISTANCE BETWEEN LAMP AND SUBSTRATE WAS 11 cm AND 21 cm, RESPECTIVELY.

4.3   The effect of UV laser irradiation on PMMA wetting

To clear the question about the nature of UV hydrophilization of PMMA, we have carried out a comparative study of PMMA wetting after exposure to UV laser radiation (2^d, 3^d, 4th and 5th harmonics of YAG:Nd^{+3} laser, λ=213 nm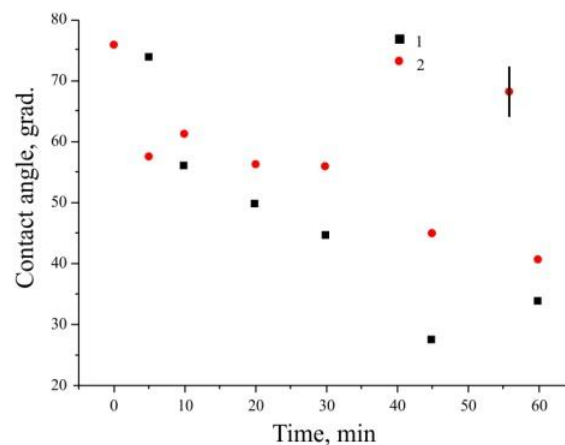 LS-2211N laser operating at a zero-order single transverse mode and with the 5th harmonic converter HG5) in laboratory and argon atmosphere. Wettability was investigated, as described earlier, by the modified method, using fixed drop volume. Irradiation was performed in a flow-through gas (Ar) cell with hermetic optical quartz windows. During irradiation in laboratory atmosphere, Ar was shut off and the windows were opened slightly to retain the irradiation dose.

The irradiation by the 2^d, 3^d and 4th harmonics had no effect on PMMA wetting. The 5th harmonic irradiation showed wetting enhancement only. The results of the series of experiments demonstrate that the drops placed on irradiated areas in Ar atmosphere do not spread, in contrast to the drop placed in the area irradiated in the presence of oxygen (Fig. 6). It means that the wettability rises under UV irradiation in the presence of oxygen only.

FIG. 6. TYPICAL SHAPE OF WATER DROPS ON UV IRRADIATED PMMA SURFACE. THE IRRADIATED AREA IS ENCIRCLED: LEFT – LABORATORY ATMOSPHERE, RIGHT – ARGON ATMOSPHERE. AVERAGE POWER OF UV IRRADIATION 20 mW/cm^2, IRRADIATION DOSE ~ 4.8 J/cm^2.

V.   WETTABILITY OF PMMA AFTER TREATMENT WITH CHLOROFORM VAPOR

In the literature, the processing of PMMA surfaces in chloroform vapor, which is a strong solvent for PMMA, is known [5, 6]. With this treatment, "smoothing" of the surface with a noticeable decrease in micro-roughness was observed. It is useful to investigate the effect of such treatment on the hydrophilicity of the surface. The scheme of the experiments carried out for this purpose is shown in Fig. 7. The PMMA substrate was placed on a chemical beaker with chloroform, so that only the central part of the substrate overlapped. The temperature of chloroform is ~ 30°C. The holding time is about a minute. Then, drops of water were applied to the areas treated and untreated in pairs, which, as before, were photographed. An example of the resulting picture is shown in Fig. 8. As in the case of UV treatment, it is evident that the droplet diameter on the treated surface is on average much larger than on the untreated surface. This indicates greater wettability on the treated part. The spread of diameters, apparently, is the result of surface wettability inhomogeneity, appeared after vaporization
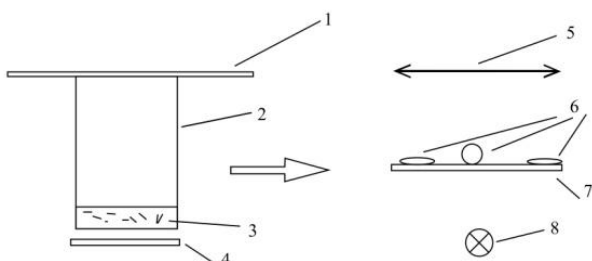

FIG. 7. SCHEME OF THE STUDY OF THE EFFECT OF CHLOROFORM VAPOR ON THE HYDROPHILICITY OF SAMPLES. 1-PMMA PLATE, 2-BEAKER, 3-CHLOROFORM, 4- HEATER; 5-CAMERA, 6 –DROPS, 7 – ILLUMINATOR

FIG. 8. WATER DROPLETS ON PMMA AFTER TREATMENT IN CHLOROFORM VAPOR. LEFT - UNTREATED AREA,   RIGHT - PROCESSED

VI. DISCUSSION AND RESULTS

For investigation of the influence of UV treatment on hydrophilicity of some materials, we used the modified method of measuring the contact angle of a drop on surface that had been specially elaborated by us. Measurements were made by determining the diameter of the drop of known volume from top-view images. The measurements were done, as a rule, in express, comparative regime to maintain equal conditions for drops applied on substrate parts prepared in an individual manner. To compare the methods, investigations were also performed for PMMA using the conventional method of measuring the contact angle from a side-view image of the drop. Results of the comparison show that the modified method permits to obtain the same results in an express manner using apparatuses of common use only. Moreover, the modified method is able to provide additional information, for example, on anisotropy, homogeneity and kinetics of wetting. The results obtained by this method may be significantly more important in some cases, in particular, for the case of superhydrophilicity, when the value of drop surface is more informative than the contact angle. Note, in case of TiO_2 (Fig. 4c) the height of the drop is ~10 μcm, and the conventional measurement of contact angle is not effective.

During comparison of the methods, new information on the possibility of UV PMMA hydrophilization and its nature was obtained. It was shown in experiment that a PMMA surface may be hydrophilized significantly by exposure to UV radiation. It was also demonstrated that the section of the spectrum shorter than 240 nm is responsible for the increase of wettability, in particular, the 5th harmonic irradiation is effective for PMMA wetting. It was shown that UVA is connected with oxygen.

It is well known [7] that photo-oxidation of polymers results in formation of multiple hydroxyl groups. The establishment of hydrogen bonds between these groups within the superficial layers of polymer and the water molecules would lead to wettability enhancement. The significance of photo-oxidation in the process of photodestruction of PMMA irradiated by the fifth harmonic of a neodymium laser was demonstrated experimentally in [8]. Therefore we explain the increase in PMMA wettability due to UVA by surface photo-oxidation.

The information on PMMA UVA is of interest for nanosphere lithography [9,10] especially.

Additionally, the possibility of PMMA hydrophylization in chloroform vapor was shown. This effect can be connected with decomposition and volatilization of surface organic contaminations [11].

All presented quantitative results on contact angle were obtained in the spherical drop approximation (as the majority of results in the literature [1,2]). If greater precision is needed, the modified method can be generalized to account for the effect of, for example, gravity on the drop shape [2,12].

VII. CONCLUSION

A modified express method of contact angle measurement based on determining the diameter of a drop with a known volume has been elaborated. The method offers a number of advantages: it can be used in an express manner for in situ dynamic investigation and makes it possible to observe inhomogeneity and anisotropy of hydrophilicity. The method is convenient in comparative measurements and does not require any special equipment.

Using the proposed method, the possibility of hydrophilic control of some materials (silicate glass, TiO_2 (anataze) and PMMA) by UV and chloroform vapor treatment has been studied. In particular, it is shown that the change in PMMA hydrophilicity during UVA process is connected with the surface oxidation of PMMA. The revealed possibility of hydrophilicity control can be used in various technologies, such as liquid coating, printing, spray quenching, nanolithography, pharmacology and others.

REFERENCES

[1] Kwok D.Y., Neumann A.W. Contact angle measurement and contact angle interpretation. Advances in Colloid and Interface Science, **1999,** 81, 167-249.

[2] Yuehua Yuan and Randall Lee T. Contact Angle and Wetting Properties. In Surface Science Techniques, Springer Series in Surface Sciences; G. Bracco, B. Holst, Eds.; Springer-Verlag, Berlin, Heidelberg, **2013**, 51, 3-34; DOI 10.1007/978-3-642-34243-1_1; http://www.springer.com/978-3-642-34242-4.

[3] Takeuchi M, Sakamoto K, Martra G, Coluccia S, Anpo M. Mechanism of photoinduced superhydrophilicity on the TiO_2 photocatalyst surface. J. Phys. Chem. B, **2005**, 109(32):15422.

[4] Bredikhin V. I., Burenina V. N., Mamayev Yu. A. and Yashin S. N., Spectral and relaxation properties of the photoconductivity of thin TiO_2 films produced by the sol-gel technique. Physical Review & Research International, 2013, 3(4), 642-665. DOI : 10.9734/prri/2013/4253.

[5] De Marco C., Eaton S. M., Martinez R. . Solvent vapor treatment controls surface wettability in PMMA femtosecond-laser-ablated microchannels. Microfluid Nanofluid, **2013**, 14, 171-176.

[6] Ogilvie I.R.G., Sieben V.J. et al Reduction of surface roughness for optical quality microfluidic devices in PMMA and COC. J. Micromech. Microeng.*,* **2010,** 20(6):065016.

[7] B. Ranby, J.F. Rabek. Photodegradation, Photo-Oxidation and Photostabilization of Polymers*;* Willey-Interscience Publication, London, New York, Sydney, Toronto, **1975**.

[8] Bityurin N., Muraviov S., Alexandrov A., Malyshev A. UV laser modifications and etching of polymer films (PMMA) below ablation threshold. Appl. Surf. Sci.*,* **1997**, 110, 270-275.

[9] Bityurin N., Afanasiev A., Bredikhin V., Alexandrov A., Agareva N., Pikulin A., Ilyakov I., Shishkin B., and Akhmedzhanov R. Colloidal particle lens arrays-assisted nano-patterning by harmonics of a femtosecond laser. Optics Express **2013**, 21 (18), 21485-21490.

[10] Afanasiev Andrei, Bredikhin Vladimir, Pikulin Alexander, Ilyakov Igor, Shishkin Boris, Akhmedzhanov Rinat, Bityurin Nikita. Two-color beam improvement of the colloidal particle lens array assisted surface nanostructuring. Applied Physics Letters, **2015**, 106, 1831021–1831024.

[11] J.R. Vig, Ultraviolet-ozone cleaning of semiconductor surfaces, research and development, Technical Report SCLET-TR-91-33 (Rev.1), Army Research Laboratory, NJ 07703-5601, U.S.A., 1992.

[12] Matyukhin, S. I. and Frolenkov, K. Yu. Forma kapel zhidkosti, pomeschennykh na tverduyu gorizontalnuyu poverhnost [Shape of liquid drops, placed on a solid horizontal surface]. Kondensirovannyie sredy i mezhfazniye granitsy [Condensed matters and interphase borders, **2013**, 15(3), 292-304. (In Russian).

Enlargement of Amanatun, South Central Timor Regency

Jarot Soleman Ndaong[1], Surjono[2], I Nyoman Suluh Wijaya[3]

[1]Magister Program of Regional and City Planning Department, Engineering Faculty, Brawijaya University
[2,3]Regional and City Planning Department, Engineering Faculty, Brawijaya University

Abstract— *South Central Timor Regency is one of the Regency within the Province of East Nusa Tenggara. It lies on 3955,36 km2 with 32 Sub-Districts and population of 459.310 people which made it as Regency with most Kecamatan (Sub-District) and most populated area in Province of East Nusa Tenggara. Thus, due it its large size, less optimum service of regional government regarding might occur. One solution offered for this issue was regional enlargement, which become the proposed enlargement of Amanatun. Amanatun was taken from the name of a kingdom during West Indies governance, which was includes in Afdeeling (Regency) South Central Timor. This proposition of Amanatun enlargement was having its own background that became the trigger and objectives of the people who desire this enlargement. Objectives of this study was to discover the triggers and objectives expected from Amanatun enlargement and whether there was relationship between the trigger and objectives of Amanatun enlargement also what is the form of this enlargement according to the prevails laws and regulations. Analysis process was using Partial Least Square (PLS) and appropriateness level for enlargement was based on government regulation guidelines.*

Keywords— *regional enlargement, trigger, objectives, relationship between effect of trigger toward objectives of enlargement, PLS, appropriateness level of enlargement based on laws and regulations.*

I. INTRODUCTION

Regional development in Indonesia particularly regional enlargement started to flourish after 1998. Since there was the change from centralized to decentralization (autonomy), a region could be developed and become independent. This was supported by policy regulating about regional government such as UU 22 of 1999 with PP 129 of 2000 replaced with UU 32 of 2004 with PP 78 of 2007 and UU 23 of 2014.

There were various aspect which affect regional enlargement in Indonesia, such as religious differences, ethnic/cultural differences, development imbalances, vastness of regional area, political factor either regarding power or political representation within regional government also the existence of regional fiscal fund. Regional enlargement was aimed to improve community's welfare such as giving optimum service for citizen, development of local potential so that it would increase economic growth, opened more employment sector, lessened disparity between central and regional, regional potential can be managed in good and faster manner, improved safety and order, also better relationship between central and regional government.

Regarding issue and plans concerning regional enlargement developed in TTS Regency since 2013 until date, author would like to conduct review about the proposed enlargement, started with answering questions such as what triggers this enlargement and what are the objectives to achieved also what is the form of enlargement based on the prevails laws and regulations.

Study site was located in South Central Timor Regency. Its population in 2016 was 443.111 people, and by far is the most populated area compared to other Regency in the Province of NTT. From number of Sub-Districts, TTS Regency has 32 sub-districts and thus known as Regency with the most sub-districts in the Province of NTT. This might the reason behind less optimum service for its citizen. Enlargement plan of Amanatun consist of 8 sub-districts (Amanatun Utara, Amanatun Selatan, Boking, Toianas, Nunkolo, Kokbaun, Santian and Noebana).
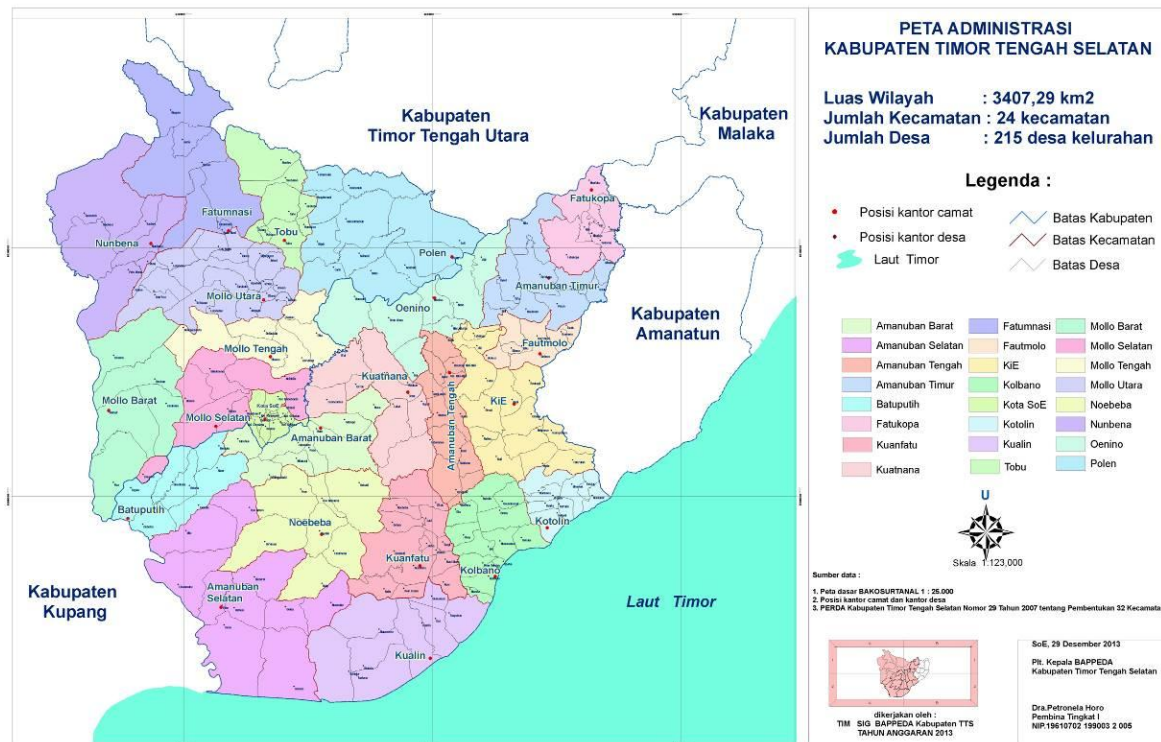
FIGURE 1. SOUTH CENTRAL TIMOR REGENCY (AFTER AMANATUN ENLARGEMENT)

II.   MATERIALS AND METHODS

This study is a quantitative descriptive study with *Partial Least Square* (PLS) approach, with purposive sampling and Likert scale as its sample collection technique. Gravimetric and quota method in calculating the appropriateness of Amanatun enlargement was based on Government Regulation (*Peraturan Pemerintah)* No 78 of 2007. Formulation of study variables was used as the main reference to answer problematic questions and act as basic reference for analysis processing.

TABLE 1
STUDY VARIABLES

No	Objectives	Variables	Sub Variables
1.	Discover the trigger of Amanatun enlargement	Trigger of enlargement	• Religious differences • Ethnic/cultural differences • Economic imbalances • Vastness of regional area • Political reason • Fiscal fund allocation
2.	Discover the objectives of Amanatun enlargement	Objectives of enlargement	• Improved service for citizen • Faster growth in democratic life • Faster regional development • Labor absorption • Faster regional potential management • Improved safety and order • Improved harmony relationship between central and regional
3.	Discover the effect of the trigger toward the objectives of enlargement	Trigger and Objectives	Hypothetical test
4.	Discover the appropriateness of Amanatun enlargement based on the existed UUs and PPs.	PP 78 of 2007	Appropriateness Level of Amanatun Enlargement

Source: Referential Compilation

2.1   Data Collection Method

Data collection method used in this study was through primary and secondary survey. Primary survey was done through observation, interview and questionnaire dispersion. Number of respondent in this study were 40 respondents with purposive sampling approach in which respondent was selected under consideration that he or she was informed and involved in the process of Amanatun enlargement. Secondary survey was done by collecting data related with Amanatun enlargement.

2.2   Data Analysis Technique

In analyzing the trigger of enlargement, objectives of enlargement and relationship/effect of the trigger toward the objectives of Amanatun enlargement, we use Partial Least Square (PLS) analysis with sample collection technique using purposive sampling, under the consideration that sample determination was taken from:

- Unknown population

- Not all people involved in Amanatun enlargement

- Minimum samples in PLS is 30-100

Number of respondents in this study was 40 respondents, in which they were asked to answer the questions by using Likert scale. Likert scale was used to find social symptom and event occurs among people by measuring perception, attitude and opinion of individuals within community, whereas variables would be made into sub-variables and then used as measurable indicators (Sugiyono, 2012). PLS analysis is part of Structural Equation Modelling (Ghozali, 2014). Several benefits of PLS are:

- Distribution free approach

- PLS objective is to predict or to developed a theory

- Small sample (30-100 samples)

- Indicator was reflective and formative

- It can be used as an alternative for structure equation modelling which has weak theory

- PLS can be used for theoretical testing and also can be used for exploratory or to test relationship which has no theory of it.

- PLS is using SmartPLS and VisualPLS softwares.

Steps in PLS consist of:
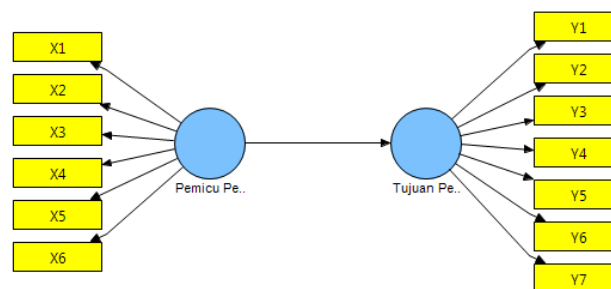
Step 1: Creating a path diagram

FIGURE 2: PATH DIAGRAM MODEL OF PLS WITH *SMARTPLS 3.0 SOFTWARE*

Step 2: Conversion of path diagram into structural model

a.   Struktural model *(inner model)*

b.   Measurement model *(outer model)*

Step 3: Conduct *Godness of Fit* evaluation

c.   Evaluation of measurement model

d.   Evaluation of structural model

Step 4: Hypothetical testing (Interpretation)

Hypothetical testing in PLS was using T-test or *t-statistic* and *p-values*.

TABLE 2
VARIABLES IN PLS MODEL

No	Latent Variables	Manifested Variables (Indicator)
1.	Objective of Enlargement (Y)	Y1 = Improved service for citizen
		Y2 = Faster democratic growth for citizen
		Y3 = Faster regional economic development
		Y4 = Labor absorption
		Y5= Faster management concerning regional's potential
		Y6 = Improved safety and order in regional area
		Y6 = Faster management concerning regional's potential
		Y6 = Improved safety and order in regional area
		Y7 = Improved relationship between central and regional government and vice versa
2.	Trigger of Enlargement (X)	X1 = Religious differences
		X2 = Ethnic/cultural differences
		X3 = Economic imbalances
		X4 = Vastness area of regional
		X5 = Political reason
		X6 = Fiscal fund allocation

Source : Analysis result

For enlargement analysis based on PP 78 of 2007, quota and gravimetric analysis was used to determine the appropriateness of regional enlargement.

III.   RESULT AND DISCUSSION

3.1   Partial Least Square (PLS) Analysis

PLS analysis was using *SmartPLS 3.0 software*. Steps in this PLS analysis were:

3.1.1   Constructing path diagram

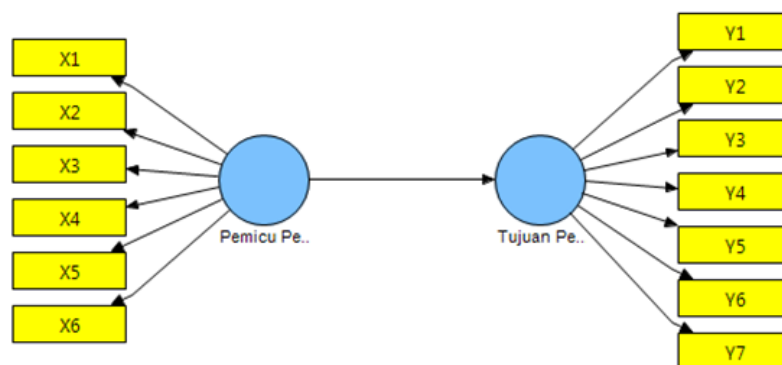**FIGURE 3. PATH DIAGRAM OF PLS**

3.1.2   Conversion of path diagram into equation system

a.   Structural model *(inner model)*

$$Y = \gamma X + \varsigma$$

b.   Measurement model *(outer model)*

i.   Variabel X (reflektive)

$$X1 = \lambda y \ X + \xi 1$$
$$X2 = \lambda y \ X + \xi 2$$
$$X3 = \lambda y \ X + \xi 3$$
$$X4 = \lambda y \ X + \xi 4$$
$$X5 = \lambda y \ X + \xi 5$$
$$X6 = \lambda y \ X + \xi 6$$

ii.   Variabel Y (reflektive)

$$Y1 = \lambda y \ Y + \xi 1$$
$$Y2 = \lambda y \ Y + \xi 2$$
$$Y3 = \lambda y \ Y + \xi 3$$
$$Y4 = \lambda y \ Y + \xi 4$$
$$Y5 = \lambda y \ Y + \xi 5$$
$$Y6 = \lambda y \ Y + \xi 6$$
$$Y7 = \lambda y \ Y + \xi 7$$

3.1.3   Conduct Goodness of Fit evaluation

Goodness of Fit evaluation was done to find out model's appropriateness, either for measurement model (outer model) and structural model (inner model).

a.   Evaluation of measurement model (outer model)

For evaluation of measurement model (outer model), we used PLS with validity and reliability test, validity test were convergent validity and discriminant validity. Convergent validity was determined by outer loadings value > 0,5
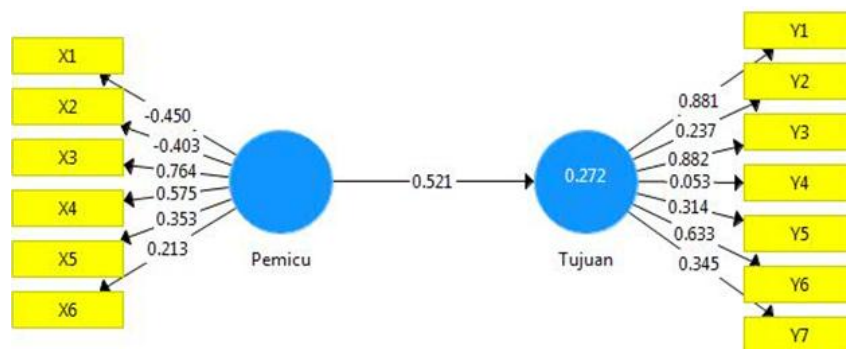
FIGURE 4. CALCULATION RESULT FOR *PLS ALGORITHM*

TABLE 3
LOADINGS VALUE BETWEEN INDICATORS

Variables		Nilai Loading	Keterangan
X (Trigger of Enlargement)	X1	-0.450	Insignificant
	X2	-0.403	Insignificant
	X3	0.764	Valid and significant
	X4	0.575	Valid and significant
	X5	0.353	Insignificant
	X6	0.213	Insignificant
Y (Objective of Enlargement)	Y1	0.881	Valid and significant
	Y2	0.237	Insignificant
	Y3	0.882	Valid and significant
	Y4	0.053	Insignificant
	Y5	0.314	Insignificant
	Y6	0.633	Valid and significant
	Y7	0.345	Insignificant

Source : SmartPLS processing results

From *PLS Algorithm* results, indicators X1, X2, X4, X5, X6, Y2, Y4, Y5, Y6 and Y7 were omitted because it has *loading value* less than 0.5 and insignificant. After omission completed, it was recalculated.

FIGURE 5. RECALCULATION RESULT FOR *PLS ALGORITHM*

TABLE 4
LOADING VALUES AND VARIANCE INFLATION FACTOR (VIF) BETWEEN INDICATORS

Variables		loadingValue	VIF Value	Information
X (Trigger of Enlargemen)	X3	0.897	1.145	Valid and significant
	X4	0.732	1.145	Valid and significant
Y (Tujuan Pemekaran)	Y1	0.920	2.034	Valid and significant
	Y3	0.890	1.995	Valid and significant
	Y6	0.652	1.358	Valid and significant

Source : SmartPLS processed results

From the table above it can be seen that *loading value* of each indicator was above 0.5 and its *variance inflation factor* (VIF) value was >0.1 and <10. For *discriminant validity*, it can be seen by looking at *cross loading* correlation value of indicator with its construct and its *average variance extracted* (AVE) of each construct whereas good model would have AVE value of its construct >0.50. *Cross loading value* in this model can be seen from table below.
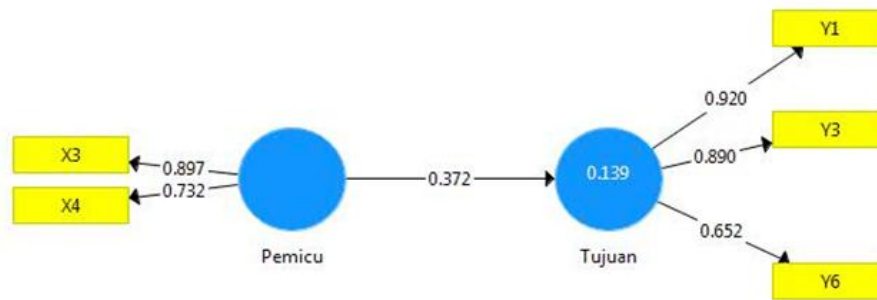
TABLE 5
***CROSS LOADING* VALUES**

	X (trigger)	Y (objective)
X3	0.897	0.359
X4	0.732	0.233
Y1	0.386	0.920
Y3	0.323	0.890
Y6	0.146	0.652

Source: SmartPLS processing result

From the table above, it can be seen that *cross loading* value of trigger variables with its indicators (X3, X4) was higher than objective variables. The opposite also occur in which *cross loading* value of objective variables with its indicators (Y1, Y3 and Y6) was higher than trigger variables. This indicated that manifested variables value of its latent variables has better prediction. AVE values for each variable can be viewed in the table below.

TABLE 6
***AVERAGE VARIANCE EXTRACTED* (AVE) VALUES**

Variables	Average variance extracted (AVE)
Trigger of Enlargement	0.670
Objective of Enlargement	0.688

Source : SmartPLS processing result

From the table above it can be seen that AVE value for each construct was above 0.5, it means that the construct is valid. Reliability test was using *composite reliability value (pc) > 0.7*.

TABLE 7
***COMPOSITE RELIABILITY* VALUES**

Variables	Composite reliability	Information
Trigger of Enlargement	0.801	Reliable
Objective of Enlargement	0.866	Reliable

Source : SmartPLS processing result

From the table above, it can be concluded that for both trigger of enlargement and objective of enlargement variables it has *composite reliability* value >0.7 thus indicators used in these variables (X3, X4, Y1, Y3 and Y6) has good reliability or able to measure its construct. Therefore, measurement model *(outer model)* can be written as follows:

X3 = 0.897 Trigger + 1.145
X4 = 0.732 Trigger + 1.145
Y1 = 0.920 Objective + 2.034
Y3 = 0.890 Objective + 1.995
Y6 = 0.652 Objective + 1.358

b.   Evaluation of structural model (inner model)

Testing toward structural model was done by looking at its *R-sqaure* and *Q-square* value with range $0<Q^2<1$, whereas closer to 1 means better model. For *R-square* and *Q-square* values, it was shown in Table 8.

TABLE 8
***R-SQUARE* AND *Q-SQUARE* VALUES**

	R Square	Q Square
Objective of Enlargement	0.139	0.139

Source : SmartPLS processing result

From the table above, it can be seen that *R-square* and *Q-square* values were > 0 which means that model was also fit with the data or able to convey the phenomenon on the field. Structural model *(inner model)* can be written:

$Y = \gamma X + \varsigma$

Objective of Enlargement (Y1,Y3,Y6) = 0.372 Trigger of Enlargement (X3,X4) + 1

3.1.4 Hypothesis Testing

Hypothesis testing in PLS was done by *resampling bootstrapping* method using *T-statistic*. The hypothesis was "there is triggering effect of enlargement toward objective of enlargement in Amanatun".

H0 : = 0 (there is no relationship/effect)

Ha : ≠ 0 (there is relationship/effect)

Result of T-test in PLS can be seen from table below:

TABLE 9
MEAN, STDEV, T-VALUES, P-VALUES

	Original Sample (O)	Sample mean (M)	Standard Deviation (stdev)	T Statistics (O/STDEV)	P Value
Pemicu>tujuan	0,372	0,396	0,184	2,027	0,043

Source : SmartPLS processing result

From the table above it can be seen that *T-statistic* for trigger > objective of enlargement is 2,027. A hypothesis was said to have significant effect/relationship x toward y if *T-statistic* ≥ 1,96 while *P value* is 0,043 which means lower (<) than *alpha* (0,05) and thus null hypothesis was rejected (Ha:≠0). Thus conclusion of this hypothesis testing is there was effect/relationship between trigger of enlargement and objective of enlargement for Amanatun region.

3.2   Analysis of Appropriateness Level based on PP of 2007

In analyzing appropriateness level for Amanatun enlargement using PP 78 of 2007, comparison was conducted between enlargements analyses of Amanatun with other Regency existed in the Province of East Nusa Tenggara.

Based on the appendix of Government Regulation (PP) No 78 of 2007, there were 11 factors and indicators with score range from 1-5,

- Score 5 was in a category of very capable with indicators value requirement ≥ 80% of average value.
- Score 4 was in category of capable with indicators value requirement ≥ 60 % of average value.
- Score 3 was in category of less capable with indicators value requirement ≥ 40% of average value.

- Score 2 was in category of incapable with indicators value requirement ≥ 20 % of average value.
- Score 1 was in category very incapable with indicators value requirement < 20 % of average value.

TABLE 10

ANALYSIS AND SCORING OF INDICATORS FOR AMANATUN ENLARGEMENT BASED ON PP 78 OF 2007

N o	Factors and Indikators	Score		Bob ot	Number	
		Kab.Induk TTS	Amanatun Enlargement		Kab.Induk TTS	Amanatun Enlargement
1.	Demography					
	1. Number of people	5	5	15	75	75
	2. Population density	5	5	5	25	25
	Total Demography score				**100**	**100**
2.	Economy Capability					
	1. Domestic product input for regional gross non oil and gas per capita	5	4	5	25	20
	2. Economy growth	5	5	5	25	25
	3. domestic product input for regional gross non oil and gas	5	3	5	25	15
	Total economy capability score				**75**	**60**
3.	Regional Potential					
	1. Bank ratio	5	2	2	10	4
	2. shopping group ratio / 10.000 citizen	5	5	1	5	5
	3. Market ratio / 10.000 citizen	5	4	1	5	4
	4. Elementary school ratio / citizen eligible for primary school	5	5	1	5	5
	5. Middle school ratio / citizen eligible for secondary school	5	5	1	5	5
	6. High school ratio / citizen eligible for tertiary school	5	5	1	5	5
	7. Rasio Fas.Kesehatan per 10.000 citizen	5	5	1	5	5
	8. Medical personnel ratio	5	4	1	5	4
	9. Motor vehicles	5	4	1	5	4
	10. Electricity subscribers	5	4	1	5	4
	11. Road length / number of vehicles	5	5	1	5	5
	12. High school diploma worker	5	4	1	5	4
	13. Bachelor degree worker	5	3	1	5	3
	14. Civil servant ratio	5	5	1	5	5
	Total Regional Potential Score				**75**	**62**
4.	Financial Capability					
	1. Local income own	5	2	5	25	10
	2. Own revenue to number of citizen ratio	5	5	5	25	25
	3. Own revenue ratio compare to gross regional domestic product	5	5	5	25	25
	Total Financial Capability Score				**75**	**60**
5.	Social Cultural					
	1. Praying facility ratio	5	5	2	10	10
	2. Sport square facility ratio	4	4	2	8	8
	3. Number of city hall	3	2	1	3	2
	Total Social Cultural Score				**21**	**20**
6.	Social Political					
	1. Election percentage	5	5	3	15	15
	2. Number of mass organization	3	2	2	6	4
	Total Social Political Score				**21**	**19**
7.	Vastness of region					
	1. Overall teritorial area	5	1	2	10	2
	2. Effective teritorial area	5	2	3	15	6
	Total Regional Vastness Score				**25**	**8**
8.	Defence					
	1. Defence personnel ratio	5	2	3	15	6
	2. Teritorial characteristic	1	4	2	2	8

N o	Factors and Indikators	Score		Bob ot	Number	
		Kab.Induk TTS	Amanatun Enlargement		Kab.Induk TTS	Amanatun Enlargement
	Total Defence Score				17	14
9.	Security					
	1. Security personnel ratio	5	2	5	25	10
	Total Security Score				25	10
1 0.	People welfare level					
	1. Human development index	5	5	5	25	25
	Total Welfare Score				25	25
1 1.	Control Range					
	1. Average distance	5	5	2	10	10
	2. Average time	5	5	3	15	15
	Total Control Range Score				25	25
	Total Overall Score				484	403

Source : Analysis result

Score for Amanatun enlargement regarding population factor was 100, score for economic capability factor was 60, score for regional potential factor was 62 and score for financial capability factor was 60. It means that it was eligible to conduct regional autonomy. Furthermore, total score for Main area in South Central Timor Regency is 484 and total score for Amanatun enlargement is 403, it means that appropriateness category for this enlargement is capable and recommended to be pursued.

IV.   CONCLUSION

From the analysis result, conclusion can be made:

1. Trigger of Amanatun enlargement is economic imbalances and vastness of regional area.
2. Objective of Amanatun enlargement is to improve service for citizen, accelerating regional economy development and to improve safety and order.
3. Hypothesis testing result indicate that there is 37,2% relation between trigger of enlargement toward objective of enlargement in Amanatun.
4. Based on PP 78 of 2007, enlargement of Amanatun was capable and recommended to be pursued.

V.   SUGGESTIONS

1. For central government, there was no complementary regulation for UU 23 of 2014 particularly regarding regional enlargement and thus implementation for Amanatun enlargement was still unclear.
2. For regional government, review regarding Amanatun enlargement as capital candidate was not yet geographically reviewed particularly for disaster prone areas and one based on hydrography.
3. For subsequent study, this study has give considerable input for Amanatun enlargement plan and also various aspects regarding not yet reviewed UU 23 of 2014.

REFERENCES

[1]   Adisasmita,Rahadjo. 2012. *Analisis Tata Ruang Pembangunan.* Yogyakarta : Graha Ilmu

[2]   Alfirdaus,K & Bayo,L. 2007. *Penataan Daerah Sebagai Penataan Institusi (Territorial Reform as Institutional Building and Reform).* Seminar Internasional PERCIK ke-8

[3]   Arianti,N,N & Cahyadinata,I. 2013. *Kajian Dampak Pemekaran Wilayah Terhadap Kinerja dan Pemeratan Ekonomi Daerah Pesisir di Provinsi Bengkulu.* Laporan Kegiatan Penelitian. Fakultas Pertanian Universitas Bengkulu.

[4]   Badan Perencanaan Pembangunan Nasional bekerja sama dengan United Nation Development Program. 2007, *Studi Evaluasi Pemekaran Daerah.*

[5]   Dirjen Otonomi Daerah, Kemendagri.2011, *Laporan hasil Evaluasi Daerah Otonom Hasil Pemekaran (EDOHP).*

[6]   Gede,N. S, Made.2008. *Pemodelan Persamaan Struktural Dengan Partial Least Square.,* Seminar Nasional Matematika dan Pendidikan Matematika.

[7]   Ghozali,Iman.2014. *Structrural Equation Modeling:Metode Alternatif dengan Partial Least Square.,* Semarang: Badan Penerbit Universitas Diponegoro.

[8]   Ilyas,H,Dr. *Implikasi Pengalihan Sistem Pemerintahan Sentralistik ke Sistem Otonomi Daerah Terhadap NKRI Paska Perubahan UUD 1945*

[9]   Khairullah dan Chayadin,M. 2006. *Evaluasi Pemekaran Wilayah di Indonesia : Studi Kasus Kabupaten Lahat.* Jurnal Ekonomi Pembangunan Vol 11

[10]   Noor,M. 2012. *Memahami Desentralisasi Indonesia.* Yogyakarta : Interpena

[11]   O'Leary, Brendan. 2006, *Analyzing Partition: Definition, Classification and Explanation (Working Paper): Mapping Frontiers, Plotting Pathways Working Paper* No.27.

[12]   Partnership For Governance Reform in Indonesia. 2011. *Desain Besar Penataan Daerah di Indonesia.* Partnership Policy Paper No 1/2011

[13]   Puspitasari,R. 2014. *Faktor-faktor yang Mempengaruhi Pembentukan Daerah Baru (Studi Kelayakan Secara Administratif Kabupaten Indragiri Selatan).* Jom FISIP Vol 1 no 2 – Oktober 2014

[14]   Samosir,P,A. 2013. *Pemekaran Daerah : Kebutuhan atau Euforia Demokrasi ? Mengurangi Regulasi Pemekaran.*

[15]   Sjafrizal.2008.*Ekonomi Regional Teori dan Aplikasi.* Padang : Badouse Media.

[16]   Sugiyono. 2012. *Statistika Untuk Penelitian.* Bandung : Alfabeta

[17]   Tenrini,H,R. 2013. *Pemekaran Daerah : Kebutuhan atau Euforia Demokrasi ? Mengapa Harus Mekar ?.*

[18]   Ulum, Miftahul. Tirta,Made. Anggraeni, Dian. 2014, *Analisis Structural Equation Modeling (SEM) untuk Sampel Kecil dengan Pendekatan Partial Least Square (PLS),*Prosiding Seminar Nasional Matematika: Universitas Jember.

[19]   Yamin, S. dan Kurniawan,H.,2009, *Structural Equation Modeling: Belajar Lebih Mudah Teknik Analisi Data Kuisioner dengan LISREL-PLS,* Buku Seri Kedua, Jakarta:Salemba Infotek.

Comparison of Turbulence Models in the Flow over a Backward-Facing Step

Priscila Pires Araujo[1], André Luiz Tenório Rezende[2]

Department of Mechanical and Materials Engineering, Military Engineering Institute, Rio de Janeiro, Brazil

Abstract—*This work presents the numerical simulation and analysis of the turbulent flow over a two-dimensional channel with a backward-facing step. The computational simulation performed in this study is based on the Reynolds equations using a technique denominated Reynolds Average Navier-Stokes (RANS). The main objective of the present work is the comparison of different models of turbulence applied to the turbulent flow over a backward-facing step. The performance of each RANS model used will be discussed and compared with the results obtained through a direct numerical simulation present in the literature. The RANS turbulence models used are k-ω, k-ε, Shear Stress Transport k-ω (SST k-ω) and the second-order closure model called Reynolds Stress Model (RSM). The Reynolds number used in all the numerical simulations constructed in this study is equal to 9000, based on the height of the step h and the inlet velocity U_b. The results are the reattachment length, the mean velocity profiles and the turbulence intensities profiles. The k-ε model obtained poor results in most of the analyzed variables in this study. Among the RANS turbulence models, the SST k-ω model presented the best results of reattachment length, mean velocity profile and contour when compared to results obtained in the literature. The RSM model found the best results of turbulence intensity profile, when compared to the models of two partial differential equations that use the Boussines hypothesis.*

Keywords—*backward-facing step, DNS, RANS, turbulence models.*

I.   INTRODUCTION

The flow separation caused by an adverse pressure gradient is a common phenomenon in many practical applications in engineering. The adverse pressure gradient is the increase of the static pressure in the direction of the flow, significantly affecting the flow. In several engineering cases, the adverse pressure gradient is caused by a sudden change in geometry, leading to separation of the flow and subsequent reattachment. Such phenomenon can also be observed in devices such as electronic cooling equipment, combustion chambers, diffusers and valves. In this context, the backward-facing step is one of the most studied cases, in order to understand the effects on the flow caused by a sudden change in geometry using a simple geometry. Therefore, it has been much studied in cases of computational simulation, requiring less computational cost than other cases and presenting satisfactory results in the study of phenomena caused by the flow separation.

The present work deals with the computational simulation and analysis of the turbulent flow over a channel with a backward-facing step by means of the construction of a relatively simple geometry with the great advantage of presenting important characteristics for the scope of the study of turbulent flows with boundary layer separation. The simulated cases in the present work are based on the study carried out by [1] using the same geometry as this one, with the objective of validating the obtained results and comparing different turbulence models, analyzing results such as the reattachment length, profiles of mean velocity, pressure coefficient and Reynolds stress components.

II.   MATHEMATICAL MODELING

In this work, the Reynolds Averages Navier-Stokes equations method (RANS) is applied to the government equations shown previously. The method of the average Reynolds equations is based on the decomposition of the velocity instantaneous value in $u_i = \overline{u}_i + u_i'$, where u_i represents the velocity instantaneous value, $\overline{u}_i$ is the mean velocity vector and u_i' represents the velocity fluctuation vector. Therefore, the equations of conservation of mass and conservation of the amount of linear motion obtained by applying the RANS methodology are given by

$$\frac{\partial \overline{u_j}}{\partial x_j} = 0; \quad \frac{\partial \overline{u_i u_j}}{\partial x_j} = g_i - \frac{1}{\rho}\frac{\partial \overline{p}}{\partial x_i} + \frac{\partial}{\partial x_j}\left(\upsilon\frac{\partial \overline{u_i}}{\partial x_j} - \overline{u_i' u_j'}\right) \tag{1}$$

It is observed the appearance of a new term, $\overline{u_i' u_j'}$, denominated Reynolds tensor. The Reynolds tensor can be modeled by an analogy with Stokes law, based on the Boussinesq hypothesis, where the turbulent stresses are proportional to the mean flow velocity gradient, as show in Eq. 2. The constant of proportionality is called turbulent viscosity, υ_t.

$$-\overline{u_i{'}u_j{'}} = \upsilon_t \left(\frac{\partial \overline{u_j}}{\partial x_j} + \frac{\partial \overline{u_i}}{\partial x_i} \right) - \frac{2}{3} k \delta_{ij} \qquad (2)$$

Three turbulence models of two differential equations using the Boussinesq hypothesis approach are used in the present work: k-ε, k-ω e SST k-ω.

The standard k-ε model [3, 4] is the turbulence model of two partial differential equations most commonly used today. In this model an equation for turbulent kinetic energy k and one equation for the dissipation of turbulent kinetic energy per unit mass ε are solved. In the standard k-ε model developed by [3], the equation for turbulent viscosity is given by Eq. 3.

$$\upsilon_t = \frac{C_\mu k^2}{\varepsilon} \qquad (3)$$

The vast use of this model has shown that it has good results for the simulation of simple flow cases, but its most known deficiency is its imprecision close of adverse pressure gradients [5].

In the standard k-ω model an equation for the turbulent kinetic energy k and an equation for the specific rate of dissipation of the turbulent kinetic energy ω are solved. Its rate is determined by the rate of energy transfer over the spectrum of lengths, so ω is defined by the large scales of motion and is closely related to the mean flow properties [6].

The most commonly used k-ω model is called the standard k-ω model, where the turbulent viscosity is given by Eq. 4.

$$\upsilon_t = a^* \frac{k}{\omega} \qquad (4)$$

The standard k-ω model shows good performance for free shear flows and flow on flat plates with boundary layer, as well as for more complex flows with adverse pressure gradients and separate flows. The main negative point of this model is that it presents a strong dependence of the boundary condition on the free current for ω [7, 8].

The SST k-ω model (Shear-Stress Transport k-ω) [9] is widely used in cases with high adverse pressure gradients and boundary layer separation, by means of a combination of k-ε and K-ω turbulence models. The SST k-ω model is the robust and precise combination of the k-ω model in the region near the walls with the independence of the free current of the k-ε model outside the boundary layer. For this, the k-ε model is written in terms of the specific dissipation rate, ω. Then, the standard k-ω model and the modified k-ε model are multiplied by a mixing function and summed [2]. The mixing function F1 is defined as a unite value (considering the standard k-ω model) in the inner region of the turbulent boundary layer and is zero (considering the standard k-ε model) at the outer edge of the layer, given by

$$F_1 = \tanh(\arg_1{}^4); \ \arg_1 = \min\left[\max\left(\frac{\sqrt{k}}{\beta^*\omega d}; \frac{500\upsilon}{d^2\omega}\right); \frac{4\sigma_\omega 2k}{CD_{k\omega} d^2}\right]; \ CD_{k\omega} = \max\left(2\rho\sigma_D \frac{1}{\omega}\frac{\partial k}{\partial x_j}\frac{\partial \omega}{\partial x_j}; 10^{-10}\right) \qquad (5)$$

In this model the turbulent viscosity is formulated through Eq. 6.

$$\upsilon_t = \frac{a_1\omega}{\max(a_1\omega; SF_2)}; \ F_2 = \tanh(\Phi^2); \ \Phi = \max\left(\frac{2\sqrt{k}}{\beta^*\omega d}; \frac{500\upsilon}{d^2\omega}\right) \qquad (6)$$

The turbulent kinetic energy k and the specific dissipation rate ω of this model can be obtained by the solution of its conservation equations, where the closing set ϕ for the SST k-ω are calculated by the use of a mixing function between the constants ϕ1 , of the standard k-ω model and ϕ2 of the model k-ε, making $\phi = F_1\phi_1 + (1 - F_1)\phi_2$.

The models discussed above are RANS models based on the Boussinesq Hypothesis. These models present a good solution to the problem of turbulence closure, but they present some faults, generally related to the limitations imposed by the concept of turbulent viscosity. The RSM model (Reynolds Stress Model) is an alternative to the models shown, based on the determination of direct equations for Reynolds transport. The RSM model is usually referred to as the direct closure model or the second order model. The transport equations for the Reynolds stress can be determined by the Navier-Stokes equations and are given by the Eq. 7.

$$\frac{\partial \overline{u'_i u'_j}}{\partial t} + \frac{\partial \overline{u'_i u'_j u_l}}{\partial x_l} = D_{ij} + P_{ij} + \Phi_{ij} - \varepsilon_{ij} \qquad (7)$$

The left side of Eq. 7 concerns the convective transport of the Reynolds tensor over the average flow. The first term on the right side is called diffusive transport term, the term P_{ij} is the term of stress production, Φ_{ij} is the pressure term and the term ε_{ij} refers to the dissipation rate of the Reynolds tensor caused by the viscosity.

III.   METHODOLOGY

All cases constructed in the present work have the same geometry, with an expansion ratio $E_R = 2$. The expansion ratio refers to the relation between the height of the outlet channel (L_y) and the height of the step (h), given by $E_R = L_y/(L_y - h)$. The inlet channel has a width of 4h and height equal to h and the outlet channel has width 29h and height 2h. In the simulations performed in the current study, the value of h used is 1 m. Fig. 1 shows the constructed geometry.
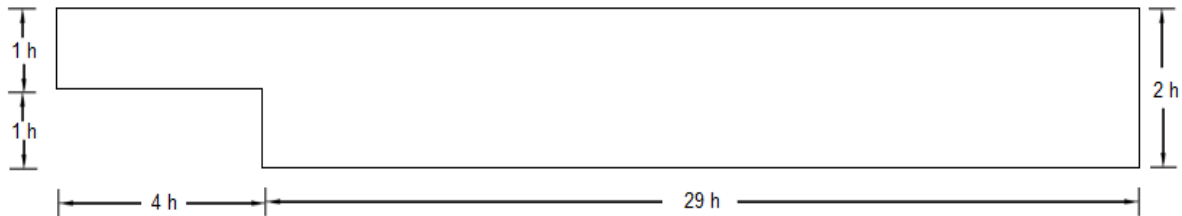

FIGURE 1. GEOMETRY BUILT.

The Reynolds number is defined by the step height, the kinematic viscosity of the fluid and the mean inlet velocity, given by $Re = U_b h/\upsilon$. The Reynolds number used in the cases constructed in the current work is Re = 9000. The mean inlet velocity set is equal to 1 m/s. The top and bottom wall regions present wall boundary conditions with the non-slip condition on the wall. The outlet region has a gauge pressure equal to zero. The mesh constructed and used in all simulated cases has 155000 elements and 156751 nodes. The region near the step received a treatment of most refined mesh, being the region of greater interest of the study realized.

The numerical method called Finite Volume Method [10] was used to discretize the equations of government. The interpolation scheme chosen for the simulations was QUICK [11] and the SIMPLE scheme [12] was used in the velocity-pressure coupling. The Multigrid technique [13] was chosen to solve the system of linear equations. The problem was considered converged when all residues were less than 10^{-6}. ANSYS FLUENT® software was used for geometry construction, mesh construction, support for numerical methods and government equations, and post-processing of built cases.

IV.   RESULTS AND DISCUSSION

The reattachment length (X_R) refers to the position where, after separation and recirculation of the flow, the reattachment happens. It is an important quantity being analyzed in the flow on a backward-facing step. Tab. 1 presents the values of reattachment length obtained in each of the cases analyzed.

TABLE 1
REATTACHMENT LENGTHS.

Case	X_R
DNS [1]	8.62
k-ω	9.83
k-ε	6.34
SST k-ω	8.50
RSM	5.86

When analyzing the Tab. 1, it is noted that the k-ω model overestimates the value of the reattachment length and the k-ε model has a significantly short reattachment length when compared to the result found in the DNS case. The SST k-ω model, as discussed above, is a RANS turbulence model recommended for cases with adverse pressure gradient and flow separation, addressing the advantages of k-ω and k-ε models. This model presents a better treatment in the regions close to the wall than the other RANS models treated in this case, thus, it was expected that this model would obtain the best result of reattachment length. The RSM model is the model that presents the lowest value of reattachment length. In spite of being a second-order closure model and solving the government equations directly, this model does not present a good treatment for the regions near the wall, which justifies the poor result for the value of reattachment length, measured in wall of the channel.

The velocity profiles were analyzed in four different flow positions, obtained in the simulations with the RANS models and compared with the results obtained by [1]. Fig. 2 presents the velocity profiles in the following positions: x/h = 0.5, x/h = 4, x/h = 8 and x/h = 20.
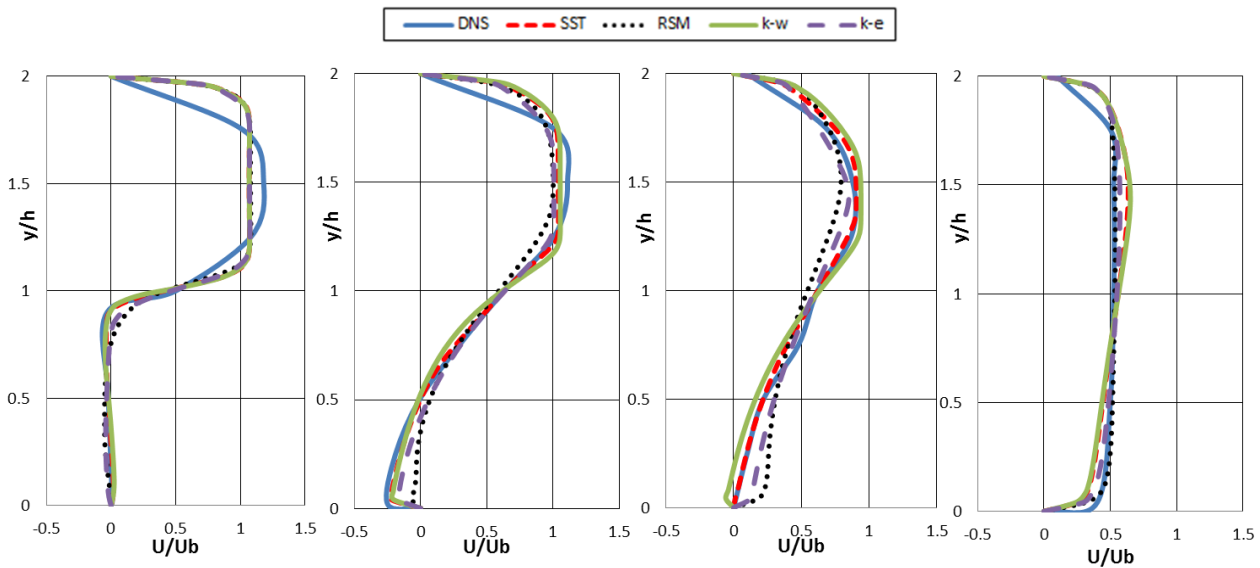

FIGURE 2. VELOCITY PROFILES AT FOUR POSITIONS.

The first position is located just after the step and it can be seen that the fully developed flow extends freely in all cases shown in Fig. 2. In x/h = 4, where the recirculation occurs, it is noted that there are negative values of velocity in the region near the bottom wall in all cases simulated in this work, as well as in the result found for the DNS case. The negative velocity values are due to the flow separation and represent the presence of inverse flow in the recirculation zone. In this position it can be observed that the velocity values near the bottom wall found with the RSM model are higher than the values obtained by the other models analyzed. Consequently, the presence of reverse flow is lower in this position for the case simulated with the RSM model. This result is explained by the fact that the reattachment length of the RSM model is considerably smaller than the reattachment length of the others turbulence models analyzed, so in the position x/h = 4 the reattachment is closer in the RSM model case. When comparing the velocity profile of k-ε model with the profiles found by k-ω, SST k-ω and DNS models, it is also possible to observe that the velocity values of this model are larger than the others since the reattachment occurs before in the k-ε model. In the position x/h = 8, it is observed that the model k-ω is the only one that presents negative values of velocity. The presence of the inverse flow in this position was already expected for this model, since the reattachment length of the k-ω model is the largest among the analyzed models, with a value equal to x/h = 9.83, while in the other models, has already occurred or is about to happen. It is also noted that the models RSM and k-ε present the highest velocity values in the region near the bottom wall, a result justified by the fact that in both models the reattachment has already happened, while it is close to occurring in the SST k-ω and DNS models. In x/h = 20 it can be observed that, although not fully developed, the flow tends to equilibrium and the velocity profiles of all models behave in a similar way.

Are analyzed the velocity profiles u^+ as a function of y^+. The term u^+ is the velocity u normalized by the friction velocity, uτ. The friction velocity is obtained as a function of the wall shear stress, τ_w, and the specific mass of the fluid. These terms and the term y+ are given below.

$$u^+ = \frac{u}{u_\tau}; \; y^+ = \frac{u_\tau}{\nu} y; \; u_\tau = \sqrt{\frac{\tau_w}{\rho}} \tag{8}$$

For all positions that the u+ profiles were obtained numerically the theoretical curve of the wall law for the laminar boundary layer and the logarithmic region was also constructed in order to compare the results found by each turbulence model with the expected results by theory. The curve for the region of the laminar boundary layer is created according to the relation $u^+ = y^+$, while the logarithmic region profile, called log, is constructed by means of $u^+ = 2,5 \ln y^+ + 5$. Fig. 3 show the velocity profiles u^+ obtained by the numerical simulations performed with different turbulence models at four different flow positions: x/h = 14, x h = 18, x/h = 26 and x/h = 28.

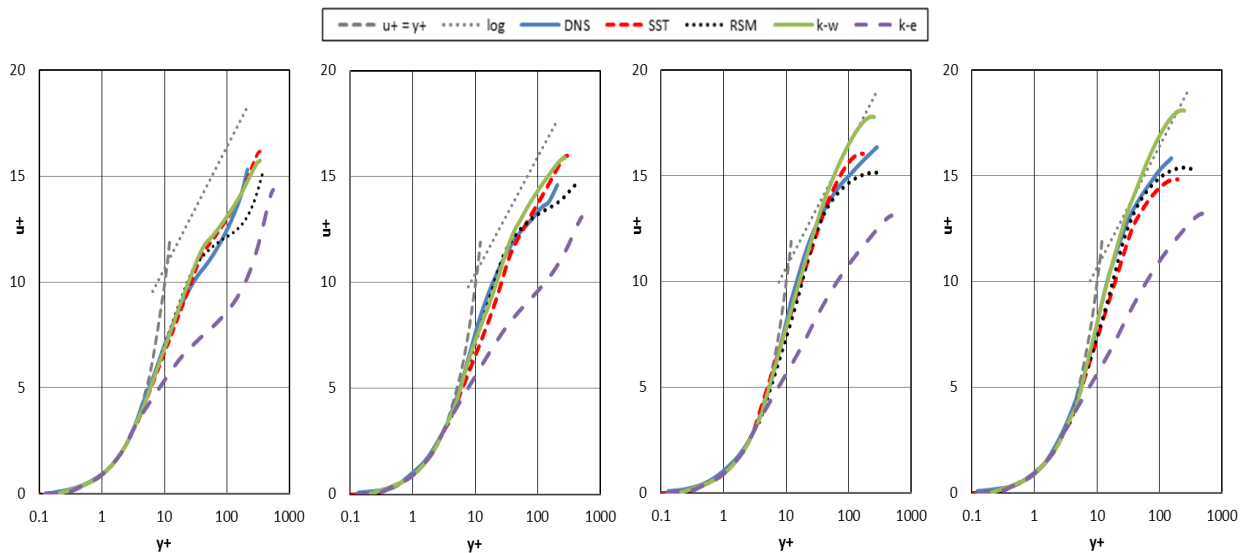**FIGURE 3. VELOCITY PROFILE u^+ AT DIFFERENT POSITIONS.**

By analyzing the u^+ velocity profiles found, it can be observed that insofar as the flow occurs the results obtained by the turbulence models discussed in the present work become closer to the results obtained by means of the theoretical curves of the law of the wall. In addition, further downstream the velocity profile tends to the fully developed velocity profile, which is not fully achieved even at long distances for the case of the descending rung. It should be noted that all the RANS turbulence models used had u^+ velocity curves with behaviors very similar to the curves obtained by direct numerical simulation, with the exception of the k-ε model. The results found by the k-ε model diverge significantly from the results obtained by other turbulence models analyzed and by the theoretical curves of the wall law in the turbulent region. This result corroborates the fact that the turbulence model of two differences equations k-ε does not present good performance in cases with adverse pressure gradient and flow separation, especially in those regions near the wall are regions of great interest.

Fig. 4 presents the profiles of $\sqrt{u'u'}/U_b$ obtained in the simulations carried out in the present work, compared with the results found by [1].
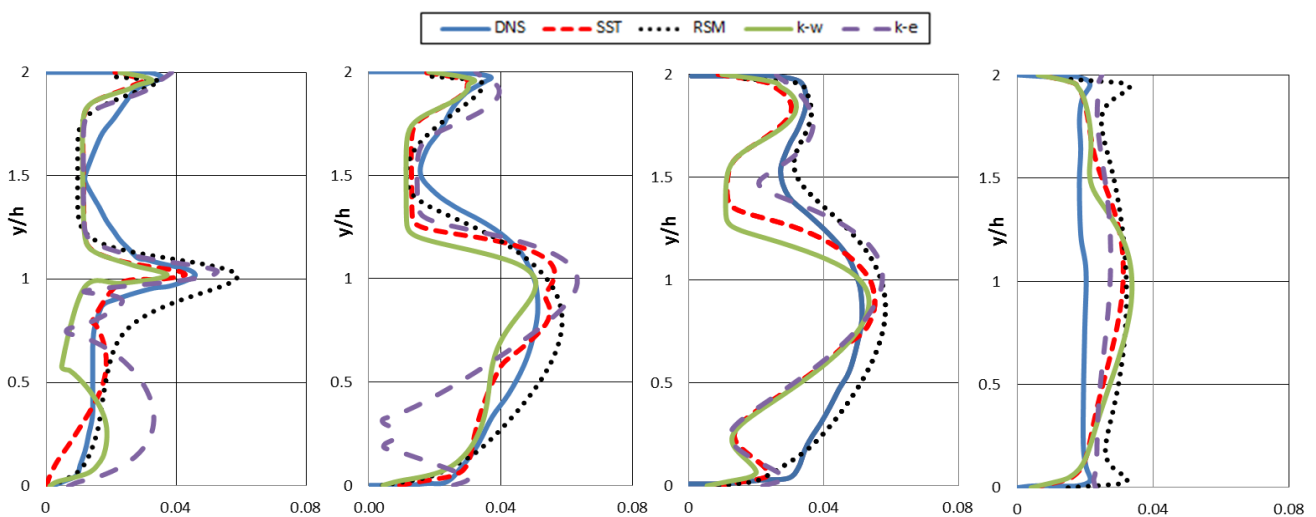

FIGURE 4. $\sqrt{u'u'}/U_b$ PROFILES AT FOUR POSITIONS.

In the turbulent intensity profile of the first position, $x/h = 0.5$, the presence of a sharp peak at the height of the step, $y/h = 1$, is observed in all models analyzed. This location refers to the region of mix layer. The $\sqrt{u'u'}/U_b$ profile obtained by means of the k-ε model presents peaks in the region below the step not predicted in the result obtained in the DNS model and not seen in the other RANS models. All models predict a peak near the top wall, according to the profile obtained by [1]. In the recirculation region, at $x / h = 4$, the k-ω, k-ε and SST k-ω models still show sharp peaks in the region near the step height,

whereas the RSM and DNS models show peaks in y/h = 1.5. As in the first position, the presence of peaks located in the top wall is observed in all models. The k-ε model again presents peaks in the regions near the bottom wall that are not predicted by any of the other models discussed in the present work. This fact is justified by the deficit of performance of this model in regions near the wall. At x/h = 8, the region close to the reattachment in most of the analyzed models, the peaks located near the top wall are regenerated in all the profiles found and peaks close to the bottom wall appear in all models of turbulence analyzed, except for the model RSM. These peaks located near the bottom wall are caused by the reattachment of the flow and cannot be seen in the RSM model because the reclosing in this model already happened in x/h = 5.86. As the flow occurs, the peaks are softened, as the flow tends to equilibrate. In the last location, at x/h = 20, we note the presence of peaks close to the bottom and top wall in all models and the behavior of the second-order quantity $\sqrt{u'u'}/U_b$ occurs more uniform. In all positions analyzed, it was possible to observe that the behavior of the $\sqrt{u'u'}/U_b$ profiles obtained by the RSM model shows greater agreement with the results found by [1] through direct numerical simulation.

V. CONCLUSION

The present work carried out computational simulations of the turbulent flow over a channel with the presence of a backward-facing step with different models of turbulence that approach the methodology of Reynolds averaged equations (RANS). The model SST k-ω obtained a result for the reattachment length equal to X_R = 8.50 and it was the model RANS that found the result closest to the value obtained by [1] through the direct numerical simulation, with reattachment length of X_R = 8.62. The second-order RSM closure model presented the lowest value of reattachment length (X_R = 5.86) and results different from that found by DNS in velocity profiles, especially in the near regions to the wall at the positions closest to the region of the collection, x/h = 4 and x/h = 8. The model k-ε obtained a value of reattachment length significantly low equal to 6.34, fact already expected since this model does not perform well in cases with pressure gradient and boundary layer separation. The RSM model obtained the best results related to the second order quantity discussed in the present study, a conclusion made when observing its profiles. This result was already expected, since it is a second-order closure model that calculates this quantity directly, unlike the other RANS models used, which use the Boussinesq Hypothesis and the turbulent viscosity modeling to calculate the quantities associated with the components of the Reynolds tensor. The k-ε model presented remarkably weak results for the analyzed second order quantity.

REFERENCES

[1] Kopera, M. A. "Direct numerical simulation of turbulent flow over a backward-facing step." University of Warwick, 2011, 178p.

[2] Rezende, A. L. T. "Análise Numérica da Bolha de Separação do Escoamento Turbulento sobre Placa Plana Fina Inclinada." Tese (Doutorado em Engenharia Mecânica) - Pontifícia Universidade Católica, Rio de Janeiro, 2009.

[3] Jones, W. P., Launder, B. E. "Prediction of laminarization with a two-equation model of turbulence." International Journal of Heat and Mass Transfer, v. 5, n.2, p. 31-34, 1972.

[4] Launder, B. E.; Sharma, B. I. "Application of the energy-dissipation model of turbulence to the calculation of flow near a spinning disk." Letters in Heat and Mass Transfer, v. 1, n. 2, p. 131-138, 1974.

[5] Wilcox, D. C. "Reassessment of the Scale-Determining Equation for Advanced Scale Models." AIAA Journal. v. 26, n. 11, p. 1299-1310, 1988.

[6] Miranda, W. R. "Simulação Numérica de uma Bolha de Separação em Bordo Arredondado Utilizando Equações Médias de Reynolds." Dissertação (Mestrado em Engenharia Mecânica) - Instituto Militar de Engenharia, Rio de Janeiro, 2014.

[7] Wilcox, D. C. "A half-century historical review of the k-w model." AIAA paper 91-0615, 1991.

[8] Menter, F. R. "Influence of free stream values on k-ω turbulence model predictions." AIAA Journal, v. 30, n. 6, p. 1657-1659, 1992.

[9] Menter, F. R. "Two-Equation Eddy-Viscosity Turbulence Models for Engineering Applications." AIAA Jounal, v. 32, n. 8, p. 1598-1605, 1994.

[10] McDonald, P. W. "The computation of transonic flow through two-dimensional gas turbine cascades." ASME, p. 71-89, 1971.

[11] Leonard, B. P."A Stable and Accurate Convective Modelling Procedure Based on Quadratic Upstream Interpolation." Computer Methods in Applied Mechanics and Engineering, p. 59-98, 1979.

[12] Patankar, S. "Numerical Heat Transfer and Fluid Flow." John Benjamins Publishing, 197p, 1980.

[13] Hutchinson B. R., Raithby G. D., 1986. "A Multigrid Method Based on the Additive Correction Strategy." Numerical Heat Transfer, p. 511-537, 1986.